UNIVERSITÀ DEGLI STUDI DI PADOVA

DIPARTIMENTO DI SCIENZE CHIMICHE
CORSO DI LAUREA MAGISTRALE IN CHIMICA INDUSTRIALE

TESI DI LAUREA MAGISTRALE

METHANATION OF CARBON DIOXIDE: OPTIMIZATION OF CATALYSTS BY MODULATING VARIOUS PARAMETERS AND POSSIBLE APPLICATION OF ZEOLITES

Relatore: Prof. Calvillo Lamana Laura

Correlatore: Dott. Gavrilovic Ljubisa

Controrelatore: Prof. Abdirisak Ahmed Isse

Laureando: Paron Enrico

ANNO ACCADEMICO 2022/2023

INDEX

ABSTRACT

Numerous efforts have recently been made to find a solution to the massive emission of carbon dioxide into the atmosphere, which is the main responsible for the climate change. This thesis work aims at improving the carbon dioxide methanation process, one of the possible strategies that could limit or stop the net emission of this powerful greenhouse gas in the near future. In particular, the use of zeolites in the catalytic bed as water sorbent has been investigated. The addition of zeolites can allow the in-situ removal of water from the reaction equilibrium, shifting it towards the products formation, in accordance with the Le Châtelier's principle. This strategy, called sorption-enhanced methanation, allows an improvement in the conversion, beyond the conventional thermodynamic limits. With this aim, two different approaches have been explored: i) dispersing the metal catalyst on two zeolites, 13X and 4A, that also act as a support; or ii) using a physical mixture of the zeolite and the catalyst in the catalytic bed.

Series of nickel or cobalt catalysts supported on different supports, such as γ-alumina, titania, or zirconia, have been prepared by using the incipient wetness impregnation or wet impregnation synthesis methods. The effect of the metal loading and the addition of ceria as promoter have also been studied. A wide arsenal of characterization techniques has been used to investigate the materials: nitrogen adsorption and desorption isotherm, X-ray fluorescence, ICP-OES, X-ray diffractometry, temperature-programmed reduction, static chemisorption of hydrogen, thermogravimetric analysis, and scanning electron microscopy. The characterization evidences that the use of nickel rather than cobalt, the choice of low calcination temperatures and the deposition on a highly porous support allow to obtain a greater dispersion, exposing a larger metallic area. The dispersion can further increase if the catalyst is promoted with cerium. Another important result is the increase of the interaction force of the metal with the support for the 10 wt.% metal loading catalysts on Alumina, causing a greater aluminate formation and decreasing the reducibility. Finally, the coating of metal particles with few atomic layers of reduced titania is observed after the reduction of the calcined catalyst, segregating the active phase.

To conclude, these catalysts have been tested in the methanation of carbon dioxide reaction by using the approaches described above. From these results, the main factors responsible for the achievement of good conversion and selectivity have been identify. These factors are a high surface area, a good reducibility and the occurrence of redox properties, introduced by the support or promoter. In addition, the catalytic tests have pointed out the superiority of the physical mixture, increasing the conversion of about 20% for an appropriate combination of reaction parameters.

The thesis has been structured in the following way. First, the crucial points of the reaction are defined in the introduction (Chapter 1), placing particular emphasis on the recycling of dioxide for the sustainable production of methane, a widely consumed commodity. The thermodynamics and kinetics of the reaction are shown, exposing the best working conditions to carry out the process and pointing out the need to use a stable and efficient catalyst. Then, the reaction mechanics are reported, to understand the intermediates involved in the production of methane (Chapter 2). The synthesis methods and characterization techniques are described in the experimental part (Chapter 3). Subsequently, the characterization of the catalysts is reported, exploring their properties (Chapter 3), and the results of the catalytic tests are described (Chapter 4).

1. INTRODUCTION

Nowadays, climate change is one of the most pressing and urgent issues, witnessing the continuous increase in average temperatures across the globe. This phenomenon is caused by multiple factors, however the main and predominant one is the emission of carbon dioxide into the atmosphere.[1–15] Due to its molecular structure, it is able to effectively absorb infrared radiation coming from the sun, releasing it later through a non-radiative relaxation process, increasing the kinetic energy of the molecules in the air, so the temperature.

Other substances are capable of carrying out the same phenomenon, even more effectively than carbon dioxide, such as methane and nitrous oxide, however only this gas is released in such an exorbitant amount, making it the main cause.

In order to avoid the aggravation of the climate warming, in recent years there has been continuous research for new and innovative technologies to prevent the release of the greenhouse gas, or at least reach a zero net emission. Various strategies have been designed over the decades, such as the in-situ capture of carbon dioxide from power plants and other industries, called Carbon Capture and Utilization, CCU. Several technologies allow the sequestration of the dioxide, such as the amine-based absorption, the membrane-based separation, the cryogenic capture, and recently also the adsorption, limiting the energy consumption of the process. Regarding this last method, a lot of research is being developed, in particular in the application of porous solids, such as zeolites and activated carbon, capable of chemically capturing the dioxide, for example lime, or combining both features, impregnating zeolites with amines.[1,2,7,11,15–25] Another possibility is the transition to renewable and sustainable fuels, such as hydrogen, converted to water, avoiding the formation of greenhouse gases.[4–6,26–28]

In this regard, an entire production chain is being developed, commonly called the hydrogen economy. However, nowadays hydrogen is mostly produced from fossil fuels, called it grey, making it a cause in the dioxide emission. To avoid it, it is necessary to produce it from electrochemical splitting of water, gaining green hydrogen. The big problems with this fuel are the high production cost, far above the conventional grey, and the difficulty of transportation, storing a potentially explosive and very light gas, quite difficult to liquefy.[29]

An innovative solution is offered by the methanation of carbon dioxide, which involves its hydrogenation to create sustainable methane, as shown in Equation 1.1, closing the emission cycle since the same quantity of greenhouse gas released by combustion would be captured to carry out the reaction.[1–3,7–16,22,24,29–51] The substitution with such manageable energy vector can solve one of the major problems of hydrogen, that is transportation, since the world economies have used natural gas for decades, finalizing and improving its distribution through pipelines and tankers.[2,13,16,29,31,43–46,52] Besides, the thermodynamics of methane formation is the most advantageous among the various hydrocarbons and alcohols, allowing the operation to be carried out easily.[8,12,31,52]

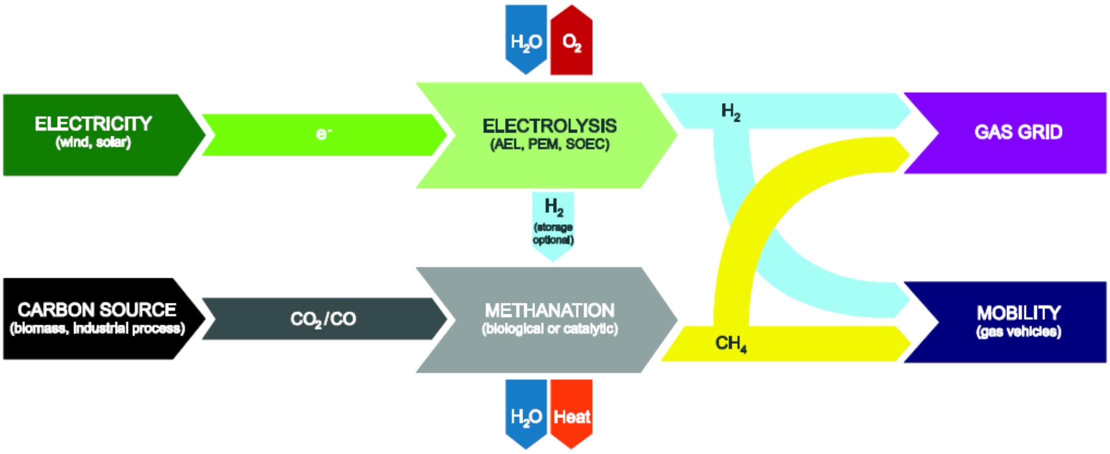

Fig. 1.1 Representation of a general methanation process.[44]

At the moment, the catalytic methanation would be performed in three different ways, depending on the reagent source. One of the most important approaches is the conversion of pure carbon dioxide streams, which would be captured from power plant flue gas or other industrial process. Another possibility is the transformation of raw and conditioned syngas, obtained by the gasification of biomass or coal, to methane, hydrogenating the carbon oxides with the hydrogen fraction in the synthetic gas. Furthermore, the methanation of carbon dioxide can be used for the improvement of the quality of biogas, enriching it with methane by conversion of the carbon dioxide fraction, in a process called biomass upgrading. The first and third method are often referred as Power-to-Gas technologies, since they allow the storage of a surplus of renewable energy, in the form of a widely used fuel.[3,11–13,16,29,39,42,44,45,50] A schematic representation of the process is shown in Figure 1.1.

$$CO_2 + 4H_2 \rightleftharpoons CH_4 + 2H_2O \qquad \Delta H_{298K} = -165.0\ kJ/mol \quad \text{(Eq. 1.1)}$$

The methanation of carbon dioxide can be seen as an evolution of the homonymous carbon monoxide reaction, shown in Equation 1.2, industrially used to minimize the presence of oxygenated carbon compounds in the reagent stream for the production of ammonia. These oxides are poisons for the iron catalyst, leading to its oxidation and decrease in activity, up to total deactivation.[13,30,37,42,45,51,53]

Lately, it has also been used to reduce the carbon monoxide content below 20 ppm in hydrogen-containing streams, used for the production of electricity with fuel cells. Indeed, the monoxide is a powerful poison towards the metal of the anode, blocking the development of the electrochemical reaction. Such approach is very cheap, not requiring high temperatures and not introducing any reagent to the mixture, which could be a source of impurities.[54–57]

$$CO + 3H_2 \rightleftharpoons CH_4 + H_2O \qquad \Delta H_{298K} = -206.2\ kJ/mol \qquad \text{(Eq. 1.2)}$$

Due to the complexity of the system, other reactions can occur, leading to the formation of a multitude of by-products, decreasing the selectivity and the methane yield. The most important parasitic reactions are: the reverse water-gas shift reaction (RWGS), shown in Equation 1.3, transforming dioxide into monoxide; the reverse dry reforming of methane, shown in Equation 1.4, converting carbon monoxide into methane and carbon dioxide through disproportionation; the Boudouard reaction, the cracking of methane, the reduction of carbon dioxide and monoxide, shown in Equations 1.5 1.6, 1.7 and 1.8, producing carbon coke; and finally, the Fischer-Tropsch synthesis, shown in Equation 1.9, generating a multitude of long and medium chain, saturated and unsaturated hydrocarbons.[13,16,58]

$$CO_2 + H_2 \rightleftharpoons CO + H_2O \qquad \Delta H_{298K} = +41.2\ kJ/mol \qquad \text{(Eq. 1.3)}$$

$$2CO + 2H_2 \rightleftharpoons CH_4 + CO_2 \qquad \Delta H_{298K} = -247.3\ kJ/mol \qquad \text{(Eq. 1.4)}$$

$$2CO \rightleftharpoons C + CO_2 \qquad \Delta H_{298K} = -172.4\ kJ/mol \qquad \text{(Eq. 1.5)}$$

$$CH_4 \rightleftharpoons C + 2H_2 \qquad \Delta H_{298K} = +74.8\ kJ/mol \qquad \text{(Eq. 1.6)}$$

$$CO_2 + 2H_2 \rightleftharpoons C + 2H_2O \qquad \Delta H_{298K} = -90.1\ kJ/mol \qquad \text{(Eq. 1.7)}$$

$$CO + H_2 \rightleftharpoons C + H_2O \qquad \Delta H_{298K} = -131.3\ kJ/mol \qquad \text{(Eq. 1.8)}$$

$$nCO + (2n+1)H_2 \rightleftharpoons C_nH_{2n+2} + nH_2O \qquad \text{(Eq. 1.9)}$$

In order to determine the best working conditions, it is necessary to study the thermodynamics of all the involved reactions. The most used approach is the Gibbs free energy minimization method, which allows to determine the amount of species at the equilibrium for a settled operating condition.[16,58]

An increase in temperature leads to a decrease in the conversion of carbon dioxide, since its methanation is exothermic, being favored at low temperatures. At the same time, a decrease in selectivity occurs, caused by the greater role of the endothermic parasitic reactions. Above approximately 600°C, for 1 atm, there is a recovery of the conversion, due to the transformation into carbon monoxide carried out by the reverse water-gas shift reaction. A large presence of methane and water is found at low temperatures, while at higher ones the gas is mainly made up of hydrogen, carbon dioxide and carbon monoxide.[1,10,11,16,29,32,42,43,43,44,46,54,58]

Increasing the pressure beyond 1 atm, there is an increment of both the conversion of dioxide and the selectivity, since the reaction occurs by reducing the number of total gaseous moles. That allows a dominant presence of methane and water even at higher temperatures, being able to carry out methanation in a bigger temperatures range.[10,11,16,42,43,58] Although this strategy may be advantageous from a thermodynamic point of view, it is not economically, since it is necessary to use expensive pressurization systems and compressors.[1,42,44] Figure 1.2 shows the calculated conversion, selectivity and yield of the carbon dioxide methanation, changing the temperature and pressure, taking into account only the thermodynamics.

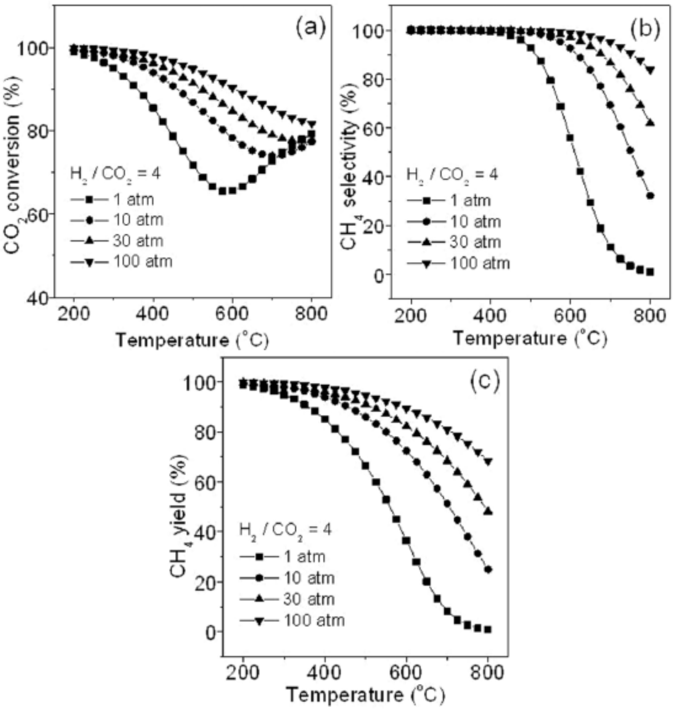

Fig. 1.2 Effect of temperature and pressure on a) conversion, b) selectivity and c) yield of carbon dioxide methanation.[58]

Changing pressure or temperature for a stoichiometric feed, composed of a 4:1 volumetric ratio of hydrogen and carbon dioxide, no carbon coke is formed. That is caused by the water produced by methanation, removing the residues through the oxidation to dioxide or monoxide. It also means that a voluntary introduction of water into the reactor would not bring any benefit, rather it would reduce the conversion by shifting the methanation equilibrium towards the reactants.[16,42,58]

A decrease of the content of hydrogen would lead to a drastic decline in conversion and selectivity, as well as a strong deposition of carbon, especially at low temperatures. Contrary, for an excess of hydrogen, there would be a slight increase in conversion and selectivity, not producing any carbon residues.[11,16,29,32,42,58]

From the considerations made so far, it is concluded that, for the optimal methanation performance, the temperatures must be between 300°C and 350°C, working at 1atm, with a stoichiometric supply of hydrogen and carbon dioxide. This conditions take in account the need to provide sufficient thermal energy to overcome the activation barrier of the reagents, by using a catalyst in a realistic situation, obtaining a conversion of around 80% and a complete selectivity towards methane.[1,29,43,44,46]

It is very important to point out that, even if the thermodynamic confirms that a reaction can take place, it does not mean that it will actually occur, since it must also be possible from a kinetic point of view.[16,45]

Contrary to the reduction of carbon monoxide, which involves a six electrons transfer, the hydrogenation of dioxide involves an eight electrons transfer, resulting in a much trickier and slower reaction to carry out. The solution is the application of an efficient catalyst, sufficiently active to allow the reaction to proceed at acceptable temperatures.[10,11,30,36,42,45,54,56,58,59]

Among the various metals, the most active and selective are the noble metals, including platinum, palladium and ruthenium. However, their use in the industrial sector is strongly limited by their high cost and low availability. For this purpose, it is preferred to use first period transition metals, among which nickel stands out, due to its good activity and selectivity, while keeping a low cost and great abundance.[1,3–6,10,11,13–15,22,24,26,28,30,32,33,35,37–39,44,45,47–50,54,56,60–69] Other metals can be taken in account, such as iron and cobalt, but these show a lower selectivity, leading to a greater formation of long-chain hydrocarbons. Indeed, these two metals are commonly used in the Fischer-Tropsch synthesis, for the transformation of syngas into long and medium chain hydrocarbons.[70–82]

The main issue related to the use of nickel is its rapid deactivation, caused by two factors, which are the deposition of carbon coke, leading to clogging of the catalyst pores, and the sintering of the metal, decreasing the active metal area. The deposition of carbon can produce different morphologies, for example hollow nanotubes or nanofibers, as shown in Figure 1.3, which are chemically stable and difficult to remove. The sintering is caused not only by the greater mobility of the metal at high temperatures, but also by the formation of volatile carbonyls, which allow the vaporization and deposition of the metal, in a mechanism similar to the Ostwald ripening. That allows the growth of larger crystallites, consuming the smaller ones and smoothing the nanoparticles. The formation of the volatile carbonyls is preferential at low temperature, since the catalyst is not activated enough to hydrogenate carbon monoxide to methane, leading to its greater presence.[3,4,6,10,11,24,26–28,31,35,37,43,45,48,50,52,55,62,63,65–69,83,84]

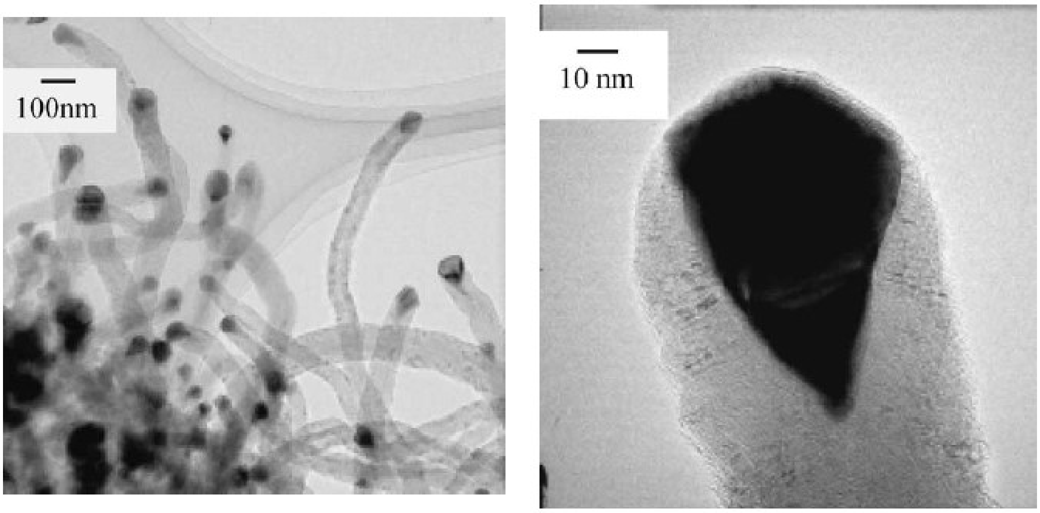

Fig. 1.3 TEM images of carbon nanofibers form by methane decomposition over a nickel catalyst.[55]

The substitution with cobalt does not lead to greater stability, since this metal suffers from surface oxidation, due to the greater energy of interaction with oxygen. The formation of the oxide layer decreases the active sites for carrying out the reaction, up to complete deactivation. In addition to this phenomenon, the sintering of the metal is also observed, accelerated by high temperatures.[63,65,72,79]

For this purpose, numerous variants of nickel catalysts are being developed and designed, capable of resisting these two phenomena through the application of different strategies. Some examples are provided by the introduction of promoters with oxidoreductive characteristics, such as cerium, the application of reducible supports to improve the oxidation of the carbon deposits, or the formation of bimetallic catalysts, which the more promising seems to be a blend of nickel and cobalt, by removing the carbon accumulation by oxidation with the oxygen adsorbed on cobalt.[4,10,28,31,40,48,51,53,60–63,65,66]

Recently, the possibility of modifying the thermodynamic of the reaction has been proposed and investigated, exceeding the conventional limits and increasing the carbon dioxide conversion, in accordance to the Le Châtelier principle. The concept is called sorption-enhancement and is based on the in-situ removal of water, moving it away from the metal surface and freeing the active sites for the transformation of further reagent. Another positive effect is the slowing down of the deactivation of the catalyst, since water is able to promote oxidation and sintering of the metal.[1,9–14,16,38,39,42,45,46,85–89]

Such concept is not applied only to the methanation, but also to improve other crucial reactions for the production of fuels, for example gasification, reforming and water-gas shift reaction, adsorbing carbon dioxide instead of water.[88]

The reaction is commonly called sorption-enhanced methanation (SEM) and allows to obtain a gas with an extremely low content of hydrogen. It has been calculated that, for appropriate operating conditions, the reactor product can be injected directly into the distribution system, without any refinement to lower the concentration of species other than methane, in order to fall within the legal limitations. That would significantly decrease the costs, avoiding a purification step that would otherwise be necessary for traditional methanation.[13,16,42,45] If the hydrogen legal limit cannot be respected, it is always possible to market the mixture as hydro-methane, a blend consisting of 5% to 30% by volume of hydrogen, increasing the combustion efficiency and reducing the emission of unburned hydrocarbons and carbon dioxide.[30,42]

Water adsorption can be carried out with different types of materials, but it must be reversible, allowing the reuse of the sorbent. The most interesting class of sorbents are zeolites, since they have a great water adsorption capacity and excellent stability, keeping high performance even after a long series of adsorption and desorption cycles.[1,9,11–14,38,39,45,85,86,88,90–92]

There are two strategies to implement zeolite in the catalytic system. The first approach is called one-particle system and is based on the use of zeolite as a support for the active phase, achieving an intimate contact with the metal, therefore better water removal. Figure 1.4 shows a schematic representation of the sorption-enhanced methanation for the one-particle system. However, this method lacks flexibility, since the amount of zeolite is related to the loading of metal into the catalyst, so it is impossible to regulate independently its quantity into the reactor. The other strategy is the introduction of the zeolite as an additive to the catalytic bed, called two-particle system, limiting the contact and exchange of matter between catalyst and sorbent, but increasing the flexibility of the operation, since it is possible to freely vary the quantity in the reactor, based on the needs and operating objectives set.[1,9,11–14,38,39,85,86,88,93]

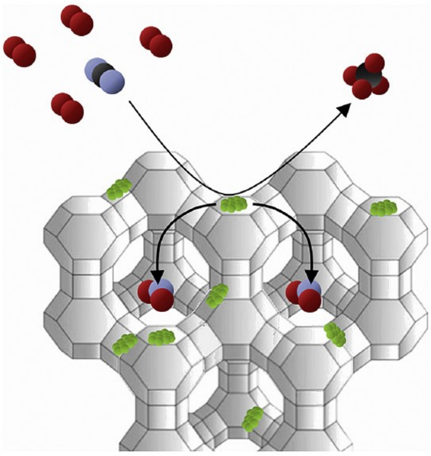

Fig. 1.4 Representation of a sorption-enhanced methanation over a zeolite-based nickel catalyst, according to the one-particle system.[85]

The capture of water causes a variation in the composition of the gas leaving the reactor, in particular at low temperatures a greater presence of methane and lower water content is observed, while the formation of carbon coke occurs by pushing at higher temperatures, due to the increase in selectivity towards the deposition of this by-product.[16,39,45]

For higher pressures, up to 10 atm, there is a lower effect due to the removal of the product, however there is clearly a reduced generation of carbon residues. Other useful strategies involve the use of an excess of hydrogen, hydrogenating the deposited carbon to methane.[16]

It is even possible to engineer the reactor, adopting the type of catalytic bed that is most suitable to carry out the reaction. A fixed bed would make the regulation of sorbent rather difficult, performing the desorption phase only when the zeolite is completely saturated, making the use of an excess of hydrogen the only applicable strategy to limit the deposition of carbon coke. On the contrary, the use of a fluidized bed would enable to regulate the circulation of the sorbent, allowing an accurate control of its quantity in the reactor, limiting the removal of water to hinder the formation of carbon deposits.[16,38,46] Figure 1.5 shows the project of a pilot reactor with multiple fixed beds used for sorption-enhanced methanation.

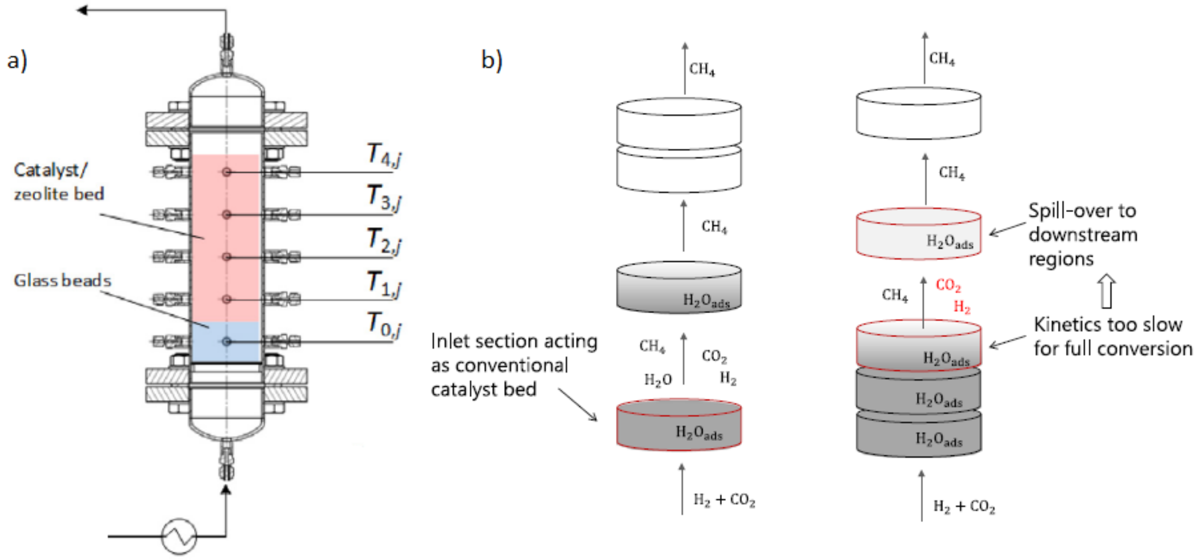

Fig. 1.5 Representation of a) a pilot reactor with several fixed beds and of b) the evolution of the sorption-enhanced methanation in it over the time.[46]

2. REACTION MECHANISM

To fully comprehend the progression of carbon dioxide methanation, it is necessary to understand the reaction mechanism and the involved intermediates. Unfortunately, the exact reaction path that allows the formation of methane is not fully known, having developed over the years two possible hypotheses of reaction mechanism:[8,10,11,14,22,30,41]

- with formation of carbon monoxide;
- without formation of carbon monoxide.

It is universally accepted that the hydrogen used in the various steps is provided by the surface of the metal, through dissociative chemisorption of the molecule.[15,22,30,36,41,48,83] The hydrogen atoms react on the metal surface, but can be even transferred to the surface of the support, through a process called spill-over.[8,11,24,36,37,41,48,52,56,57,85,87,89]

The first reaction mechanism is the most widely accepted and considers the methanation of carbon dioxide as the overall result of two other reactions, which are the reverse water-shift reaction (RWGS), involving the transformation of dioxide into monoxide, and the methanation of the latter, completing the reduction to methane.[1,22,29,37,41,50,51,57,58,83]

To study the reaction path, numerous studies have been carried out using infrared spectroscopy in operando conditions, raising the temperature and recognizing the different intermediates that are formed on the catalyst surface. Carbonate and bicarbonate are the first intermediates that are formed. They obtained by adsorption of the dioxide on a basic site of the support, for example hydroxyl groups. Both species can exist in monodentate and bidentate forms, resulting in a different reactivity, caused by the stabilization offered by the support.[8,22,37,39–41,48,52,53,56,62,66,68]

Raising the temperature, the desorption of bidentate carbonate takes place, leaving only the monodentate. Afterwards, the reduction of the bicarbonates and the remaining carbonates occurs to form the formates, respectively bidentate and monodentate, the latter more reactive. According to the first reaction path, the formate is converted by reduction to carbon monoxide, which subsequently transfers to the metal surface, positioning itself on hollow, bridged and linear sites.[8,22,24,30,33,36,37,39–41,47,48,52,53,56,83] The different sites lead to a change in the interaction energy between the carbonyl and the metal surface, being greater for hollow sites, while gradually decreasing for bridged and linear carbonyls. Less bonded carbonyls are the last to form on the metal and they can desorb quite easily, generating carbon monoxide as by-product,.[12,29,36,41,81,83,94]

Some studies show that carbon monoxide can even behave like a poison, being adsorbed on the metal surface, decreasing the area available for dissociative chemisorption of hydrogen, leading to a decrease in reactivity.[5,41,52,57,95]

On the surface of the metal, especially the (111) planes, the carbonyls undergo a further split, releasing the oxygen atom and converting it to water, while the carbon remains on the surface to form metal carbide, a reactive intermediate. Such carbide layer decreases the adsorption of carbon monoxide on the planar surface of the metal, leaving available mainly low coordinated sites, for example edges and vertexes of the particle, from which carbon monoxide is preferentially desorbed. The carbide is repeatedly attacked by atomic hydrogens, until it is completely hydrogenated to methane, free to desorb and exit the reactor.[22,30,37,41,48,52,53,62,83] Figure 2.1 shows a schematic representation of the reaction path by the formation and hydrogenation of carbon monoxide.

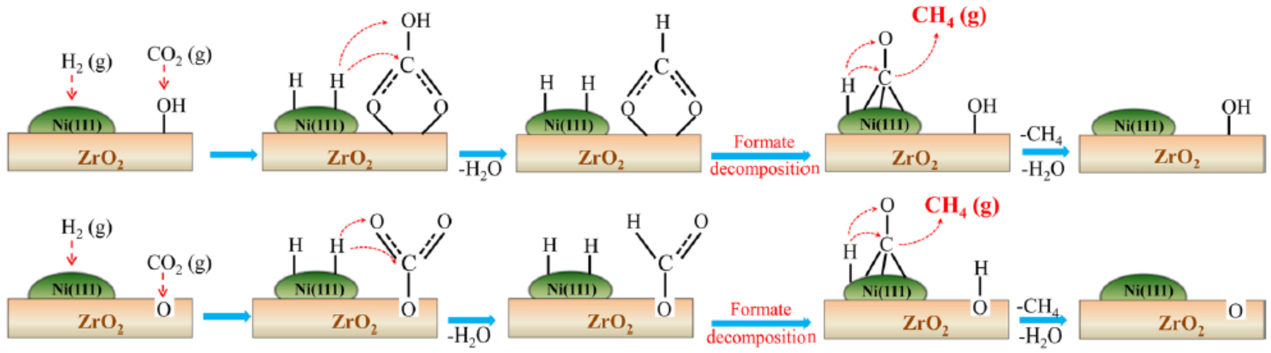

Fig. 2.1 Representation of the carbon monoxide route for methanation over a zirconia-based nickel catalyst.[48]

Differently, the second reaction mechanism assumes the conversion of the formate to methoxide on the surface of the support, which can undergo a further reduction in order to remove the oxygen as water, leaving a methyl group. Both methoxide and methyl groups are hydrogenated to allow the generation of methane and its desorption. It should be noted that this different reaction path considers the metal surface only as a hydrogen source, while the entire dioxide conversion takes place on the surface of the support, at the interface between the two phases.[8,22,30,36,48] Figure 2.2 shows a schematic representation of the reaction mechanism by the decomposition of formate to methoxide and its subsequent reduction to methane.

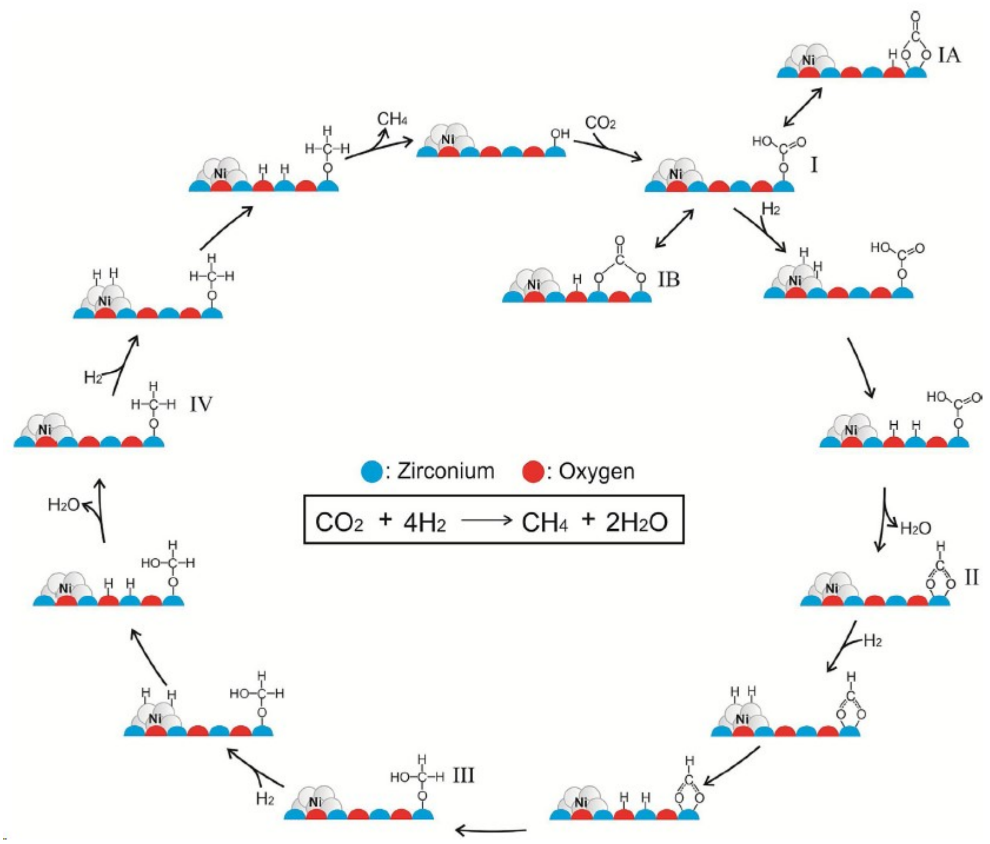

Fig. 2.2 Representation of the methanation mechanism without formation of carbon monoxide over a zirconia-based nickel catalyst.[8]

The prevalence of one reaction path rather than the other depends on a multitude of factors, primarily the characteristics of the support, resulting in different adsorptions and activations of the carbon dioxide molecules. For example, a distinctive effect is the enrichment of electron density of the metal from the support, allowing a greater retrodonation for the breaking of the carbon-oxygen bonds.[2,4,8–11,15,32,33,36,37,40,62,68,71,75,78,94,96] Another case are the reducible supports, which adsorb the dioxide on mild basic sites and proceed to the gradual conversion to methane only on the support surface, accepting hydrogen atoms from the metal by spill-over. While, the formation of monoxide is attributed to the reaction of the dioxide with a reduced metal center, resulting in the filling of the oxygen vacancy. Such intermediate can be desorbed as a by-product or hydrogenated on the metal surface.[8–10,24,36,37,40,48,52,57,66,85]

Other parameters to take in particular consideration are temperature and pressure, guiding the conversion one mechanism or the other for different operating conditions. Besides, it is important to remember that the presence of one mechanism does not necessarily exclude the other, as both can occur at the same time, as parallel processes.[8]

3. EXPERIMENTAL

3.1 *Materials*

The materials employed as catalyst support are: alumina powder (Puralox SCca 150/200 by Sasol), titania powder composed of a mixture of anatase and rutile, in an approximately 3:1 molar ratio (Titanium(IV) oxide, Aeroxide P25 by Thermo Fisher Scientific)[24], 1/8" pellets of titania in anatase phase (Titanium(IV) oxide, catalyst support by Thermo Fisher Scientific) and 1/8" pellets of zirconia in monoclinic phase (Zirconium oxide, catalyst support by Thermo Fisher Scientific). The used zeolites are 13X (Z10 by Zeochem) and 4A (Z4 by Zeochem), both in the shape of beads with a diameter between 1.6 mm and 2.6 mm. The full summary is reported in Table 3.1.

Table 3.1 Main features of the material used as support for the synthesis.

Denomination	Composition	Company
Alumina	γ-alumina	Sasol
Titania P25	mixture of anatase and rutile	Thermo Fisher Scientific
Anatase	anatase	Thermo Fisher Scientific
Zirconia	monoclinic zirconia	Thermo Fisher Scientific
13X	13X	Zeochem
44	4A	Zeochem

The metal precursors for the syntheses are: 99% pure nickel nitrate hexahydrate (Nickel(II) nitrate hexahydrate by Acros Organics), 99% pure cobalt nitrate hexahydrate (Cobalt(II) nitrate hexahydrate by Acros Organics) and 99.9% pure cerium nitrate hexahydrate (Cerium(III)-nitrate from Fluka AG. Buchs SG). The ceria sample, used as a reference in some characterizations, is obtained from cerium nitrate hexahydrate, by calcination in a muffle at 500°C for 3h in static air with a thermal ramp of 5°C/min. All the gaseous effluents are provided by Nippon Gases company.

3.2 *Catalyst synthesis*

In order to have a homogeneous powder to be used as support, we proceed with grinding both the titania and zirconia pellets and the 13X and 4A beads, using a mortar and a pestle, taking care to clean the equipment with abrasive sand and milli-Q water whenever it is decided to crush a different material.

For the synthesis of the various catalysts, the wet impregnation (WI) method was adopted. However, in the case of alumina as support, the incipient wetness impregnation (IWI) method was also used. The difference between these two synthesis techniques lies in the fact that the former allows the deposition of the precursor both on the external surface and inside the pores of the support. On the other hand, for the IWI method, the metal precursor is deposited only inside the pores. Therefore, in the latter case, the metal loading of the catalyst is limited by the solubility of the precursor in the small amount of solvent that we can use, which should be equal to the pore volume of the support material. For this reason, the IWI technique is only used for highly porous materials, such as alumina.[77]

For the wet impregnation synthesis, the appropriate amount of precursor needed to obtain a metal loading of 15% or 10% was weighted. Subsequently, the metal nitrate was poured into a beaker together with an arbitrary amount of milli-Q water, typically between 20 g and 50 g. The solution was kept under stirring for about 10 minutes at room temperature. In the meantime, the appropriate quantity of support was slowly added to the metal precursor solution, once the salt was completely dissolved, while the stirring was regulated in order to avoid sedimentation. Finally, the suspension was heated up to at 80°C and kept at this temperature overnight to allow the solvent to evaporate. The following morning the beaker was placed in an oven at 110°C for 24h, in order to completely eliminate any trace of humidity.

For the incipient wetness impregnation, the appropriate amount of precursor needed to obtain a metal loading of 15% or 10% was weighted. Subsequently, the metal nitrate was poured into a beaker, but this time the amount of milli-Q water used to dissolve it was equal to the support pore volume, for example 5.0 g of water for 10.0 g of alumina. The solution was kept under stirring for about 10 minutes at room temperature. The correct amount of alumina powder was weighted and placed on a Petri dish, arranging it as evenly as possible. Using a pipette, the solution was taken and added to the support, drop by drop, while mixing with the tip of a spatula to homogenize the dispersion of the solution. Unlike the previous synthesis technique, in this case we had a powder with a dry appearance, indicating that the precursor solution is not present in the spaces among the particles, but only inside the pores of these ones. After covering the dish with drilled aluminum foil, it was placed in the oven for 24h at 110°C to eliminate all the water.

The synthesis of cerium-promoted catalysts was carried out by co-impregnation, according to the methods previously explained. Particular attention must be paid to weigh the correct amount of the two precursors, as it is not possible to use the same quantities used for the synthesis of unpromoted catalysts. The desired cerium loadings were 2, 3, 4 and 5%.

The different samples from the various synthesis were placed into appropriate ceramic crucibles and introduced into a muffle where they were calcinated at 550°C, and also 850°C in the case of nickel, for 1h in static air with a thermal ramp of 5°C/min. In the case of impregnation on zeolite, the calcination was performed at 450°C for 3 hours, to limit the degradation of the crystalline structure of the zeolite as much as possible.

The various catalysts were labelled in order to indicate: the percentual metal loading, the metal used in the synthesis, the support, and the calcination temperature. If the support is made of alumina, it is indicated which synthesis technique was adopted. For the promoted catalysts, it is also specified the loading of cerium. The list of the catalysts is reported in Table 3.2.

Table 3.2 Nomenclature of the prepared catalysts.

• with Alumina:	15Ni/Alumina_IWI_550 15Ni/Alumina_WI_550 15Ni/Alumina_IWI_850 15Ni/Alumina_WI_850 15Co/Alumina_IWI_550 15Co/Alumina_WI_550 10Ni/Alumina_IWI_550 10Ni/Alumina_WI_550 10Ni/Alumina_IWI_850 10Ni/Alumina_WI_850 10Co/Alumina_IWI_550 10Co/Alumina_WI_550
• with TitaniaP25:	15Ni/TitaniaP25_550 15Ni/TitaniaP25_850 15Co/TitaniaP25_550
• with Anatase:	15Ni/Anatase_550 15Ni/Anatase_850 15Co/Anatase_550
• with Zirconia:	15Ni/Zirconia_550 15Ni/Zirconia_850 15Co/Zirconia_550
• with zeolites:	15Ni/13X_450 15Ni/4A_450
• promoted with cerium:	15Ni_2Ce/Alumina_IWI_550 15Ni_2Ce/Alumina_WI_550 15Ni_3Ce/Alumina_IWI_550 15Ni_3Ce/Alumina_WI_550 15Ni_4Ce/Alumina_IWI_550 15Ni_4Ce/Alumina_WI_550 15Ni_5Ce/Alumina_IWI_550 15Ni_5Ce/Alumina_WI_550 15Ni_2Ce/Alumina_IWI_850 15Ni_2Ce/Alumina_WI_850 15Ni_3Ce/Alumina_IWI_850 15Ni_3Ce/Alumina_WI_850 15Ni_4Ce/Alumina_IWI_850 15Ni_4Ce/Alumina_WI_850 15Ni_5Ce/Alumina_IWI_850 15Ni_5Ce/Alumina_WI_850

3.3 *Characterization techniques*

3.3.1 *Nitrogen adsorption and desorption isotherm*

In order to analyze the textural properties of the various catalysts, such as surface area, pore volume and average pore diameter, the isothermal adsorption and desorption of nitrogen was performed, recording the quantity of adsorbate in relation to the relative pressure. Nitrogen was used, due to its inert nature, ensuring reversible physisorption with the surface of the solid, however it is also possible to use other gases, such as argon or krypton.

The most used model for understanding physical adsorption is the BET isotherm, from the initials of those who developed it, Brunauer, Emmett and Teller. The main idea is that the forces at play during the condensation of the gas on the solid are the same ones responsible for the formation of multiple layers of adsorbate on its surface. The assumptions of the model are the following:

- the first layer of adsorbate interacts with the surface of the solid with uniform energy interactions, so the surface is considered homogeneous and identical at every point;
- the formation of a layer occurs only upon completion of the previous one;
- at saturated vapor pressure, the number of adsorbate layers is infinite, so resulting in the condensation of the gas on the surface of the solid;
- the adsorbate molecules do not present any lateral interaction with others in the same layer, instead they interact only with those of the upper or lower layer;
- the enthalpy of interaction between the first layer and the surface of the solid is equal to the enthalpy of adsorption, while it is equal to the enthalpy of vaporization for all other interactions among the upper layers.

Based on these axioms, it is possible to define the equation that links the volume of adsorbate, V_a, to the applied pressure, P, shown in Equation 2.1, knowing the saturated vapor pressure, P_0.

$$\frac{P}{V_a(P_0-P)} = \frac{1}{V_{ML}C} + \frac{C-1}{V_{ML}C} \cdot \frac{P}{P_0} \qquad \text{(Eq. 2.1)}$$

$$C \propto e^{\left(\Delta H_{ads}-\Delta H_{vap}\right)/RT} \qquad \text{(Eq. 2.2)}$$

The constant C is related to the enthalpy of adsorption and vaporization, the latter one is typically well cataloged in manuals. Equation 2.2 shows this relation.

Through a linearization process of the expression, it is possible to obtain the value of the volume of adsorbate that constitutes the monolayer in contact with the surface of the solid, V_{ML}, being able to obtain the surface area of the porous solid, A_s, as shown in Equation 2.3, knowing how much area is occupied by the single adsorbate, A_m, equal to 16.2 Å^2 for the nitrogen molecule.

$$A_s = \frac{V_{ML}}{0.0224} N_A A_m \qquad \text{(Eq. 2.3)}$$

To get the distribution of the pores and to calculate their volume and average diameter, the BJH method is applied, by the creators Barrett, Joyner and Halenda, which is an iterative method that considers the emptying of the pores from the liquid, that has been condensed into them by reaching the saturated vapor pressure, by lowering the pressure through sequential small steps. Applying the Kelvin equation, shown in Equation 2.4, it is possible to understand in which pores there may be condensation or not during the adsorption phase, and vaporization or not during the desorption phase, being able to link the quantity of adsorbate released during the desorption step with the pore size.

$$ln\left(\frac{P^*}{P_0}\right) = -\frac{2\gamma v \ cos\theta}{RTr_m} \qquad \text{(Eq. 2.4)}$$

The factors in the expression are: the critical condensation pressure, P^*, above which condensation is observed inside the pore; the surface tension of the liquid, γ; the molar volume of the adsorbate, v; the contact angle between the surface and the liquid inside the pore, θ; and the average radius of curvature of the meniscus created by the liquid, r_m, dependent by the dimension of the pore. According to this equation, we see filling and emptying of small pores at low relative pressure, while filling and emptying of bigger ones for a higher relative pressure. In general, the pores are differentiated into micropores, with a diameter of less than 2 nm, mesopores, with a diameter between 2 nm and 50 nm, and macropores, with a dimension greater than 50 nm.

To carry out the analysis, 0.5 g of powder were weighed, poured into an appropriate quartz tube with a bulb at the end, used for this specific analysis, and subsequently degassed at 300 °C for 24 hours, in order to guarantee the complete absence of any adsorbate on the surface of the solid. This operation was conducted with a VacPrep 061 sample degassing system by Micromeritics. At the end of the degassing, we proceed with the reweighing of the sample, properly subtracting the tare, and with the isothermal adsorption and desorption carried out by the machine 3Flex by Micromeritics, calibrated using a reference material of silica-alumina, at the temperature of -195.8°C, reached by immerging the sample in a liquid nitrogen bath, confined in a container. Figure 3.1 shows VacPrep 061 sample degassing system and the tube used for the analysis, while Figure 3.5 shows 3Flex.

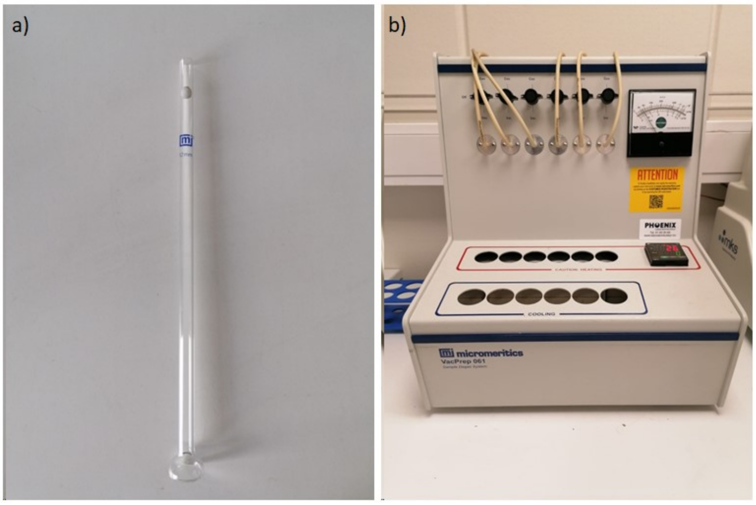

Fig. 3.1 Pictures of a) the tube used for the nitrogen adsorption and desorption and of b) VacPrep 061 sample degassing system.

3.3.2 *X-ray fluorescence*

To determine the mass percentage content of the elements in the catalysts, in particular of the introduced metal by impregnation, X-ray fluorescence spectroscopy, XRF, was used.

The analysis begins by irradiating the sample with high frequency electromagnetic radiation, so X-rays, since they are energetic enough to allow the promotion of the electrons from the core levels up to empty orbitals, by absorption of a photon. This allows the creation of an electronic hole in the atomic orbital of origin of the excited electron. Finding itself in non-equilibrium conditions, the system evolves with the transition of an electron from a core orbital, with a higher energy than the one containing the electronic hole, to this one, with consequent filling of the hole. By conservation of energy, the electronic transition is accompanied by the emission of a photon with energy equal to the energy difference between the two orbitals, according to the fluorescence phenomenon shown in Equation 2.5.

$$E_{h\nu} = E_2 - E_1 \tag{Eq. 2.5}$$

Based on the fluorescence emission spectrum, characteristic for each element, it is possible to trace back the chemical composition of the sample and quantify the content of the different atoms.

It should be noted that the electronic transition occurs between core levels, therefore atomic orbitals, since being particularly concentrated around the nucleus, are not overlapped with orbitals of other atoms, leading to the possible creation of molecular orbitals. This means that the analysis allows to identify and quantify the atoms in the sample, without caring about how they interact with each other, forming bonds.

The analysis was carried out with Niton XL5 Plus portable instrument, supplied by Thermo Fischer Scientific, generating the necessary radiation for the measurement with an X-ray tube, having a silver plate as target, hit by an electron beam accelerated by a voltage difference of 50 kV and an intensity of 500 μA. The sample was poured into a disposable container with a thin transparent plastic sheet on the bottom, subsequently placed above the irradiation spot, with a diameter of 8 mm. Figure 3.2 shows Niton XL5 Plus.

Fig. 3.2 Picture of Niton XL5 Plus portable instrument.

3.3.3 *Inductively coupled plasma–optical emission spectroscopy*

In order to determine the content of the metals in the catalysts, in particular the cerium in the promoted ones, the inductively coupled plasma–optical emission spectroscopy was performed, basically called ICP-OES.

The technique uses a plasma up to 10000 K, generated by the application of a radio frequency electric field, obtained by the passage of current through three coils. The torch is supplied with a flow of argon and ignited by a spark or an electric arc, allowing the ionization of a few atoms of the carrier gas. Subsequently, the ions are accelerated by the magnetic field generated in conjunction with the electric one, leading to energetic collisions which involve further ionization of the atoms and the consequent formation of the plasma. The shape of the plasma is a feather-like, dictated by the application of the magnetic field, with gradually lower temperatures moving closer to the tip, away from the coils.

The solution is introduced through a small tube, pushed by a peristaltic pump up to the entrance of the torch. At this point a nebulizer allows its dispersion while the argon transports it to the plasma, where atomization and ionization take place. In plasma, ions and electrons recombine and split, allowing the creation of a characteristic electromagnetic emission of the element. At this point a monochromator and a detector allow the acquisition of the emission spectrum, quantitatively determining the elements of interest and their concentration.

The preparation of the solution occurred by weighing exactly 0.2 g of powdered catalyst, introduced into an inert crucible with a sufficient aliquot of solution containing nitric acid and hydrochloric acid, in a 1:3 molar ratio, called aqua regia. The sample was solubilized by microwave digestion. Once the solid had been dissolved, dilution was carried out to 50mL, obtaining the mother solution. In order to allow the analysis, falling within the detection range of the instrumentation, serial dilutions of 1:1, 1:10 and 1:100 were performed, introducing the various solutions into the apparatus to carry out the determination of the elements.

The instrument used to carry out the analysis is 5800 ICP-OES from Agilent, while to introduce the solutions the SPS 4 Autosampler was use, from the same company. Their pictures are shown in Figure 3.3.

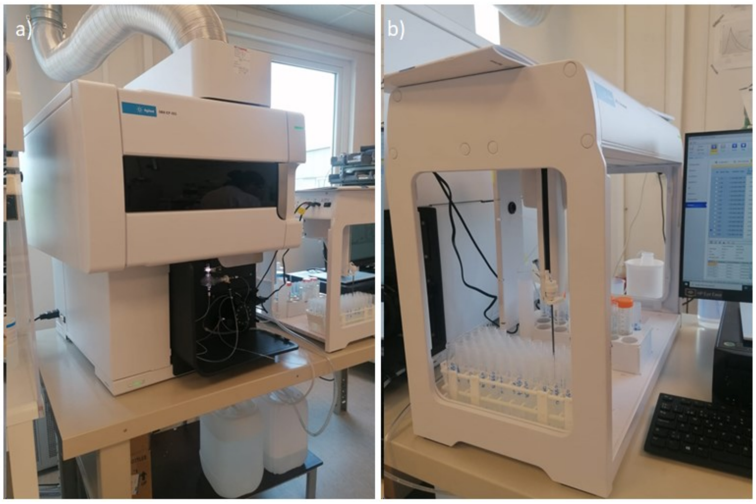

Fig. 3.3 Pictures of a) 5800 ICP-OES and of b) SPS 4 Autosampler.

3.3.4 *X-ray diffractometry*

X-ray diffraction, XRD, was adopted to identify the crystalline phases and determine the particle size in the various samples.

To explain the diffraction phenomenon, it is possible to apply the Bragg law, which provides a geometric relationship in order to observe diffraction of a wave for a certain scattering angle or not. Let’s imagine to have a crystal, therefore a solid made up of particles which are arranged in a regular and orderly manner in space, repeated indefinitely along the three dimensions. Such crystal is composed of parallel crystalline planes, on which the particles lie, separated by a certain interplanar distance, *d*. Suppose we have a monochromatic electromagnetic radiation with a certain wavelength, λ, incident on the planes with a certain reflection angle, also called Bragg angle, θ.

The electromagnetic waves can be reflected by the first crystalline plane, or be transmitted through this and interact with the second one, on which they can then be transmitted or reflected. The radiations obtained from the reflection on the various crystalline planes will add up in a phenomenon called interference. It can be destructive, leading to wave cancellation, or constructive, forming a wave with double amplitude. The latter is possible only if the difference in optical path among the reflected radiations is equal to a multiple of their wavelength. According to this criteria, the geometric relationship is obtained, that allows the constructive occurrence of the waves only for specific Bragg angles, calculated using Equation 2.6.

$$2d\ sen\theta = n\lambda \qquad n \in N \qquad \text{(Eq. 2.6)}$$

Each crystal consists of a large quantity of families of parallel crystalline planes, all with a specific interplanar distance, therefore, based on the pattern returned by the diffractogram, it is possible to trace back the observed crystalline phase, through comparison with a library. Based on the description just provided, it is obvious that, to have diffraction of electromagnetic radiation, it is first necessary to have an ordered pattern of the particles that form the solid, therefore diffractometry is not able to analyze disordered, so amorphous, phases.

Generally, the diffractograms are reported as the intensity of the diffracted radiation in relation to the diffraction angle, 2θ, which is the angle observed between the direction of propagation of the incident radiation with the direction of propagation of the diffracted radiation, so equal to double of the Bragg angle.

The Scherrer equation, shown in Equation 2.7, allows to relate the average size of the crystallites along the perpendicular direction to the family of crystalline planes, *L*, with the width of the peak at half height generated by this family in the diffractogram, β.

$$L = K\frac{\lambda}{\beta\ cos(2\theta)} \qquad \text{(Eq. 2.7)}$$

The constant *K* expresses the symmetry of the unit cell that forms the crystalline lattice, typically equals to 0.9.

To start the analysis, we proceeded with grinding a small arbitrary amount of sample with mortar and pestle, in order to expose all the crystalline planes which made up the crystalline lattice. Subsequently, a certain amount of ethyl alcohol was added to the ground powder, depositing the suspension drop by drop onto a silicon holder with a pipette, trying to get the most homogeneous deposition as possible by giving delicate lateral taps to the holder. Once the solvent had completely evaporated, the holder was inserted into one of the six available ports in the machine, to carry out the measurement.

The analysis was performed by using D2 Phaser, supplied by the company Bruker, collecting the signal from 10 up to 90°, with a step of 0.02°, for a total measurement time of approximately 1h. To generate the radiation, an X-ray tube was used, targeting a copper plate, hit by an electron beam, accelerated by a voltage difference of 30kV and an intensity of 10mA. Subsequently, the beam is monochromatized with an appropriate monochromator, selecting the wavelength equal to 1.54184Å, Cu Kα. The processing of the diffractograms was carried out with the EVA software, allowing the identification of the phases through comparison with the PDF-4 2017 database and the determination of the crystallite size. Figure 3.4 shows D2 Phaser and a magnification of its interior.

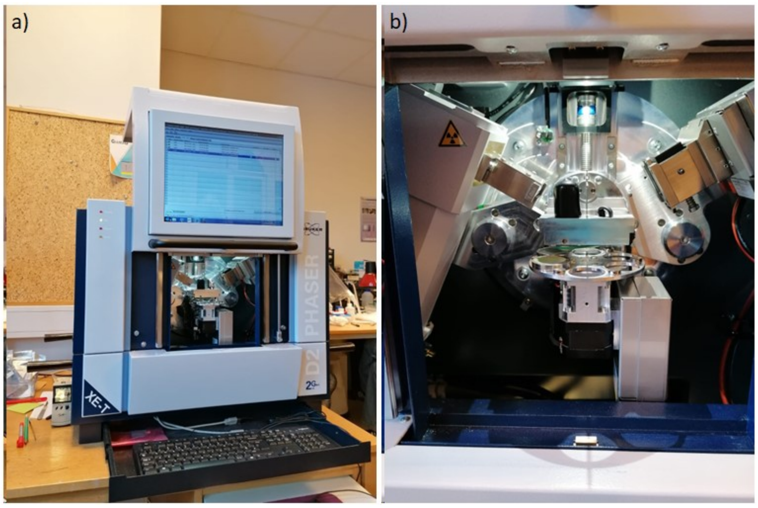

Fig. 3.4 Picture of a) D2 Phaser and b) a magnification of its inner.

3.3.5 *Temperature-programmed reduction*

Temperature-programmed reduction, TPR, was carried out to analyze the reducibility of the catalysts and, in particular, the interaction between the phase containing the active metal and the support, by reducing the calcined sample with hydrogen on a thermal ramp.

The temperature was increased from room temperature up to 900°C in an atmosphere rich in hydrogen, while the reduction of the oxide phase was observed as soon as it is spontaneous, therefore with a negative Gibbs free energy, *G*. Equation 2.8 calculate the Gibbs free energy from the standard Gibbs free energy and the partial pressure of water and hydrogen.

$$G = G_0 + RT\ ln\left(\frac{P_{H_2O}}{P_{H_2}}\right) \qquad \text{(Eq. 2.8)}$$

In some cases, the reduction is possible even if the standard Gibbs free energy is positive, since the partial pressure of water, P_{H_2O}, is particularly low, allowing the logarithmic term to be dominant, especially at high temperatures.

Sometimes the reduction immediately involves the formation of the metallic phase, while in other cases the formation of a further oxide can be observed, with a lower oxidation state than the previous one, thus resulting in an intermediate in the final reduction to metal.

The interaction between the oxide phase and the support is fundamental during the reduction, in fact the greater is the strength of the interaction and the lower is the tendency for the oxide to reduce, due to the stabilization caused by that, therefore leading to the appearance of the reduction peak at higher temperature. Interestingly, smaller oxide particles involve a stronger interaction with the support, so they are reduced after larger particles, resulting in lower reducibility. A further case is that of the formation of a mixed oxide, resulting from the chemical reaction between the oxide phase and the support, such as the creation of aluminate or silicate on an alumina or silica support, leading to the formation of reduction peaks at very high temperatures, with consequent decrease in reducibility.

The reduction also depends on the nucleation speed of the created metal phase. In fact, if it is slow, there would be greater initial difficulty in the reduction, due to the need to form the metal nucleation centers, followed by a rapid increase due to growth of these. If rapid, however, a very rapid reduction would be observed immediately, since the formation of nuclei is not a particularly high obstacle. After the reduction of the particle surface, the reduction of the bulk oxide will proceed, which will be definitely slower due to the decrease in the reaction interface as it proceeds.[26,97]

To begin the measurement, we proceeded by introducing exactly 0.15 g of sample into a quartz U-tube, on the bottom of which quartz wool had been placed to retain the sample, avoiding its dispersion in the machinery. Once the tube had been carefully connected to the analyzer, we proceeded by flowing the gas used for the reduction, containing 10% by volume of hydrogen in nitrogen, with a flow rate equal to 2,231 mmol/min, heating up to 900°C with a thermal ramp of 10°C/min by means of a cylindrical heating mantle. Once the final temperature had been reached, it was maintained for a total of 50 minutes. The acquisition was carried out every 0.1 s by a thermal conductivity detector, TCD, able to record the quantity of consumed hydrogen through the variation of thermal conductivity of the effluent gas. The detector was protected from the humidity, developed during the reduction, by passing the gas into a cryogenic trap containing ice and salt, at a temperature lower than -10°C, allowing the capture of water.

The employed machine for the analysis was 3Flex by Micromeritics, properly calibrated by reducing a sample of silver oxide. Figure 3.5 shows 3Flex and the U-tube used for the analysis.

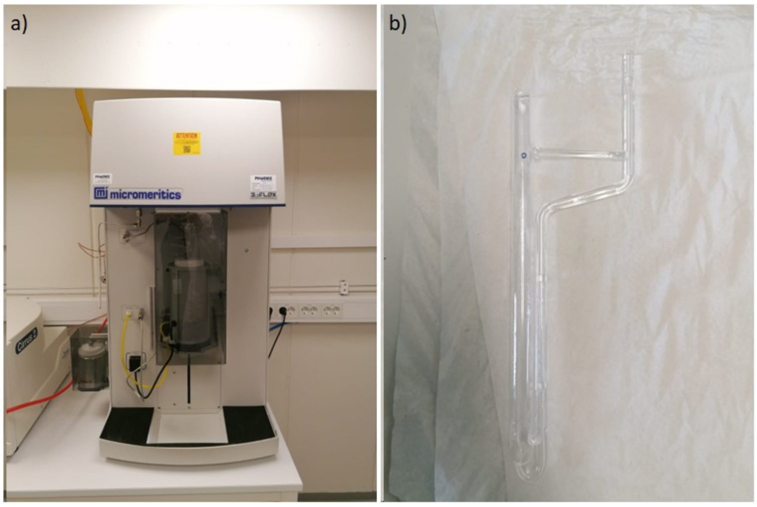

Fig. 3.5 Pictures of a) 3Flex and of b) the U-tube used for the TPR analysis.

3.3.6 *Static chemisorption of hydrogen*

Static chemisorption of hydrogen was carried out to determine the active area, made available by the metal, and to calculate the dispersion, defined as the percentage of surface atoms compared to the total ones. Generally, a greater dispersion is connected with a greater metal area, for the same loading, giving a higher number of active sites, so increasing the conversion of the catalyst.

To analyze the metal surface, it is necessary to isolate the quantity of adsorbed hydrogen relating only to the formation of the monolayer in contact with the solid. However, during the process we observe both the chemisorption of hydrogen to form the first layer and the physisorption of further hydrogen on that already chemisorbed, forming additional layers, making the determination of chemisorbed hydrogen alone complicated.

To solve this issue, the sample is degassed, allowing the removal of the physisorbed hydrogen, but not the chemisorbed one, and a further adsorption is carried out. In this case, since the chemisorbed hydrogen was already present on the sample, the resulting isotherm is related only to the physisorbed one. This procedure allows the repeated isotherm to be subtracted from the first one, obtaining the adsorption isotherm relating only to chemisorption. Generally, the shape of the isotherm follows the Langmuir model, idealizing the formation of a monolayer, being able to determine the volume of chemisorbed hydrogen, V_m, drawing a tangent to the plateau obtained at high relative pressures and obtaining the desired value from the intercept on the y-axis.

To determine the active metal area, A_m, it is necessary to know the number of moles of chemically adsorbed gas, n_a, obtainable from the volume of chemisorbed hydrogen, and the area occupied by the single adsorbate, A_g, also called cross-section of the adsorbate, equal to 0.123 nm^2 for hydrogen. Equation 2.9 shows the calculation of the active metal area.

$$A_m = F_s n_a N_A A_g \qquad \text{(Eq. 2.9)}$$

The coefficient F_s is called stoichiometric factor and is related to the adsorbed specie and the metal, taking on a value of 2 in case of hydrogen on a large variety of metals.

To calculate the dispersion of the metal, $\gamma_{\%}$, it is necessary to know, in addition to the volume of chemisorbed hydrogen, also the molar volume of hydrogen, V_{mol}, both expressed in standard conditions, the metal loading in the catalyst, $M_{\%}$, introduced during the synthesis, and the atomic mass of the metal, W_a. Equation 2.10 shows the calculation of the dispersion of the metal.

$$\gamma_{\%} = \frac{N_s}{N_T} \cdot 100 = \frac{V_m / V_{mol}}{M_{\%} / W_a} F_s \cdot 100 \cdot 100 \qquad \text{(Eq. 2.10)}$$

Finally, the average diameter of the active particles, d, is in relation to the metal area, dispersion, and metal density, ρ. Equation 2.11 shows the calculation of the average diameter of the active particles.

$$d = \frac{6}{A_m \, \gamma_{\%} \, \rho} 100 \qquad \text{(Eq 2.11)}$$

Note that the adopted expression to calculate the average size of the particles requires them to be spherical, however it is possible to easily change the expression to consider other geometries. In particular, the results reported by the characterization are expressed for hemispherical particles.

To carry out the measurement, we started by weighing exactly 0.15g of calcined catalyst and introducing it into a U-tube, the same used in the temperature-programmed reduction, with quartz wool on the bottom, and to connect it to the machinery. At this point pure hydrogen was flowed and the set reduction temperature was reached with a thermal ramp of 10°C/min, by means of a cylindrical heating mantle, maintaining for 30min in order to have complete reduction of the oxide to form the metallic phase. Subsequently, the temperature was lowered to 35°C, within which the adsorption took place, and the sample was evacuated, making sure to have a surface free from adsorbates. The two hydrogen adsorptions were carried out, interspersed with degassing to ensure the removal of the physisorbed hydrogen, measuring the quantity of adsorbate using a thermal conductivity detector, TCD. At the end, the sample was reweighed, appropriately subtracting the tare.

The reduction temperature was chosen starting from the profile obtained from the temperature-programmed reduction, in order to use the minimum temperature that allows the formation of the metallic phase, in order to limit the sintering of the particles as much as possible, which would lead to their aggregation, compromising the analysis.

Table 3.3 Reduction temperature applied for the metal formation before the hydrogen chemisorption.

Catalyst	Temperature of reduction (°C)
15Ni/Alumina_IWI_550	650
15Ni/Alumina_WI_550	650
15Ni/Alumina_IWI_850	850
15Ni/Alumina_WI_850	850
15Ni/TitaniaP25_550	550
15Ni/TitaniaP25_850	700
15Ni/Anatase_550	550
15Ni/Anatase_850	700
15Ni/Zirconia_550	600
15Ni/Zirconia_850	600
15Co/Alumina_IWI_550	650
15Co/Alumina_WI_550	650
15Co/TitaniaP25_550	500
15Co/Anatase_550	500
15Co/Zirconia_550	600
15Ni/13X_450	500
15Ni/4A_450	500

The reduction temperature for the catalysts with a 10% metal loading was the same as for the corresponding 15% ones reported in Table 3.3. The same is applied for the promoted catalysts to the correspondent unpromoted, at the same calcination temperature.

A Micromeritics 3Flex instrument, calibrated with a reference of platinum-aluminum alloy, was used for this type of measurements. Figure 3.5 shows 3Flex and the U-tube used for the analysis.

3.3.7 *Thermogravimetric analysis*

Thermogravimetric analysis, TGA, were carried out to study the adsorption capacity of the zeolites.

The measurement consists in exposing a sample of zeolite to an atmosphere containing the gas to be adsorbed, recording the quantity of captured adsorbate by the material through the variation in its mass. The adsorption process cannot be infinitely rapid, therefore a progressive increase in mass is observed, until equilibrium conditions are reached. At this point, the adsorption speed is equal to the desorption speed, resulting in saturation of the zeolite with adsorbate.

The determination of the water adsorption capacity of the zeolites is of particular interest, which is calculated with Equation 2.12.

$$C_{H_2O} = \frac{\Delta m}{m_i} \qquad \text{(Eq. 2.12)}$$

The expression includes the mass variation, starting from exposure to water vapor, when saturation is reached, Δm, and the initial mass, which is the mass of the zeolite sample without humidity, m_i.

To begin the analysis, an arbitrary amount of zeolite, in beads, was weighed, between 30 and 40mg. Then it was introduced into a small refractory alumina crucible, which was hung to a platinum wire, connected to the analytical balance, inside the tubular furnace within which the exposure took place. This was followed by heating the supply pipe to 150°C, in order to have a pre-heating of the gaseous mixture before being introduced into the chamber, thus also avoiding the possible condensation of the water vapour. Before measuring, the humidity was eliminated from the zeolite by flowing 500mL/min of nitrogen at the analysis temperature for a total of 30min.[85] Next, the gas introduced into the chamber was changed with the desired one, maintaining the same flow rate, for an exposure time of 20min.

A series of measurements were carried out at 200°C at different water vapor concentrations, 10 vol.%, 20 vol.%, 30 vol.% and 40 vol.% water in nitrogen, in order to study the saturation trend in relation to the water content. In addition, another series of measurements were carried out at different temperatures, from 100°C up to 350°C (every 50°C), using 40 vol.% water in nitrogen.

Similarly, analyses were carried out by exposure of carbon dioxide and hydrogen with a concentration of 40 vol.% in nitrogen. The measurement in hydrogen was performed at 100°C, while the ones in carbon dioxide were done up to 250°C, with the aim to verify the adsorption of the reagents, in other words their capture and sequestration from the reaction.

To conclude, the stability of zeolites was determined by performing 30 cycles of adsorption, for 20 minutes, and desorption, for 30 minutes.[85] Using the 40 vol.% water vapor concentration at 200°C and 300°C.

The instrumentation used was home-made, consisting of a MK2-M5 Vacuum Head microbalance connected to the DISBAL Control Unit, both by C.I. Electronics Ltd, and an EVA 12/150B tube furnace from Carbolite Gero controlled by the 3216 unit from Instron. The crucible had a diameter of 8 mm and a height of 10 mm. Figure 3.6 shows the home-made instrumentation.

Fig. 3.6 Picture of the home-made thermogravimetric instrumentation.

3.3.8 *Scanning electron microscopy*

To study the morphology of the surface of the catalysts, we used scanning electron microscopy, SEM, while the distribution of the elements on the single particle was determined by using SEM-EDX (energy dispersive X-ray).

The analysis is based on hitting the sample with an electronic beam, generated by an emitter through the thermionic effect or field effect, accelerated by a desired voltage difference, moving the focus hotspot to scan the surface. There are three collected signals, which are backscattered electrons, secondary electrons and X-rays, allowing the collection of a lot of information, including the morphology and the chemical analysis of the material.

The backscattered electrons are electrons of the incident primary beam, deflected from their trajectory by the interaction with the nuclei of the atoms that make up the sample. In particular, those that return back, in the opposite direction of the incident beam, are analyzed. The entire phenomenon can be considered as an elastic diffusion, since these electrons possess the same energy as the incident primary electrons, due to no energy exchange. Backscattered electrons are typically used to create an image of the surface of the solid, however they are also sensitive to its composition, since heavier atoms have a greater nuclear charge, therefore they are able to modify more easily the trajectory of the electrons, returning a more intense signal, while also being able to provide quantitative indications about the elements.

Secondary electrons are electrons from the core levels of the atoms that make up the sample, expelled due to the collision with the electrons of the primary beam with which they exchanged energy. This phenomenon can be considered an inelastic diffusion, since the energies of the electrons are different from each other. The secondary electrons are used to determine the morphology, examining and returning an image of the surface of the solid, since their intensity depends on the neighborhood of the emission point. By irradiating a cavity in the surface, a greater amount of material is all around the point from which the secondary electrons emerge, leading to a greater probability that these enter the solid and be dissipated, resulting in a lower collection of electrons by the detector, therefore a lesser signal intensity, denoted by a dark area. On the contrary, for a protrusion, the quantity of material around it is definitely smaller, with a lower probability that the secondary electrons collide with the solid, remaining stuck in it, returning a greater quantity of electrons, so a more intense signal, characterized by a light area.

Typically, the images obtained from secondary electrons are rather flat, making their interpretation quite difficult, therefore, in order to recover part of the sense of depth, both images with secondary and backscattered electrons are collected, having a more complete picture of the sample surface.

The same phenomenon that involves the emission of secondary electrons also leads to the formation of electronic holes in the core levels of the atoms, inside the sample, which are in a non-equilibrium condition, wanting to fill these holes through electronic transitions of electrons from higher energy orbitals, with consequent emission of photons due to fluorescence phenomenon. Since the orbitals involved are atomic, the radiation emitted has the frequency of X-rays, providing information about the chemical nature of the atom, since the energy of the radiation is characteristic of its orbitals, unique for each element. Through the analysis of the characteristic spectrum and its intensity, it is possible to obtain information both on the chemical composition of the solid and on the quantity of the elements that constitute it, thus carrying out the EDX analysis.

Microscopy is also dependent on the characteristics of the employed primary beam. Indeed, it is necessary to modulate the voltage difference to optimize the image. If the applied accelerating voltage is excessively high and the material, which made the solid, is not so electrically conductive, such as an insulator, the electrons would accumulate on it, causing the formation of artifices, which do not actually exist on the surface, being mistaken for characteristics of it. Generally, in these cases it is enough to lower the accelerating voltage, however if this is not sufficient, due to the insulating nature of the sample, it is possible to consider the coating with a layer of conductive material, for example gold or, even more simply, graphite. On the other hand, if the voltage difference is not sufficiently high, not enough energy would be provided for the expulsion of the electrons from the atomic orbitals, obtaining not only poorly resolved images from the secondary electrons, but also obtaining a minimal quantity of X-rays, insufficient for an adequate spectroscopic analysis. In this case, it is sufficient to increase the voltage difference. The accelerating voltage, therefore the energy of the incident beam, together with the composition of the solid, is also a fundamental parameter for the investigation depth of the microscopy, typically obtaining information relating to 1 μm of thickness.

To prepare the sample for microscopy, we lightly grinded it, in order to avoid aggregates, and attached the powder to an adhesive layer of carbon, placed on the base of a small steel cylinder. Since the analyzed material is an insulator, the adhered powder was covered with a layer of graphite in vacuum, by heating a carbon filament through passage of an electric current. After that, the samples were introduced into the electron microscope, each housed in a specific port of the holder, proceeding with focusing for the collection of images. At this point we proceeded to collect the images of the particles using backscattered and secondary electrons, adopting an accelerating voltage equal to 5 kV. Subsequently, the chemical information was collected using EDX in mapping mode, in order to observe the distribution of the elements, applying a voltage difference of 15 kV, in order to guarantee the formation of electronic holes in the core levels.

To cover the powder with graphite, CED 030 Balzers carbon evaporator by Bal-Tec was used, while we used the JSM-7900F electron microscope by Jeol, which has a Schottky emitter, with a resolution of 0.6 nm at 15k V, coupled with EDS 65 Advanced system by AZtecLive for the X-ray analysis, determining elements heavier than beryllium. Figure 3.7 shows JSM-7900F electron microscope and CED 030 Balzers carbon evaporator.

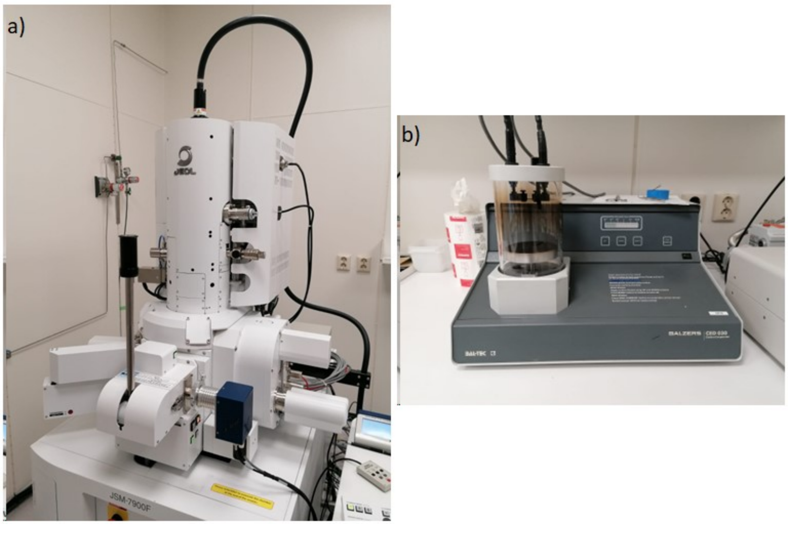

Fig. 3.7 Pictures of a) JSM-7900F electron microscope and of b) CED 030 Balzers carbon evaporator.

3.4 *Catalytic activity*

In order to study the performance of the catalysts, compare their stability and investigate the possible improvement through the application of zeolites, a series of catalytic tests were carried out on a packed bed reactor, PBR, examining the effluent gas by using a gas analyzer.

The reactor consists of a quartz tube, 50 cm long and 1 cm in diameter, having a constriction in the middle with a 0.5 cm thick porous septum, necessary to retain the powder catalyst and create the fixed catalytic bed. The tube is surrounded by a cylindrical heating mantle to maintain the desired temperature, controlled by a thermocouple inserted inside the bed.

Before analysis, the in-situ reduction of the catalyst was performed, using a gaseous mixture containing 10 vol.% of hydrogen in nitrogen, with a flow rate of 200mL/min for 30min. The reduction temperature was chosen based both on the reduction profile of the calcined catalyst, determined by the temperature-programmed reduction, and on the desire to keep this temperature as constant as possible among the various samples, in order to achieve an adequate comparison. For this purpose, we normally used 650°C, varying only if at that temperature was is not possible to reduce the oxide phase containing the active metal.

Table 3.4 Reduction temperature applied for the metal formation before the catalytic test.

Catalyst	Temperature of reduction (°C)
15Ni/Alumina_WI_550	650
15Ni/Alumina_WI_850	850
15Ni/TitaniaP25_550	650
15Ni/Anatase_550	650
15Ni/Anatase_850	700
15Ni/Zirconia_550	650
15Ni/Zirconia_850	650
15Co/Alumina_WI_550	650
15Co/Anatase_550	650
15Co/Zirconia_550	650
15Ni/13X_450	500
15Ni/4A_450	500

The reduction temperature for the catalysts with a 10% metal loading was the same as for the corresponding ones with 15% metal loading reported in Table 3.4. The same was applied for the promoted-containing catalysts and the corresponding without promotor.

In a typical experiment, the reagent gas entered from the top of the tube and exited from the bottom, flowing through the fixed bed. At the exit, an ice-cooled condenser was present, in order to remove the water vapor from the effluent gas, which could interfere or damage the sensors of the analyzer, used for the determination of the concentration of the species.

Assuming that there is no accumulation of carbon in the catalytic bed, so there is no deposition of carbon coke, and that the temperatures of the gas entering the alimentation system and exiting the condenser are the same, we calculated the conversion of carbon dioxide, shown in Equation 2.13, the selectivity towards methane, shown in Equation 2.14, the selectivity towards carbon monoxide, the major by-product of the reaction, shown in Equation 2.15, and the methane yield, shown in Equation 2.16, from the percentage concentrations of the species in the effluent gas.

$$C_{CO_2} = \frac{\%CO_{\ out} + \%CH_{4\ out}}{\%CO_{2\ out} + \%CO_{\ out} + \%CH_{4\ out}} \qquad \text{(Eq. 2.13)}$$

$$S_{CH_4} = \frac{\%CH_{4\ out}}{\%CO_{\ out} + \%CH_{4\ out}} \qquad \text{(Eq. 2.14)}$$

$$S_{CO} = \frac{\%CO_{\ out}}{\%CO_{\ out} + \%CH_{4\ out}} \qquad \text{(Eq. 2.15)}$$

$$R_{CH_4} = \frac{\%CH_{4\ out}}{\%CO_{2\ out} + \%CO_{\ out} + \%CH_{4\ out}} \qquad \text{(Eq. 2.16)}$$

Each catalyst was tested to determine its performance and to compare it with the others, in order to understand which combination of factors allowed for the best outcome. In a typical activity test, 150 mg of catalyst and 750 mg of crushed and sieved quartz were introduced into the quartz tube. The quartz particles had a size between 300 μm and 1000 μm and were used to dissipate the heat released by the exothermic reaction.[3] Before the analysis, the feed system was heated up to 150°C to preheat the gases.

After the reduction, the temperature was lowered to approximately 300°C and the reagent gaseous mixture, consisting of hydrogen and carbon dioxide with a volumetric ratio of 4:1 was introduced. A total flow rate of 200 mL/min was used. Gradually, the temperature was increased to 350°C and, having reached the steady state, the percentage concentrations of the species in the effluent gas were collected every 2 minutes for a total of 20 minutes of measurement. At the end of the analysis, the heating mantle was turned off and a mixture of 25 mL/min of hydrogen and 100 mL/min of nitrogen was introduced into the reactor, in order to avoid oxidation during the cooling down process. At 50°C, the gas flow was stopped and the catalyst was extracted from the tube.

For the stability measurements, we proceeded in a similar way. However, at the end of the 20 minutes measurement the gaseous mixture was not changed. Instead, the reaction was continued for further 70 h, without changing the set temperature. At the end of this period, we proceeded with the adjustment of the temperature, if it had changed, returning it to 350°C and reaching the steady state, then collecting data for 20 minutes every 2minutes. The shutdown of the reactor was performed in the same way described above.

To conclude, the catalyst was analyzed in the presence of zeolite in the reactor. In this case, the 750 mg of quartz were replaced by an equal amount of crushed and sieved zeolite, with dimensions between 200 µm and 300 µm. After the usual in situ reduction, the methanation took place in the same conditions previously described, with the only difference that at the end of the 20 minutes analysis, the set temperature was brought to 300°C and the reagent gas was replaced with 10 vol.% hydrogen in nitrogen, with a flow rate of 200mL/min, for a total of 30 minutes, in order to desorb the water in the zeolite, avoiding the oxidation of the metal during its release. At the end, the reagent gas was reintroduced and the temperature was raised to 350°C, to carry out a second analysis. This was repeated for a third time before shutting down the reactor, in order to understand if there had been a performance decrease due to degradation of the sorbent.

Finally, the same cycle of three methanations was carried out at different working conditions, listed below:

- 150 mg of catalyst and 750 mg of zeolite, 300°C and 200 mL/min of a hydrogen and carbon dioxide mixture with a 4:1 volumetric ratio;
- 150 mg of catalyst and 750 mg of zeolite, 300°C and 100 mL/min of a hydrogen and carbon dioxide mixture with a 4:1 volumetric ratio;
- 75 mg of catalyst and 825 mg of zeolite, 300°C and 100 mL/min of a hydrogen and carbon dioxide mixture with a 4:1 volumetric ratio;
- 150 mg of catalyst and 750 mg of zeolite, 300°C and 100 mL/min of a hydrogen and carbon dioxide mixture with an 8:1 volumetric ratio.

It is recalled that for each measurement carried out in the presence of zeolite, a similar reference measurement was carried out in its absence, maintaining the same working conditions, but replacing the zeolite with quartz, in order to ascertain an improvement or otherwise in reactivity.

The SICK GMS820P gas analyzer was used to carry out the analyzes, which contains a MULTOR non-dispersive infrared sensor, to determine the concentration of methane, carbon monoxide and carbon dioxide, and a THERMOR thermoconductive sensor, for hydrogen analysis.

The temperature control was carried out manually, adjusting the mantle temperature to ensure that the one recorded by the thermocouple, inserted in the catalytic bed, was as close as possible to the desired one, with a deviation of approximately ±2.5°C. To read the values of temperature, the mantle was connected to the 3216 control unit, while the thermocouple was connected to the 2416 unit, both from Eurotherm. Figure 3.8 shows the reactor, condenser and SICK GMS820P gas analyzer.

Fig. 3.8 Pictures of a) reactor and condenser, and of b) SICK GMS820P gas analyzer.

Due to lack of time, each catalytic test was performed only once, carrying out the traditional methanation test three times only for the most active catalyst, calculating the maximum half-dispersion for the conversion, selectivity and yield, by using Equation 2.17.

$$\Delta x = \frac{x_{max} - x_{min}}{2} \quad \text{(Eq. 2.17)}$$

4. CHARACTERIZATION

4.1 *Supports*

It is essential to know the properties of the supports used in the syntheses, since their interaction with the active phase can drastically change its reactivity, influencing a multitude of parameters.

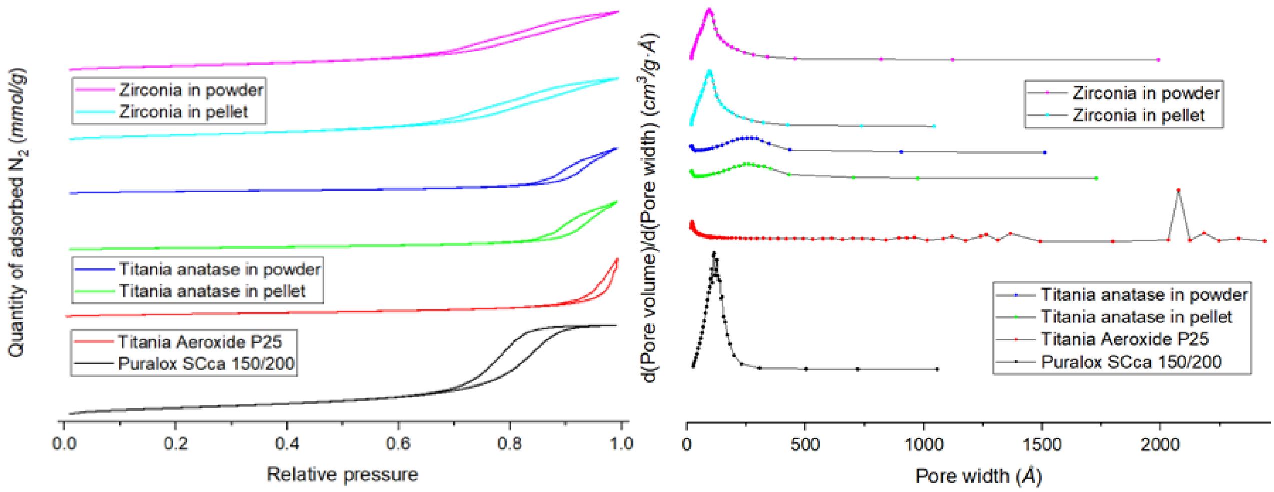

Fig. 4.1 Images of the isotherms, on the left, and of the pore size distribution, on the right, of the supports.

Figure 4.1 shows the adsorption isotherms and the pore size distribution curves for the different supports, while the values extracted from the analysis are reported in Table 4.1. It is observed that the adsorption and desorption processes are irreversible on all supports, which means that the quantity of adsorbate measured during the adsorption and desorption is not the equal at the same relative pressure. This is caused by the capillary condensation inside the pores, generating type IV isotherms, typical of mesoporous solids.[3,4,6,33,50,62,67,69,78,80,87,98–100]

Table 4.1 Textural properties of the supports.

Support	**Surface area (m^2/g)**	**Pore volume (cm^3/g)**	**Average pore diameter (nm)**
Alumina	154.4	0.46	12.0
TitaniaP25	47.6	0.28	20.2
Anatase in pellet	45.0	0.24	21.1
Anatase in powder	42.8	0.22	20.8
Zirconia in pellet	114.6	0.32	11.1
Zirconia in powder	107.3	0.30	11.3

Among all the materials, Alumina shows the highest surface area (154.4 m^2/g) and total pore volume (0.46 cm^3/g), with a narrow and unimodal pore size distribution, around 12.0 nm.[79] Zirconia supports have a slightly lower surface area and pore volume, due to the greater compactness, and a narrow unimodal pore size distribution, around 11.3 nm.[61] Titania samples, on the other hand, have smaller surface area (~ 45 m^2/g) and pore volume (~ 0.24 cm^3/g).

For Anatase, it is possible to note a bimodal pore size distribution, in particular there are some micropores, with a maximum at 1.9 nm, and mainly mesopores, with a maximum peak at around 26.0 nm. The calculation of the average takes into account both populations, resulting in a value slightly lower than that of the maximum for the mesopores, showing how these are more numerous.

TitaniaP25 has macropores, centered at 207.5 nm, but also a significant presence of micropores, with a maximum of 2.0 nm, and a very slight quantity of macropores with dimensions between 75 nm and 150 nm, which allow to reduce the calculated average diameter. The large presence of macropores for TitaniaP25 is caused by the presence of rutile, a stable crystalline phase for large titania crystallites, producing large interstices between particles, unlike anatase, stable for smaller crystallites, forming smaller gaps.[71]

By comparing the pellet and powder supports, it can be observed that grinding does not cause any drastic change in the textural properties, negligibly lowering all the physical parameters of interest, due to the breaking of the particles along the pores inside them.

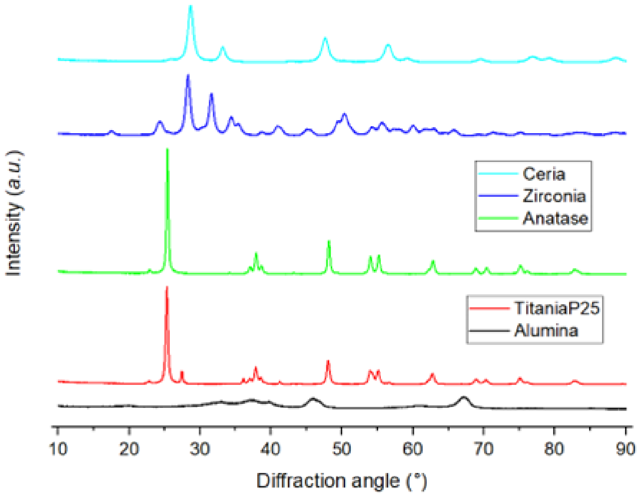

Fig. 4.2 Diffractograms of the supports and of the ceria reference.

Figure 4.2 shows the X-ray diffractograms of the supports, used to determine the phases in the samples. Alumina exhibits three major peaks, at 37.6°, 45.9° and 66.9°, characteristic of the (311), (400) and (440) crystalline planes of the γ phase, one of the most porous polymorphs of this oxide.[43,78,80,99,101,102]

TitaniaP25 is made up of a mixture of anatase and rutile, both with a tetragonal crystalline lattice, deduced from the co-presence of the peaks at 25.4°, characteristic of the (101) crystal plane of anatase, and 27.6°, characteristic of the (110) crystalline plane of rutile. The latter has a lower intensity due to the lower content. Characteristics for anatase are also the peak at 48.2°, of the (200) plane, and three peaks centered around 37.9°, caused by planes (103), (004) and (112). The second most intense peak of rutile is the one at 36.2°, characteristic of the (101) plane. In case of Anatase sample, only the peaks related to the anatase phase are observed, not noting any traces of other crystalline structures, such as rutile or brookite.[35,84,94]

Zirconia shows a large multitude of peaks, characteristics of the monoclinic phase, called baddeleyite, in particular the three largest ones at 28.3°, 31.5°and 50.2°, characteristic of the (-111), (111) and (022) crystalline planes. No tetragonal and cubic phases are identified, which are the other two most recurrent stable phases of zirconia.[61,65,66,70,103,104]

It should be noted that the peaks relating to Alumina are rather broad and not very intense, typical of small particles, in accordance with the Scherrer equation, favoring the porosity of the material. On the contrary, the anatase and rutile peaks for the two titania supports are very intense and sharp, typical of larger particles, creating bigger pores and reduced porosity.[6,48,80,87,101,105]

To conclude, the ceria pattern shows the occurrence of cerianite, which is a cubic crystalline structure of the oxide, evidencing the peaks at 28.6° and 47.5°, characteristic of the (110) and (022) crystalline planes.[60,87]

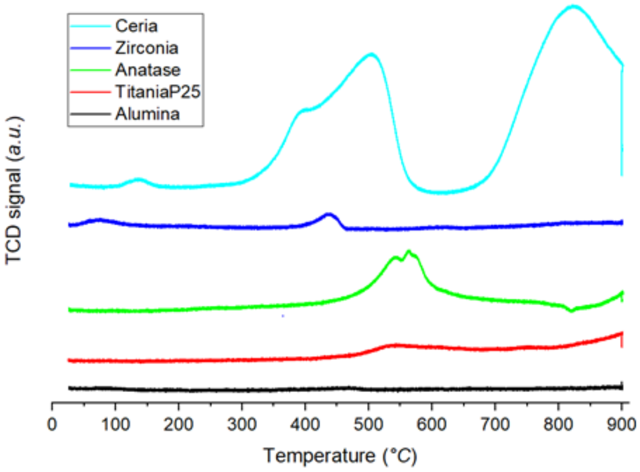

Fig. 4.3 Reduction profile of the supports and of the ceria reference.

Figure 4.3 shows the reduction profile of the supports, needed to analyze their reducibility properties. Alumina does not exhibit any reduction peak in the temperature range studied as expected, since it is not a reducible oxide.[106] However, all the other supports shows reduction processes that can be associated to the formation of reticular oxygen vacancies, due to a change in the oxidation state of the metal from +4 to +3. These oxygen vacancies are fundamental, since they act as adsorption sites for carbon dioxide, allowing its activation by weakening the bond between carbon and oxygen, making it more disposed to hydrogenation.[31,60]

For TitaniaP25, no particularly intense peaks are observed, since the rutile is not as reducible as anatase. In fact, by comparison with Anatase, a drastic difference in the intensity of the reduction peak is observed, in favor of the latter centered at 550°C.[105]

Zirconia shows a not very intense reduction peak, but located at lower temperatures, with a maximum at 435°C. This proofs that, although not much oxide is reduced, this process is quite favored.[103]

To conclude, the reduction profile of the ceria sample is also reported, showing two reduction peaks, respectively at low temperatures, between 300 and 580°C, due to the reduction of the superficial phase, and at high temperatures, over 670°C, due to the treatment of the bulk one. The reduction is definitely more intense than that of supports and also occurs at lower temperatures, proving that the introduction of cerium into a catalyst allows to gain excellent redox properties.[33,87]

4.2 *Nickel catalysts*

Once the properties of the catalytic support were determined, the nickel catalysts prepared on them were also characterized. In the following, the results obtained from the characterization are presented. These results enable us to isolate which combination of parameters results in the best properties.

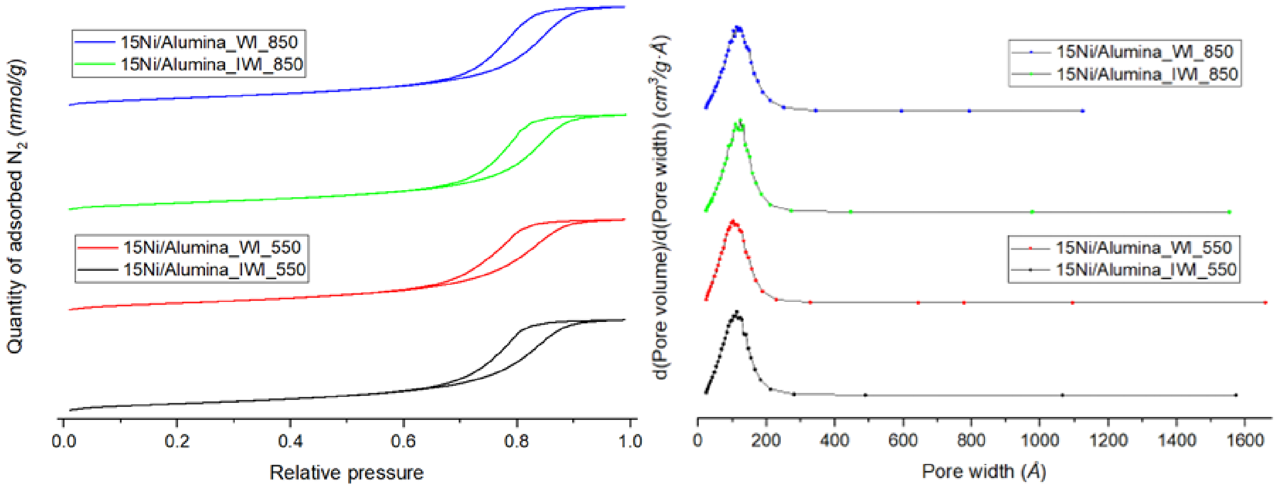

Fig. 4.4 Images of the isotherms, on the left, and of the pore size distribution, on the right, of the 15% nickel Alumina-based catalysts.

Table 4.2 Textural properties and metal loading of the 15% nickel catalysts.

Catalyst	**Surface area (m^2/g)**	**Pore volume (cm^3/g)**	**Average pore diameter (nm)**	**Metal loading (%)**
15Ni/Alumina_IWI_550	124.4	0.35	11.1	15.0
15Ni/Alumina_WI_550	127.8	0.35	10.9	14.5
15Ni/Alumina_IWI_850	120.6	0.36	11.9	15.9
15Ni/Alumina_WI_850	127.9	0.37	11.7	15.8
15Ni/TitaniaP25_550	37.5	0.32	33.5	13.2
15Ni/TitaniaP25_850	1.3	0.01	30.5	14.1
15Ni/Anatase_550	33.9	0.17	20.4	10.8
15Ni/Anatase_850	5.1	0.02	16.0	13.4
15Ni/Zirconia_550	39.8	0.19	18.7	21.4
15Ni/Zirconia_550	11.5	0.13	46.5	18.4

Table 4.2 reports the textural properties of the nickel catalyst. Figure 4.4 shows the adsorption isotherms and the pore size distribution curves for the different Alumina-based nickel catalyst. For the Alumina-based catalysts, the surface area and pore volume slightly decrease after the nickel incorporation, compared to the support, due to the introduction of the metal inside the pores, leading to a partial filling.[3,4,12,24,31–33,50,51,62,69,73,76,78–80,87,89,96,99–101,103,104,106,107] The average pore size also decrease slightly due to partial occupation, allowing their shrinkage, but not their obstruction, which would have led to an increase in the average diameter, eliminating the population of pores with smaller dimensions, which are the first to be clogged. The possibility of obstruction cannot be ruled out, even if shrinkage is the predominant phenomenon, leading to an overall net decrease in the average size.[62] The unimodal distribution observed for the support is kept, meaning that the distribution of the precursor is uniform.[76]

The increase in the calcination temperature leads to an increase in the average pore diameter, bringing back to a value close to that of the support, due to the greater sintering of the nickel oxide particles, reaching larger dimensions which lead to easier obstruction. In the case under consideration, the effects of restriction and obstruction are equal and opposite, counterbalancing each other.[3,5,10,33,48,69,101]

While the average pore diameter seems to vary only due to the calcination temperature, being independent from the synthesis method, exactly the opposite is observed for the surface area. In fact, slightly higher values are obtained for the WI method.

It should be noted that the differences observed are minimal between the various synthesis methods and calcination temperatures, as they can easily be overridden by accidental errors that occur during the preparation of the catalysts. Consequently, it can be said with certainty that these parameters do not cause significant variations in the textural properties, pointing out that γ-alumina has a very high thermal stability, not leading to closure of the pores due to its sintering.

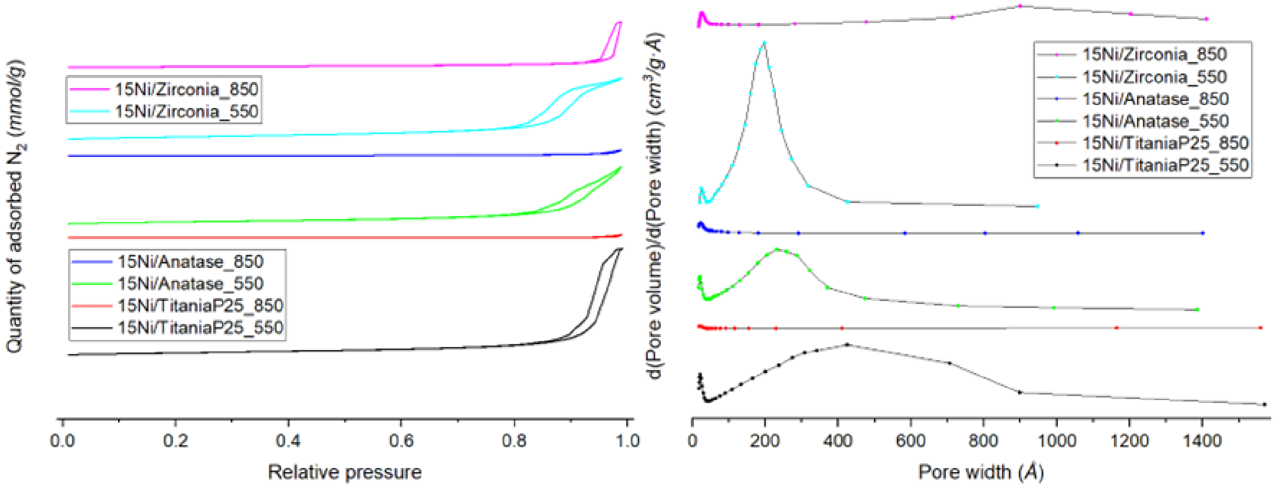

Fig. 4.5 Images of the isotherms, on the left, and of the pore size distribution, on the right, of the 15% nickel reducible supports-based catalysts.

Figure 4.5 shows the adsorption isotherms and the pore size distribution curves for the remaining nickel catalyst. Regarding the reducible supports, a decrease in the surface area and pore volume is detected after the introduction of nickel, with an increase in the average diameter, caused by filling and obstruction of the pores.[4,12,24,31,32,50,51,61,62,69,73,76,78–80,87,89,96,99–101,103,104,106,107] The only exception to this trend are the increase in pore volume for 15Ni/TitaniaP25_550 and the decrease in their average size for 15Ni/Anatase_550. In the first case, this is due to the deposition of a significant quantity of the nickel precursor on the external surface of the support particle, creating a porous structure, even if the deposition inside the pores of the material is not exclude. The second exception is easily understandable by assuming a narrowing of the pores, rather than their obstruction.[62]

Examining the distribution of the pores, micropores are found, demonstrating that the impregnation did not allow a homogeneous distribution of the metal, but rather resulted in a preferential filling of the outermost pores, keeping the more internal and smaller ones unchanged, causing the creation of a bimodal distribution. For 15Ni/Zirconia_550, the main peak is placed at larger diameters, 19.8 nm, due to the filling and closing of the smaller pores, while for 15Ni/TitaniaP25_550 and 15Ni/Anatase_550, smaller sized mesopores are observed, at 42.5 nm and 23.1 nm respectively, caused by the narrowing of macropores and mesopores. For 15Ni/TitaniaP25_550, it can also be hypothesized a porous deposition of nickel outside the support, allowing the fraction of mesopores to increase, helping in the creation of the broad peak at 42.5 nm.[71]

The comparison of the results at different calcination temperature is very interesting. A drastic change in the porosity of the materials occurs at higher temperature due to the sintering of the support, which involves the collapse of the smaller pores. This can be clearly observed by investigating the distribution of their diameter, whereby a shift of the peaks towards larger dimensions is observed, or even the lack of peaks in the case of titania supports, leaving only a minimal fraction of micropores and a few macropores of dimensions so large that they do not fall within the measurement range. The conclusion is that 15Ni/TitaniaP25_850 and 15Ni/Anatase_850 are not porous materials, while 15Ni/Zirconia_850 is porous due to the superior thermal stability of the support. The decrease in porosity involves a drastic decline in the surface area and pore volume, accompanied by an increase in their average size. However, a reduction of this value is observed for the two titania supports, compared to lower calcination temperatures. This is an artifice, since the calculation does not consider the presence of macropores larger than the upper measurement limit, instead taking into account the few micropores that remained intact during calcination.[3,5,6,10,50,51,61,63,64,69,82,84,101]

For all the catalysts studied, except for 15Ni/TitaniaP25_850 and 15Ni/Anatase_850, a IV type isotherms are obtained, typical of mesoporous materials. The exceptions cannot be included in any isotherm, since the amount of adsorbate is negligible, so they are not porous.[3–5,33,36,50,61,62,67,69,78,80,87,98–100,103]

The metal loading was determined by XRF analysis and the values are reported in Table 4.2. As observed, the values are very close to the nominal one. Only 15Ni/Anatase_550 and 15Ni/Zirconia_550 deviate from the nominal loading, showing a lower and higher value, respectively.

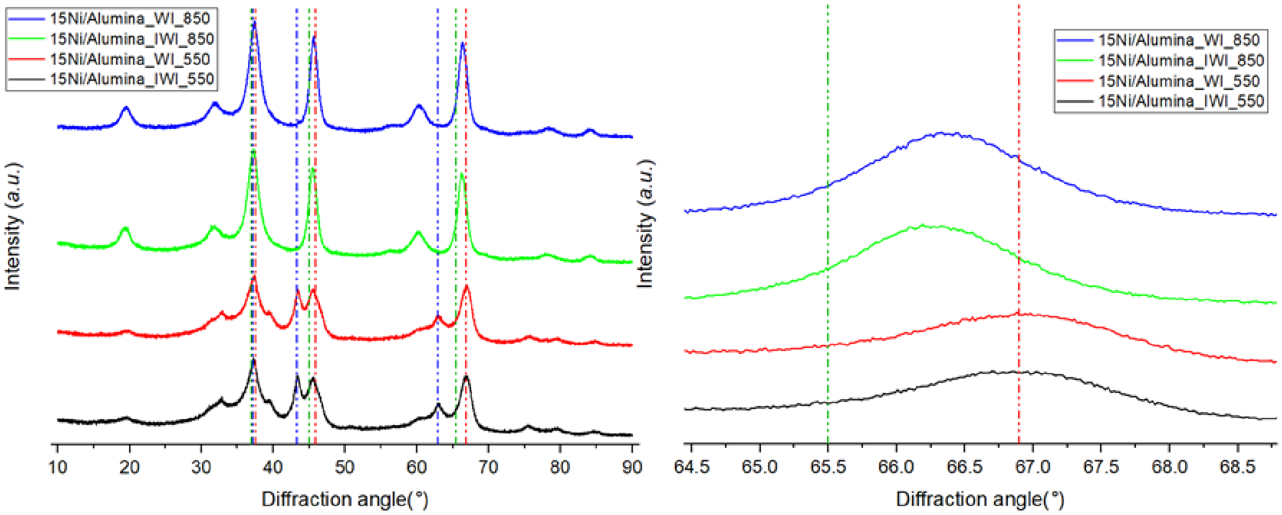

Fig. 4.6 Diffractograms of the calcined 15% nickel Alumina-based catalysts. The vertical dotted lines show the position of the main peaks of γ-alumina (red), nickel oxide (blue), and nickel aluminate (green). On the left, a magnification of the peaks around 66° is shown.

Figure 4.6 depicts the XRD patterns for the Alumina-based nickel catalyst. All the samples present the characteristic peaks of γ-alumina, confirming the stability of the support. No phase transformation to other polymorph occurs, for example forming α-alumina.[26,101,106,108] It is clear that there are no differences based on the synthesis method. Regarding the nickel, differences are observed with the calcination temperature. The presence of nickel oxide, NiO, is observed in the samples calcined at 550°C, confirmed by the presence of the peaks at 37.2°, 43.3° and 62.9°, characteristic of the (111), (200) and (220) crystalline planes. On the other hand, nickel aluminate, $NiAl_2O_4$, is formed at 850°C, showing peaks at 37.0°, 45.0° and 65.5°, characteristic of the (311), (400) and (440) crystalline planes. The formation of the mixed oxide is caused by the reaction between the nickel oxide with the γ-alumina, leading to the complete consumption of the first reagent.[3,4,10,29,31,37,47,50,67,69,99,105,106,108]

The formation of aluminate is caused by the diffusion of Ni^{2+} ions within the γ-alumina lattice, causing the expansion of the lattice parameters due to the larger size of nickel compared to aluminum. This results in a shift of the peaks to lower diffraction angles. This can be clearly observed by examining the peak at 66.9°, characteristic of the (440) crystalline plane of γ-alumina. The peak shifts to lower values due to the overlap with the peak of the mixed oxide, with increased reticular parameters.[2,7,26,37,87,97,99,100,108]

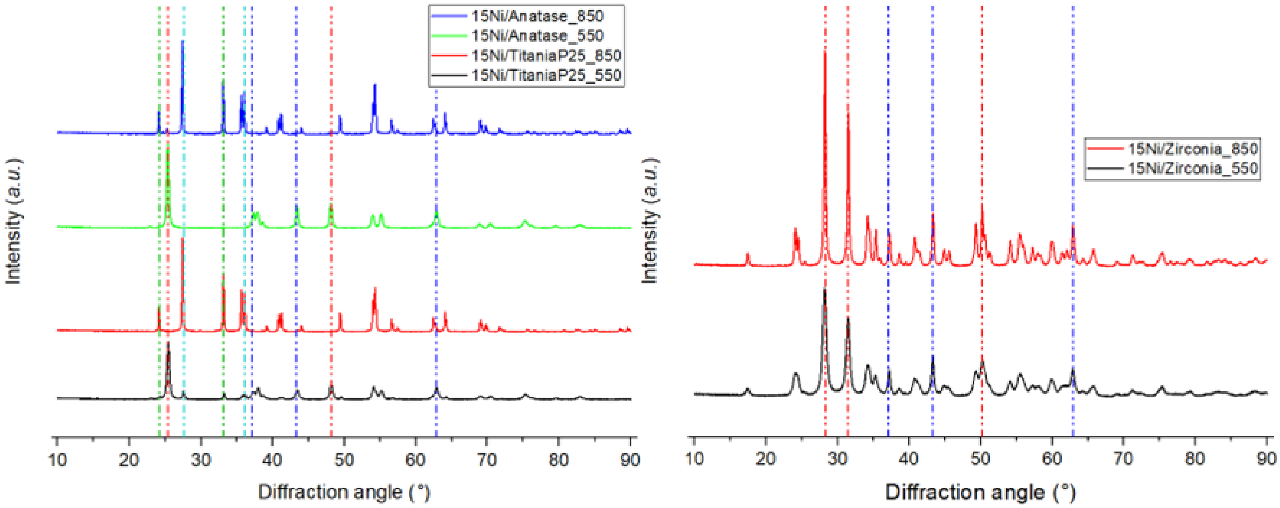

Fig. 4.7 Diffractograms of the calcined 15% nickel reducible supports-based catalysts. On the left, the vertical dotted lines show the position of the main peaks of anatase (red), rutile (light blue), nickel oxide (dark blue), and nickel titanate (green). On the right, they show the position of the main peaks of baddeleyite (red), and nickel oxide (blue).

Figure 4.7 depicts the XRD patterns for the remaining nickel catalyst. For the 15Ni/TitaniaP25_550 sample, the presence of anatase and rutile is observed, not showing a considerable change compared to the support. However, peaks at 37.2°, 43.3° and 62.9° are observed, which are characteristic of nickel oxide, and at 24.2° and 33.2°, caused by the limited formation of nickel titanate, NiTiO$_3$, by reaction with the support, not resulting in the total consumption of the oxide. The two peaks of the mixed oxide are characteristic of the (012) and (104) crystalline planes, respectively. By increasing the calcination temperature, a change in the phase of the support is showed for 15Ni/TitaniaP25_850, converting all the anatase into rutile, favoring the conversion of nickel oxide into titanate, leaving only some traces, while the majority of the metal is involved in the formation of the mixed oxide. By changing the initial crystalline phase, for 15Ni/Anatase_550, the phase transformation does not occur, remaining stable, and no reaction between the support and nickel oxide is detected, resulting in the absence of titanate. However, the situation changes drastically for 15Ni/Anatase_850. A strong conversion of titania into rutile is observed, even if not complete, and a total transformation of the oxide phase into nickel titanate occurs.[5,6,24,35,37,56,64,64,82,84,94,96,105,109]

Comparing the patterns of the four catalysts, it is noted that the peaks become sharper and narrower when the temperature increases, confirming the sintering hypothesis. Even more interesting is the phase transformation from anatase to rutile, which involves the reorganization of the crystalline structure and consequent collapse of the pores, contributing to the reduction of porosity and to the rearrangement of the distribution of metal, achieving lower dispersions.[5,6,63,64,84,101,103]

Both for 15Ni/Zirconia_550 and for 15Ni/Zirconia_850, the presence of nickel oxide is confirmed. However, the most interesting thing in this case is the change in the diffraction pattern for the monoclinic zirconia calcined at high temperatures. The peaks become narrower and more intense, due to sintering of the support. For neither of the two samples, a phase transformation is found.[2,4,5,28,36,48,52,65,66,101,103]

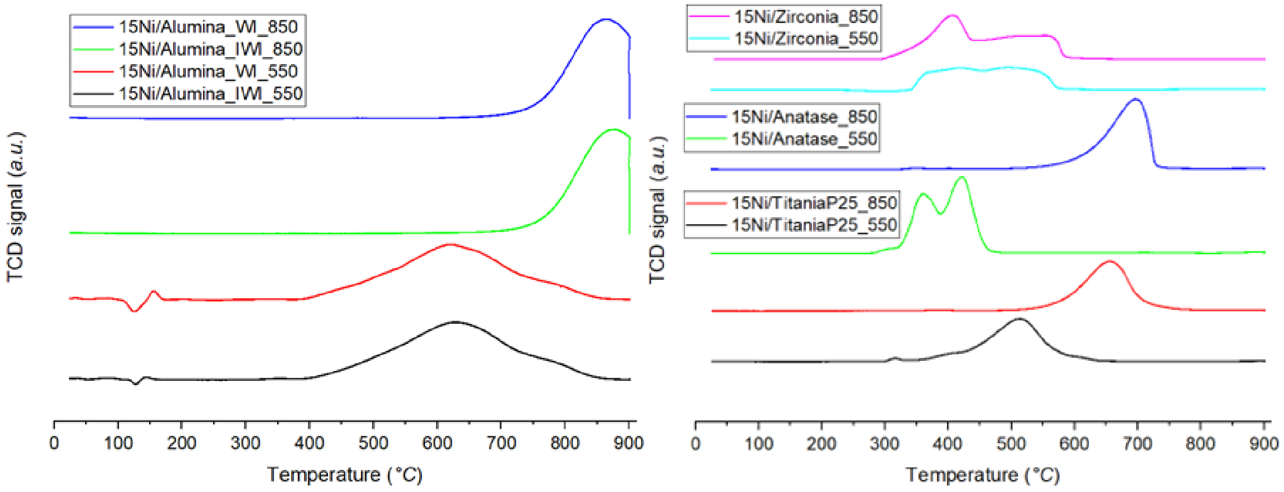

Fig. 4.8 Reduction profile of the 15% nickel catalysts.

Figure 4.8 shows the reduction profile of the nickel catalyst. Analyzing the Alumina-based catalysts, a strong difference caused by the calcination temperature is observed, while the synthesis method does not have any effect. At 550°C, a broad reduction peak with a maximum at about 630°C is observed. It is composed of three peaks, which are α-nickel, β-nickel, and γ-nickel. The peak at lower temperature is associated to α-nickel and derives from the reduction of oxide particles of considerable size, with a weak interaction with the support. The peak at intermediate temperature is related to β-nickel and derives from the reduction of oxide particles of smaller diameter, therefore, involved in a more intense interaction. Finally, the peak at higher temperature is assigned to γ-nickel, that corresponds to the reduction of the surface nickel aluminate, obtained by reaction with γ-alumina, in a very strong interaction with the support.[3,4,30,31,43,50,54,69,99,106] It is found that the main form assumed by the metal is the β phase, with a maximum at 630°C for 15Ni/Alumina_IWI_550 and 620°C for 15Ni/Alumina_WI_550.[3,31,69,105]

At higher temperatures, neither the α nor the β phase are anymore observed, only the γ remaining, with a reduction peak at approximately 875°C for 15Ni/Alumina_IWI_850 and 865°C for 15Ni/Alumina_WI_850. In this case, the aluminate is not superficial, like that obtained previously, more susceptible to reduction, but it is rather bulk aluminate, more stable, requiring higher reduction temperatures. This shows that an increase in calcination temperature allows for a better diffusion of nickel into the alumina lattice, until a massive phase is created.[3,4,26,50,54,69,99,105,106]

The peaks at less than 150°C are caused by the disturbance of the detector, due to the environmental humidity contained in the samples.

For 15Ni/TitaniaP25_550, a quite complex reduction profile is collected, caused by the presence of both anatase and rutile, doubling the number of interactions. In particular, a peak is observed at high temperatures, at around 515°C, due to the presence of a strong interaction of the nickel oxide with the support, but also by the occurrence of titanate, which is not particularly reducible. The reduction begins at around 300°C, suggesting that there are also a few nickel oxide particles with larger dimensions, which interact less with the support.[5,6,24,27,34,35,53,64,94,96,110] Increasing the temperature, for 15Ni/TitaniaP25_850, the peak shifts to 660°C, due to the massive formation of titanate, while no trace of the reduction at low temperature remains.[6]

A similar trend is confirmed for the Anatase-based catalysts, in fact there are two peaks for 15Ni/Anatase_550 at 360 and 420°C, respectively. They are caused by different interactions with the anatase, in particular, the one at higher temperatures is caused by nickel oxide particles on surface crystalline defects of the support, often lattice oxygen vacancies. The reduction begins at 285°C, with the conversion of oxide particles with weak interaction with the support.[5,6,24,27,34,35,53,64,94,96,110] For 15Ni/Anatase_850, only the titanate peak is observed at 695°C.[6] Comparing the two titania supports, it can be stated that the presence of rutile leads to a lower reducibility for calcination at 550°C, but it allows a better reducibility for calcination at 850°C, probably caused by a lower production of mixed oxide.[24,64,94,96]

Both 15Ni/Zirconia_550 and 15Ni/Zirconia_850 have a reduction profile centered in the same temperature range, between 300°C and 580°C, with a similar shape. The only difference is the higher intensity of the peak at low temperature, at 405° C, for the second sample. This is due to the reduction of larger nickel oxide particles, which are formed due to greater sintering and less dispersion caused by the decrease in surface area, the latter provoked by the collapse of the porosity of the support. The shape of the profiles shows a large number of interactions between nickel oxide and the support, in particular the interaction with lattice oxygen vacancies formed during the reduction process cannot be excluded.[2,4,5,28,36,48,61,66,98,105]

It is evident that the impregnation on a reducible support involves a strong reducibility of the metal, not only because of the reduced interaction with it, but also due to the redox properties, mediating the reduction of the oxide phase.[2,15,54,71,85]

The formation of metal particles on reducible supports allows a greater formation of oxygen vacancies, since nickel is able to provide reactive hydrogen via spill-over, facilitating surface reduction of the support.[2,7,24,36,37,48,52,87,103]

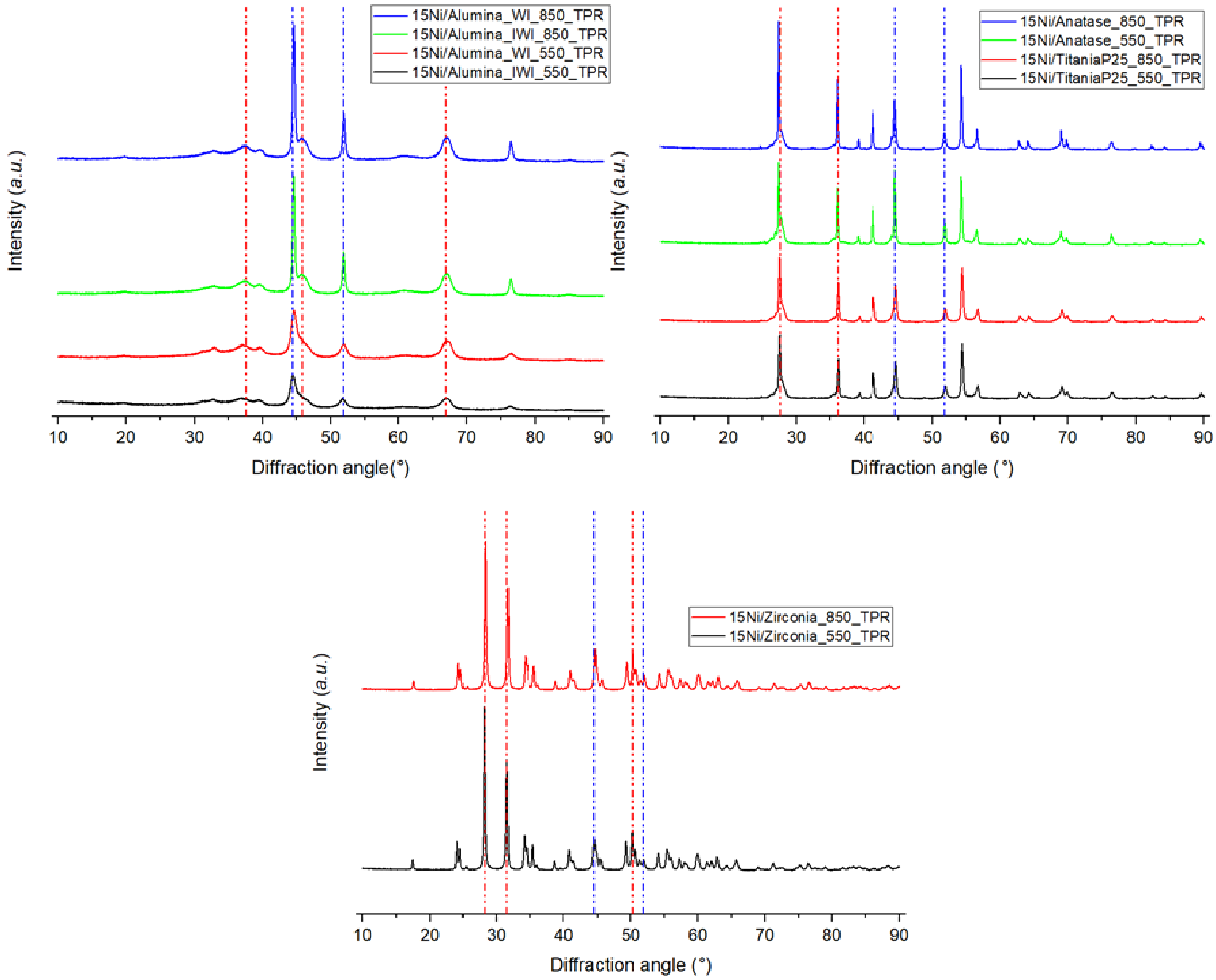

Fig. 4.9 Diffractograms of the reduced 15% nickel catalysts. The red vertical dotted lines show the position of the main peaks of γ-alumina, on the left, rutile, on the right, and baddeleyite, on the bottom. The blue ones show the main peaks of metallic nickel.

Figure 4.9 shows the XRD pattern of the nickel catalyst after the temperature-programmed reduction, while Table 4.3 reports the crystallite size of the nickel particles. From the XRD analysis, the complete conversion into metal for all the oxide phases containing nickel can be seen, with the peaks appearing at 44.5° and 51.9°, characteristic of the (111) and (200) crystalline planes.[3–5,27,29,35,43,48,50,64,66,67,84,94,96,106,109]

In the case of 15Ni/Alumina_IWI_850 and 15Ni/Alumina_WI_850 samples, metal particles of larger dimensions, compared to the corresponding calcined at 550°C, are formed due to the greater sintering during calcination. However, on the other reducible supports, the average particle diameters are very similar, regardless of the calcination temperature used. The only exception is 15Ni/Anatase_550, which has a big nickel particle size, higher than that found for 15Ni/Anatase_850.[3,10,26,29,48,50,97]

Alumina-based catalysts show a smaller nickel crystallite compared to other samples, due to the greater surface area, on which the metal is distributed, and the smaller pore size, which increases the dispersion.[3,15,24,28,31,33,52,64,70,74,78–81,85,94,100,101,104,106,107] A substantial and significant variation in the size of the metal particles is not observed in relation to the different synthesis procedure on Alumina.

Focusing on IWI synthesis, for 15Ni/Alumina_IWI_550 the metal particles are smaller than the average size of the pores, suggesting a substantial presence of nickel inside the pores. However, for 15Ni/Alumina_IWI_850, the opposite is observed, with particles averagely larger than the average diameter of the pores, therefore indicating that the metal resides mainly on the external surface of the particle or in the connections between pores, migrating due to the high temperature used.[71–73,79]

Regarding the effect on the supports, no variation in the XRD pattern is observed for γ-alumina, demonstrating once again its high thermal stability. The opposite happens for the titania supports, where only rutile was observed. Zirconia does not show any phase change, but the baddeleyite pattern for 15Ni/Zirconia_550 has very narrow and sharp peaks, due to the sintering of the crystallites of the support, phenomenon that did not occur during calcination due to the low temperature used.[64,66,84,101,109,111]

Table 4.3 Parameters collected by static chemisorption and XRD of the reduced 15% nickel catalysts.

Catalyst	**Dispersion (%)**	**Metallic area (m^2/g)**	**Crystallite size (nm)**	**XRD crystallite size (nm)**
15Ni/Alumina_IWI_550	5.75	5.74	17.6	9.0
15Ni/Alumina_WI_550	6.35	6.35	15.9	8.7
15Ni/Alumina_IWI_850	1.92	1.92	52.7	24.0
15Ni/Alumina_WI_850	2.78	2.77	36.4	24.2
15Ni/TitaniaP25_550	0.07	0.07	1518.1	24.3
15Ni/TitaniaP25_850	-	-	-	25.6
15Ni/Anatase_550	-	-	-	46.2
15Ni/Anatase_850	-	-	-	28.2
15Ni/Zirconia_550	1.80	1.80	56.1	43.9
15Ni/Zirconia_850	1.27	1.27	79.5	43.8

Table 4.3 reports the dispersion, the metal area and the crystallite size obtained by the static chemisorption of hydrogen for the nickel catalysts. Static hydrogen chemisorption partially confirms some trends obtained from the XRD analysis of the reduced samples, though differences can be found.

These differences can be attributed to the sensitivity of the techniques. XRD is a bulk sensitive technique, while chemisorption is a surface sensitive technique.

It is not possible to carry out successfully any chemisorption analysis on titania-based catalysts, since titanium is reduced to Ti^{3+} during the measurement. Ti^{3+} has a strong tendency to migrate on the surface of the nickel particles, isolating them from the external environment by formation of a reduced oxide coating, thus preventing the chemical adsorption of hydrogen on their surface. Figure 4.10 shows the formation of the coating after the reduction of the calcined catalyst. This phenomenon, called strong metal-support interaction (SMSI), is more intense at higher reduction temperatures, allowing a greater reduction of the support, and for anatase, leading to a better interaction with the nickel oxide. The measurement of 15Ni/TitaniaP25_550 is the only one with a positive result, although meaningless, due to the partial covering of the metal.[6,24,27,34,37,53,63,64,71,77,82,84,96,111–113]

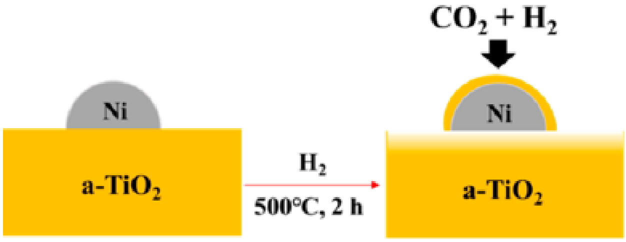

Fig. 4.10 Representation of the formation of the reduced oxide layer on nickel particles.[34]

An increase in the calcination temperature leads to a reduction in dispersion for both Alumina and Zirconia based samples. Although for the first support, the sintering of the nickel oxide particles could be the cause of the phenomenon, it was excluded from the XRD measurements on Zirconia-based catalysts. The further factor that explains this trend is the collapse of the pores of the support, leading to the isolation of nickel from the external environment, stuck in a closed pore, resulting in a lower quantity of adsorbate and a calculation that does not take into account the segregated metal portion.

The collapse of the pores also explains why the WI method allows for greater dispersion compared to the IWI one on Alumina, since the metal particles in the second synthesis are present only inside the pores, which are more susceptible to their collapse and to the segregation of nickel in closed pores. In contrast, for WI, the metal is also deposited on the external surface of the support, leading to less sequestered nickel. The difference is clear between 15Ni/Alumina_IWI_850 and 15Ni/Alumina_WI_850, since the higher calcination temperature causes a higher degree of the support sintering, while it is more contained for 15Ni/Alumina_IWI_550 and 15Ni/Alumina_WI_550, due to the lower collapse of the porosity. It should be noted that the high temperature causes minimal collapse of the pores for Alumina-based catalysts compared to those based on Zirconia, providing a less marked effect.

The greater dispersion of nickel is responsible for the higher surface area of 15Ni/Alumina_WI_550 and 15Ni/Alumina_WI_850, compared to the corresponding ones synthesized by the IWI method. In fact, smaller nickel particles lead to a lower probability of pore closure, maintaining a greater surface area.

4.3 *Cobalt catalysts*

After the nickel catalysts, the cobalt ones were characterized in order to investigate the change in properties caused by the use of a different metal. In the following, the results are presented.

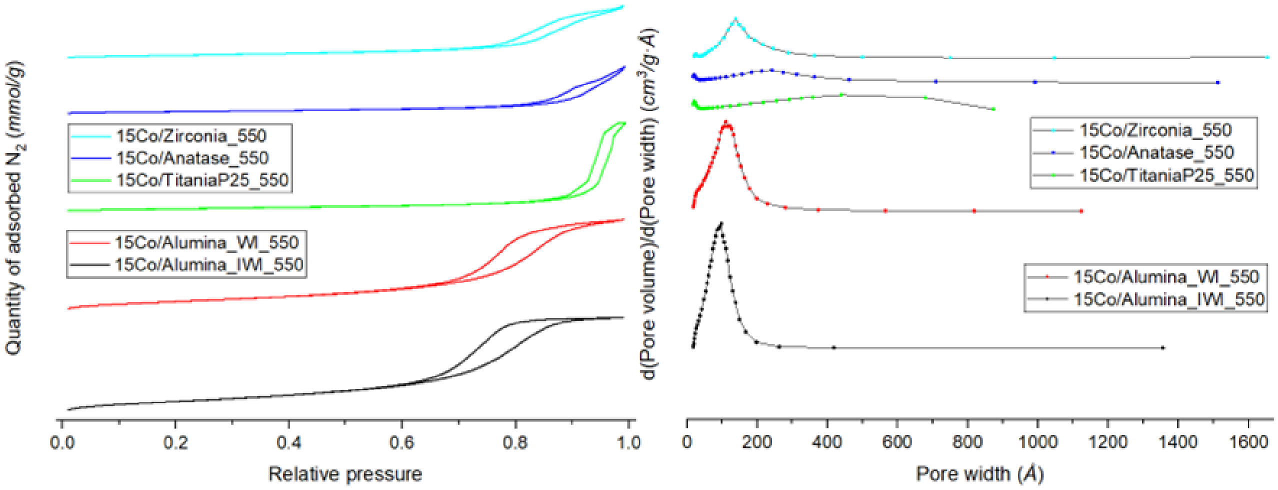

Fig. 4.11 Images of the isotherms, on the left, and of the pore size distribution, on the right, of the 15% cobalt catalysts.

Table 4.4 Textural properties and metal loading of the 15% cobalt catalysts.

Catalyst	**Surface area (m^2/g)**	**Pore volume (cm^3/g)**	**Average pore diameter (nm)**	**Metal loading (%)**
15Co/Alumina_IWI_550	155.7	0.36	9.2	16.9
15Co/Alumina_WI_550	131.3	0.34	10.4	18.1
15Co/TitaniaP25_550	39.0	0.32	31.6	13.0
15Co/Anatase_550	33.5	0.17	19.9	12.5
15Co/Zirconia_550	47.0	0.19	16.4	19.9

Figure 4.11 shows the adsorption isotherms and the pore size distribution curves for the cobalt catalysts, while Table 4.4 reports their textural properties. As before, type IV isotherms are observed, characteristic of mesoporous solids.[3–6,33,50,62,67,69,70,78,80,87,98–100,103]

The Alumina-based catalysts are still the one with highest porosity. Unlike the nickel case, the synthesis method affects the textural properties. In fact, better results are obtained for 15Co/Alumina_IWI_550 compared to 15Co/Alumina_WI_550, evidencing a greater area, similar to that of the support, and a lower average pore diameter. This suggests that during the WI there was greater obstruction of the pores, caused by the sintering of cobalt oxide particles on the outer surface of the alumina grains, which can move freely to form larger crystallites, due to the absence of mobility constraints such as pore walls.

The pore size distribution curves seem to confirm this hypothesis, noting a unimodal distribution for both samples. However, a certain fraction of micropores is observed for 15Co/Alumina_WI_550, accompanied by a shift of the maximum to higher values. This means that the impregnation did not distribute the metal homogeneously, but favored the deposition in the outer pores, leaving the inner ones unchanged.[76]

On Alumina, the decrease in the average pore diameter is prominent after impregnation, showing preferential narrowing rather than obstruction. The surface area decreases only for 15Co/Alumina_WI_550, while it remains unchanged for 15Co/Alumina_IWI_550 compared to the support due to the minimal obstruction of the pores.[62]

Comparing with the corresponding samples containing nickel, there is no significant difference with 15Ni/Alumina_WI_550, while there is a marked improvement in textural properties compared to 15Ni/Alumina_IWI_550, due to the partial closure of the pores for the latter.

The filling of the pores also explains the decrease in the surface area and pore volume, followed by an increase in their average diameter for catalysts obtained on reducible supports.[3,4,12,24,31–33,50,51,61,62,69,73,76,78–80,87,89,96,99–101,103,104,106,107] The only exceptions to this trend are 15Co/TitaniaP25_550 and 15Co/Anatase_550, evidencing the porous deposition of cobalt on the external surface of the support and the restriction of the pores, respectively.[71]

No variations are observed for the cobalt catalysts obtained from the reducible supports compared to the nickel counterpart., except for 15Co/Zirconia_550, that shows a greater surface area and a lower average pore diameter, showing a preferential restriction of pores rather than their obstruction.

As regards the distribution of the pore size, no drastic differences are observed compared to the impregnation with nickel at the same calcination temperature, showing an uneven distribution of the metal inside the pores, appearing a microporous fraction.[71]

The cobalt loadings are reported in Table 4.4. The values are close to the nominal one, pointing out a successful impregnation.

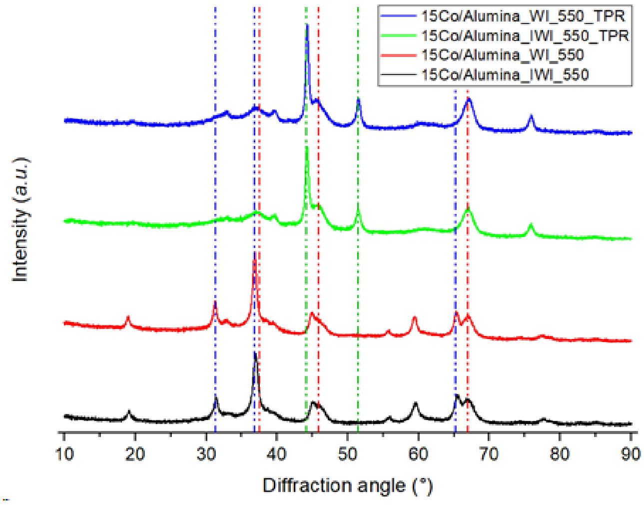

Fig. 4.12 Diffractograms of the calcined and reduced 15% cobalt Alumina-based catalysts. The vertical dotted lines show the position of the main peaks of γ-alumina (red), cobalt oxide (II,III) and cobalt aluminate (blue), and metallic cobalt (green).

Figure 4.12 shows the diffractograms of the Alumina-based cobalt catalysts. It is observed that the occurrence of γ-alumina, excluding any phase transformation of the support.[26,72,73,76,79,112]

Unfortunately, it is not possible to distinguish the presence of cobalt oxide (II,III), Co_3O_4, from the occurrence of cobalt aluminate, $CoAl_2O_4$, since both have the same spinel crystalline structure, with cell parameters very close to each other. This leads to the position of the peaks at the same diffraction angles, which are 31.3°, 36.9° and 65.2°, characteristic of the (220), (311) and (440) crystalline planes.[15,51,71–73,76,79,80,85,87,97,108,112,114]

The diffractometric patterns of 15Co/Alumina_IWI_550 and 15Co/Alumina_WI_550 are almost identical, therefore it is possible to state that the crystalline phases are independent by the synthesis method used in the preparation of the catalysts.

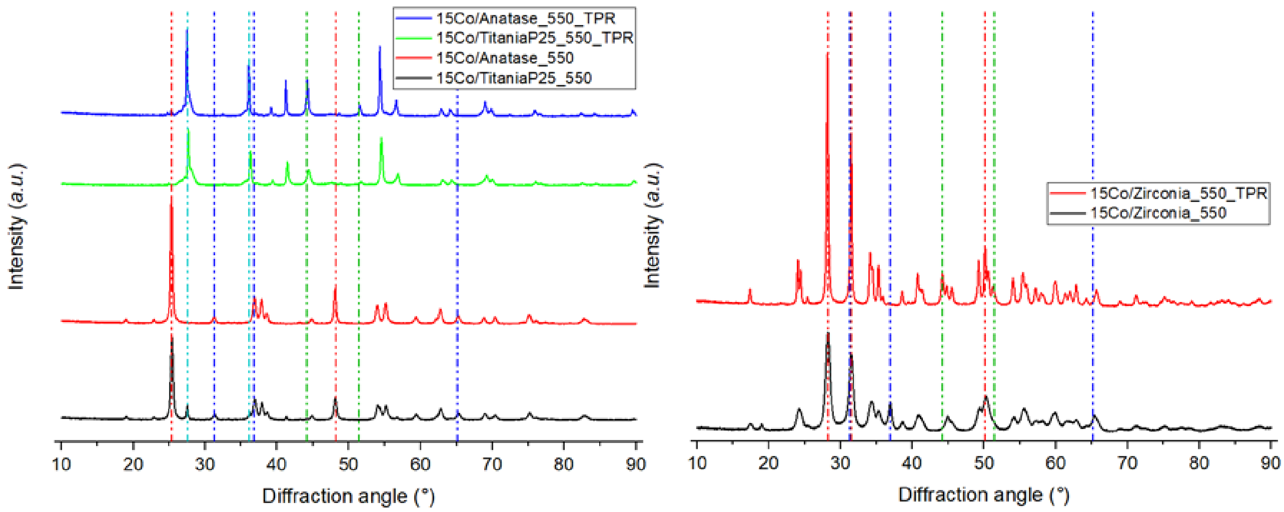

Fig. 4.13 Diffractograms of the calcined and reduced 15% cobalt Titania-based catalysts and Zirconia-based catalysts. On the left, the vertical dotted lines show the main peaks of anatase (red), rutile (light blue), cobalt oxide (II,III) (dark blue), and metallic cobalt (green). On the right, they show the main peaks of baddeleyite (red), and cobalt oxide (II,III) (blue), and metallic cobalt (green).

Figure 4.13 shows the diffractograms of the remaining cobalt catalysts. For titania supports, 15Co/TitaniaP25_550 shows the typical peaks for anatase and rutile, the latter with less intensity due to the lower content, and cobalt oxide(II,III). In particular, the proportion between the intensities of anatase and rutile peaks is similar to that of the support, evidencing no phase transformation at the calcination temperature used. Only the presence of anatase and cobalt oxide (II,III) is evident for 15Co/Anatase_550, showing no phase transformation of the support. Differently from nickel impregnation, cobalt titanate, $CoTiO_3$, was not formed.[63,74,82,94,112]

Lastly, 15Co/Zirconia_550 contains only cobalt oxide (II,III) and monoclinic zirconia. For the latter, the diffractogram has rather broad peaks, caused by small crystallites that are not sintered by the used temperature, pointing out the good thermal stability of Zirconia.[15,70,85,100,103,104]

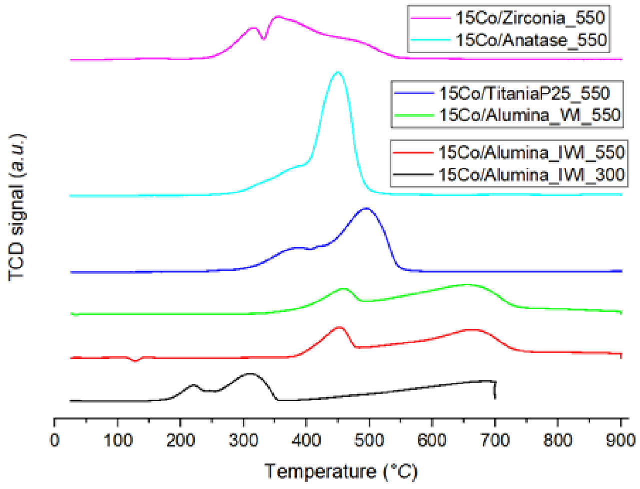

Fig. 4.14 Reduction profile of the 15% cobalt catalysts.

Figure 4.14 shows the reduction profile of the cobalt catalysts. The presence of a peak located at 220°C is evident for 15Co/Alumina_IWI_300, calcined at 300°C for 3h. It cannot be assigned to a cobalt oxide, but rather to nitrate used as precursor, confirming an incomplete calcination. Consequently, it was chosen 550°C, achieving complete calcination due to the absence of this peak on the other catalysts.[72,78,79,114]

The presence of two reduction peaks is evident for the Alumina-based catalyst, respectively at 455°C and 665°C for 15Co/Alumina_IWI_550, and 460°C and 655°C for 15Co/Alumina_WI_550, caused by the two-step reduction process of the cobalt oxide(II,III). The first peak is caused by the reduction to cobalt oxide(II), CoO, while the second from the latter to metallic cobalt. It occurs a weak but constant consumption of hydrogen at higher temperatures, due to small particles of cobalt oxide strongly interacting with the support and/or of cobalt aluminate, difficult to reduce, requiring very high temperatures.[15,72,73,76,78–80,85,87,89,97,107,112,114]

An intricate reduction profile is obtained for 15Co/TitaniaP25_550, caused by the presence of two different crystalline structures, doubling the possible interactions, and by the interactions with surface crystalline defects, such as oxygen vacancies. Two peaks are found at 385°C and 495°C, related to the two-step reduction of cobalt oxide, while the absence of cobalt titanate is confirmed by the lack of peaks at higher temperatures.[63,74,77,107,112]

A similar situation occurs for 15Co/Anatase_550, evidencing a peak at 450°C, caused by the reduction of cobalt oxide (II,III) with strong interactions with the support, and some overlapping peaks at lower temperatures, starting from 280°C due to the reduction of larger oxide particles.[63,74,77,107,112] In this case, the intensity of the peaks is greater and shifted to lower temperatures than for 15Co/TitaniaP25_550, concluding that the reducibility is higher. The same conclusion was previously drawn by comparing the corresponding nickel-containing catalysts.[115]

The catalyst with the highest reducibility is 15Co/Zirconia_550 due to the excellent redox properties of the support, showing the beginning of the reduction at lower temperatures, from 240°C up to 550°C. The reduction profile consists of a peak at 315°C, caused by the first reduction of quite large oxide particles, not interacting with crystalline defects, and a series of overlapping peaks with a maximum located at 355°C, due to the reduction of finer oxide particles, possibly on oxygen vacancies, taking into account the second step that leads to the formation of metal.[15,70,85,100,103,104]

Figures 4.12 and 4.13 show the diffractograms of the reduced cobalt catalysts, while Table 4.5 reports the crystallite size of the cobalt particles. The analysis shows the complete conversion of the oxide into metallic cobalt, point out by the appearance of the peaks at 44.2° and 51.5°, characteristic of the (111) and (200) crystalline planes.[63,76]

No phase transformation occurs for 15Co/Alumina_IWI_550, 15Co/Alumina_WI_550 and 15Co/Zirconia_550, maintaining γ-alumina and monoclinic zirconia, respectively. However, the narrowing of the peaks and the increase in their intensity is evident for the latter, caused by the sintering that increased the size of the crystallites of the support.

The transformation of titania from anatase to rutile phase is observed for 15Co/TitaniaP25_550 and 15Co/Anatase_550, caused by the high temperature. It is complete for the former, while some traces of anatase are kept for the latter.[63,64,71,84,111]

The average metal particles size is higher than the average pore diameter for 15Co/Alumina_IWI_550, concluding that there are many cobalt crystallites placed on the outer surface of the support or positioned between the junctions of two or more pores.[71–73,79] Furthermore, the average particle size is smaller for 15Co/Alumina_IWI_550 compared to 15Co/Alumina_WI_550, since the cobalt is also deposited on the external surface of the support particle for the latter, making easy the migration and agglomeration of the crystallites. This confirms the previous hypothesis made to explain the smaller surface area obtained by the WI method.

The size of the metal particles is clearly inversely proportional to the surface area of the material and directly proportional to their average pore diameter.[3,15,24,28,31,33,64,70,74,76,78–81,85,94,100,104,106,107] The only exception is 15Co/Zirconia_550, which shows a slightly bigger area and a smaller pore size compared to the two titania-based catalysts. However, a lower interaction between metal and support occurs, deduced from the lower reduction temperatures for 15Co/Zirconia_550, allowing an easier aggregation of the cobalt particles.[10,27]

Comparing with the nickel counterparts, 15Co/Alumina_IWI_550 and 15Co/Alumina_WI_550 show larger metal particles, pointing out a greater tendency to sinter for cobalt. On the contrary, 15Co/Anatase_550 shows smaller dimensions.

Table 4.5 Parameters collected by static chemisorption and XRD of the reduced 15% cobalt catalysts.

Catalyst	**Dispersion (%)**	**Metallic area (m^2/g)**	**Crystallite size (nm)**	**XRD crystallite size (nm)**
15Co/Alumina_IWI_550	2.76	2.75	36.7	14.4
15Co/Alumina_WI_550	2.74	2.74	37.0	15.1
15Co/TitaniaP25_550	0.17	0.17	578.9	24.1
15Co/Anatase_550	-	-	-	33.2
15Co/Zirconia_550	1.42	1.42	71.1	41.4

Table 4.5 reports the dispersion, the metal area and the crystallite size obtained by the static chemisorption of hydrogen for the cobalt catalysts. The static chemisorption of hydrogen confirms the same trends seen from the diffractometry of the reduced catalysts, obtaining a greater dispersion on Alumina. However, even in this case, it is not possible to carry out measurements or have meaningful measurements for the titania-based catalysts due to the strong metal-support interaction. Such phenomenon involves the coating of cobalt particles with a few atomic layers of reduced support, isolating the metal from the external environment.[6,24,27,34,37,53,63,64,71,77,82,84,96,111,112,116]

4.4 *10 wt.% metal loading catalysts*

The characterization of the lower metal loading catalysts is shown below, reporting the repercussions on the final properties.

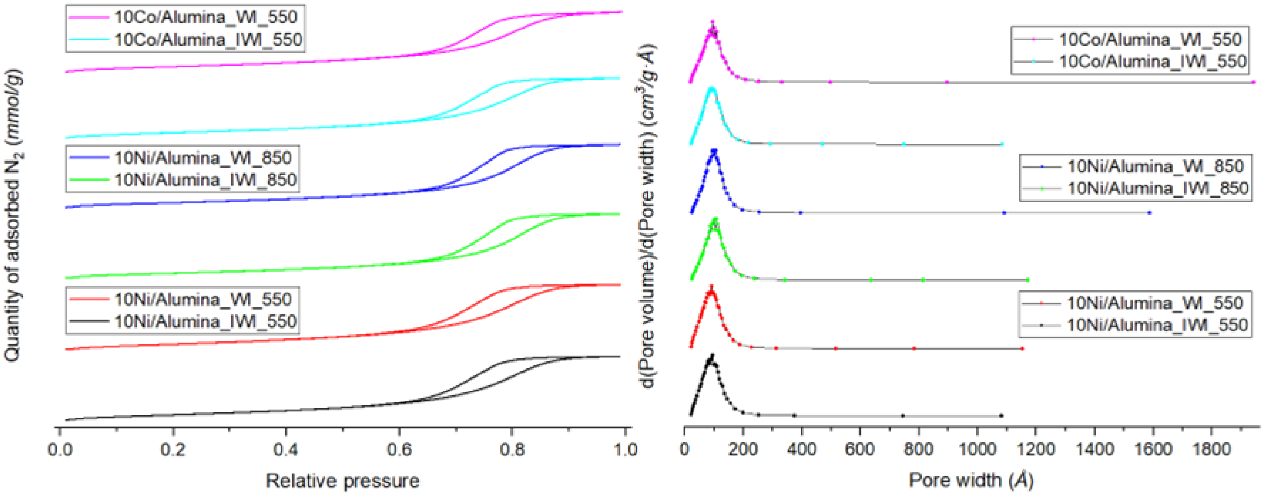

Fig. 4.15 Images of the isotherms, on the left, and of the pore size distribution, on the right, of the 10% metal catalysts.

Table 4.6 Textural properties and metal loading of the 10% metal catalysts.

Catalyst	Surface area (m^2/g)	Pore volume (cm^3/g)	Average pore diameter (nm)	Metal loading (%)
10Ni/Alumina_IWI_550	178.4	0.43	9.5	10.2
10Ni/Alumina_WI_550	185.6	0.43	9.4	8.1
10Ni/Alumina_IWI_850	160.5	0.42	10.5	10.0
10Ni/Alumina_WI_850	157.6	0.42	10.6	8.3
10Co/Alumina_IWI_550	163.7	0.40	9.7	10.2
10Co/Alumina_WI_550	165.9	0.40	9.6	9.8

Figure 4.15 shows the adsorption isotherms and the pore size distribution curves for the lower metal loading catalysts, while Table 4.6 reports their textural properties. The hysteresis caused by capillary condensation point out the occurrence of type IV adsorption isotherms, typical of mesoporous solids, exactly as found for the previous Alumina-based catalysts.[3–6,33,50,62,67,69,78,80,87,98–100]

The impregnation with a smaller quantity of precursor leads to an obvious decrease in the pore volume and an unexpected increase in the surface area, contrary to previously. This cannot be explained with a porous deposition of the precursor on the outer surface of the support, since the pore distributions are all unimodal, pointing out a uniform impregnation of the metal in all pores.[76] The cause is the formation of very small oxide particles, which act as protrusions attached to the pore wall, allowing the shrinkage and create a more curvilinear and sinuous path, favoring the formation of further surface area. The tiny size of the crystallites avoids clogging of the pore, which is minimal.[50,62,98]

The increase in calcination temperature leads to a decrease of the surface area and an increase of the average pore diameter. This is caused by a more intense sintering of the nickel oxide particles, agglomerating in larger crystallites and causing greater clogging of the finer pores, eliminating or reducing this population from the distribution.[3,5,10,33,48,69,101]

The surface area is smaller on catalysts obtained by impregnating with cobalt instead of nickel, concluding that the tendency to agglomerate is greater for the first metal, producing larger particles with less dispersion.

Analyzing the difference between the synthesis techniques, WI method allows for larger surface areas compared to IWI one at low calcination temperature, 550°C, while for higher temperatures, 850°C, the opposite occurs. The cause is the larger available area on which to disperse the metal for the WI synthesis, allowing the creation of smaller particles, less able to clog the pores. However, providing more thermal energy, the particles on the outer surface of Alumina migrate more easily, having no restriction to mobility, creating crystallites large enough to block the pore entrances, decreasing the surface area available for physisorption. The difference in area is more evident for nickel compared to cobalt, due to the previously mentioned greater mobility of the latter metal.[33]

Comparing the catalysts with the higher loading counterparts, a higher surface area and pore volume are observed, while it is evident a lower average diameter, caused by the less filling of the support.[101] The only catalyst with no drastic difference is 15Co/Alumina_IWI_550, due to its already excellent dispersion of the metal.

Table 4.6 reports the metal loadings of the catalyst, obtained by X-ray fluorescence. It is confirmed that the metal content is close to the nominal target.

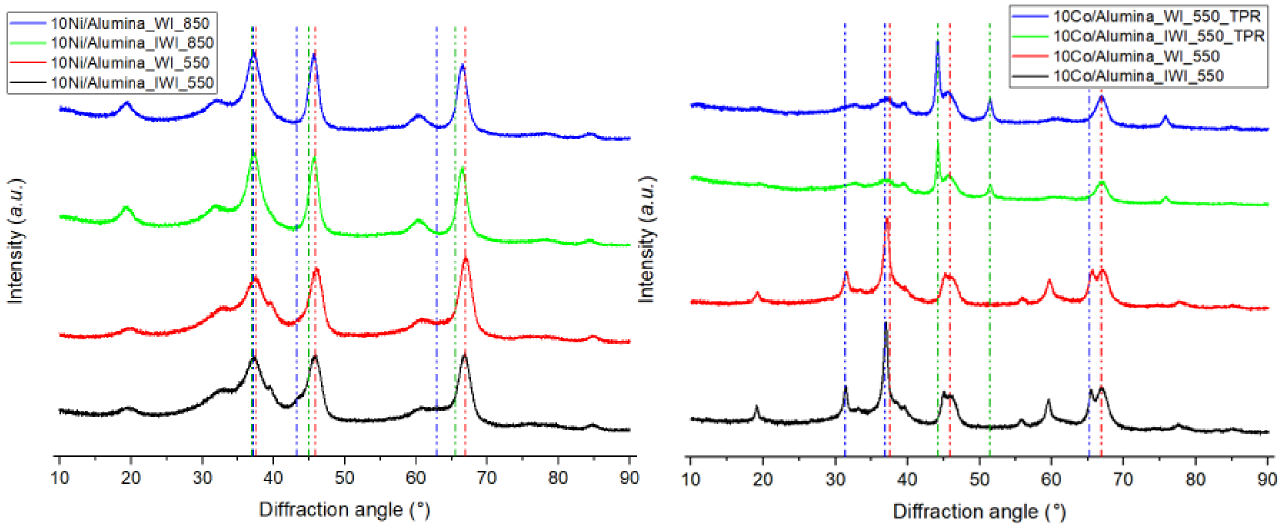

Fig. 4.16 Diffractograms of the calcined 10% nickel catalysts, and calcined and reduced 10% cobalt catalysts. On the left, the vertical dotted lines show the position of the main peaks of γ-alumina (red), nickel oxide (blue), and nickel aluminate (green). On the right, they show the main peaks of γ-alumina (red), cobalt oxide (II,III) and cobalt aluminate (blue), and metallic cobalt (green).

Figure 4.16 shows the diffractograms of the lower metal loading catalysts. No phase transformation is observed, pointing out only the occurrence of γ-alumina, due to the excellent thermal stability.[3,26,50,72,79,105]

Nickel oxide is observed for 10Ni/Alumina_IWI_550 and 10Ni/Alumina_WI_550. The complete conversion of the oxide into nickel aluminate occurs for 10Ni/Alumina_IWI_850 and 10Ni/Alumina_WI_850 due to the higher calcination temperature, causing a reaction with the support.[3,4,10,29,31,37,47,48,50,67,69,99,105,106,108]

It is impossible to discriminate between cobalt oxide (II,III) and cobalt aluminate occurs for 10Co/Alumina_IWI_550 and 10Co/Alumina_WI_550, due to the same position and intensity of the peaks.[51,71–73,76,79,80,85,87,97,108,112]

The decrease of the intensity of the peaks is evident for all samples due to the lower metal loading, in particular a clear difference is observed for 10Ni/Alumina_IWI_550 and 10Ni/Alumina_WI_550, making it difficult to determine the peaks.[99] This is also caused by the greater dispersion of the metal oxide, provoking a broadening of the peaks and a reduction in their height. This effect is not so evident for the other catalysts due to the greater tendency towards aggregation, caused by the increase in calcination temperature or the greater mobility of the cobalt.

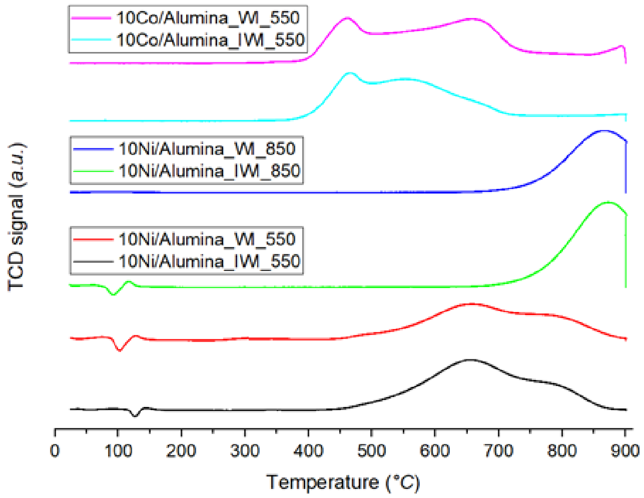

Fig. 4.17 Reduction profile of the 10% metal catalysts.

Figure 4.17 shows the reduction profiles of the lower metal loading catalysts. All three oxide phases related to nickel, α, β and γ, are observed for 10Ni/Alumina_IWI_550 and 10Ni/Alumina_WI_550. However, their relative contents are different compared to the higher nickel loading catalysts. In particular, an increase in the presence of γ nickel is observed, essentially consisting of surface aluminate. This is caused by the greater dispersion of the nickel oxide particles, which have a greater interaction with the support due to the smaller size, making the oxide less reducible. On the other hand, the stronger interaction also allows an easier formation of the aluminate, leading to its greater formation, especially for 10Ni/Alumina_WI_550. The lower reducibility is confirmed by looking at the maxima, 655°C for 10Ni/Alumina_IWI_550 and 660°C for 10Ni/Alumina_WI_550, evidencing a shift towards higher temperatures compared to higher metal contents.[3,4,10,43,50,54,69,99,105,107]

The formation of bulk nickel aluminate is evident for 10Ni/Alumina_IWI_850 and 10Ni/Alumina_WI_850, with maxima centered at 875°C and 865°C, respectively, This values are exactly the same for the counterparts with higher loadings.[3,4,26,50,54,69,99,105]

The two peaks caused by the two-step reduction process are observed for 10Co/Alumina_IWI_550 and 10Co/Alumina_WI_550, forming cobalt oxide (II) and subsequently the metallic phase. The shape of the reduction profile does not differ significantly from higher loadings, except for an increase of the reducibility for 10Co/Alumina_IWI_550, with a shift of the maximum of the second peak to 550°C from 665°C, and for a higher hydrogen consumption at higher temperatures, over 840°C, for 10Co/Alumina_WI_550, due to the presence of cobalt aluminate. The lower reducibility of 10Co/Alumina_WI_550 compared to higher loading catalysts and to 10Co/Alumina_IWI_550 is caused by the better dispersion of the metal, arranging it also on the outer surface of the Alumina grain, leading to smaller particles with stronger interaction with the support, and by the the formation of a greater quantity of mixed oxide.[72,73,76,78–80,85,87,89,97,107,114]

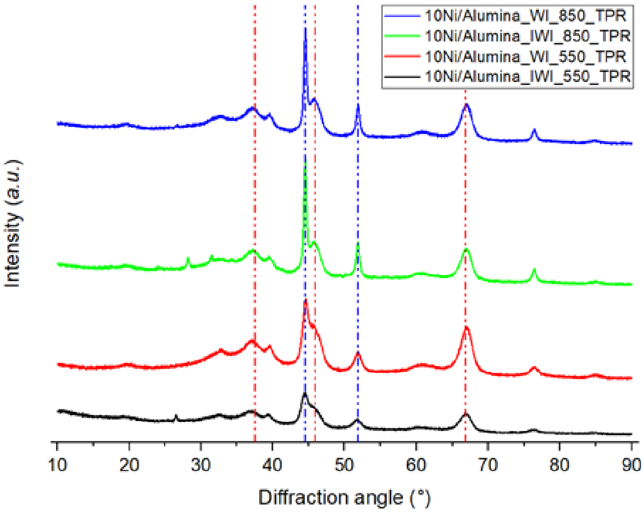

Fig. 4.18 Diffractograms of the reduced 10% nickel catalysts. The vertical dotted lines show the position of the main peaks of γ-alumina (red), and metallic nickel (blue).

Figures 4.16 and 4.18 show the diffractograms of the lower metal loading catalysts after the temperature programmed-reduction, while Table 4.7 reports the crystallite size of the metal particles. The complete reduction to metal is verified for the various catalysts, observing the appearance of the characteristic peaks related to nickel, 44.5° and 51.9°, and to cobalt, 44.2° and 51.5°. No variation in the γ-alumina patterns occur for the samples, pointing out the support stability even for lower metal loadings.[3,4,27,29,35,43,48,50,64,67,76,84,94,106,109]

After the reduction, the metal particle size for 10Ni/Alumina_WI_550 is larger compared to 10Ni/Alumina_IWI_550, even if the two values are very close to each other, so the difference is considered negligible. An opposite trend is observed for 10Ni/Alumina_IWI_850 and 10Ni/Alumina_WI_850, caused by the greater aggregation during calcination for the former catalyst, due to the smaller available area to distribute the nickel. However, the difference is so small that no conclusions can be drawn.[3,10,26,29,48,50,97]

The difference of the particle size is also negligible for 10Co/Alumina_IWI_550 and 10Co/Alumina_WI_550, although the values follow the trend previously forecasted to explain the greater reducibility for the IWI synthesis.

The average size of the nickel particles is smaller for a lower loading, while it is roughly the same for cobalt, evidencing the greater mobility of this metal.[3,30,73,77,107]

The size of the crystallites is smaller than the average pore diameter for 10Ni/Alumina_IWI_550, pointing out a mainly positioning of the metal inside the pores, while the same conclusion cannot be reached for the other catalysts obtained by the IWI synthesis, with the metal also on the outer surface and in the connections between pores.[71–73,79]

Table 4.7 Parameters collected by static chemisorption and XRD of the reduced 10% metal catalysts.

Catalyst	**Dispersion (%)**	**Metallic area (m^2/g)**	**Crystallite size (nm)**	**XRD crystallite size (nm)**
10Ni/Alumina_IWI_550	4.33	4.33	23.4	8.0
10Ni/Alumina_WI_550	2.89	2.89	35.0	8.8
10Ni/Alumina_IWI_850	2.37	2.37	42.6	17.1
10Ni/Alumina_WI_850	1.75	1.75	57.8	16.5
10Co/Alumina_IWI_550	1.45	1.45	69.7	15.1
10Co/Alumina_WI_550	1.56	1.56	64.9	14.5

Table 4.7 reports the dispersion, the metal area and the crystallite size obtained by the static chemisorption of hydrogen for the lower metal loading catalysts. The same results are not returned by chemisorption, in fact in this case a lower dispersion of the metal is observed compared to that obtained for the higher loading counterparts. This is caused by the lack of reduction of the mixed oxide, which is formed in greater quantities due to better interaction with the support, resulting in less exposed metallic area. The only exceptions are 10Ni/Alumina_IWI_850 and 10Ni/Alumina_WI_850, which show complete participation of nickel in the formation of the aluminate, exactly like for higher metal content.[87,109]

In particular, 10Ni/Alumina_WI_550 shows a lower metallic area due to the greater quantity of aluminate formed compared to 10Ni/Alumina_IWI_550, as evidenced by the TPR analysis. The same trend cannot be explained with the same phenomenon for 10Ni/Alumina_IWI_850 and 10Ni/Alumina_WI_850, since the quantities of mixed oxide formed are the same. The cause is instead caused by the greater aggregation of the particles on the external surface of the support, confirming the accidental variation observed in the diffractometric measurement.

A very small difference in the dimensions of the is verified for 10Co/Alumina_IWI_550 and 10Co/Alumina_WI_550. A much larger crystallite size is observed for the cobalt catalysts compared to the nickel analogues, due to the greater sintering of this metal.

4.5 *Addition of cerium oxide as catalyst promoter*

It is concluded from the previous characterization that Alumina-based catalysts are the most porous, but the support is not able of any redox property. In the following, it is reported the characterization of Alumina-based catalysts promoted with cerium, providing a reducible oxide and determining the effect on physico-chemical properties.

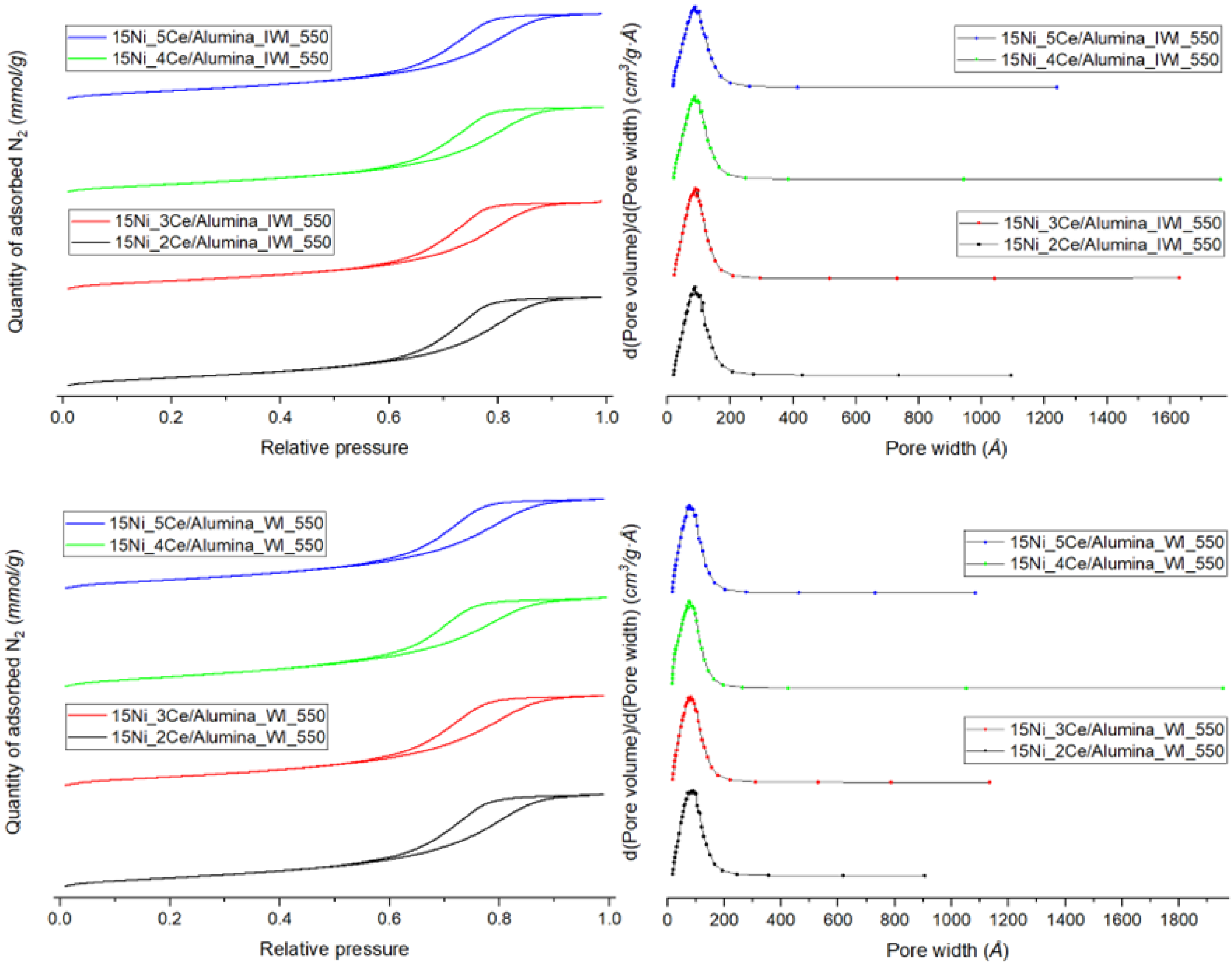

Fig. 4.19 Images of the isotherms, on the left, and the pore size distribution, on the right, of the 15% nickel promoted catalysts, calcined at 550°C.

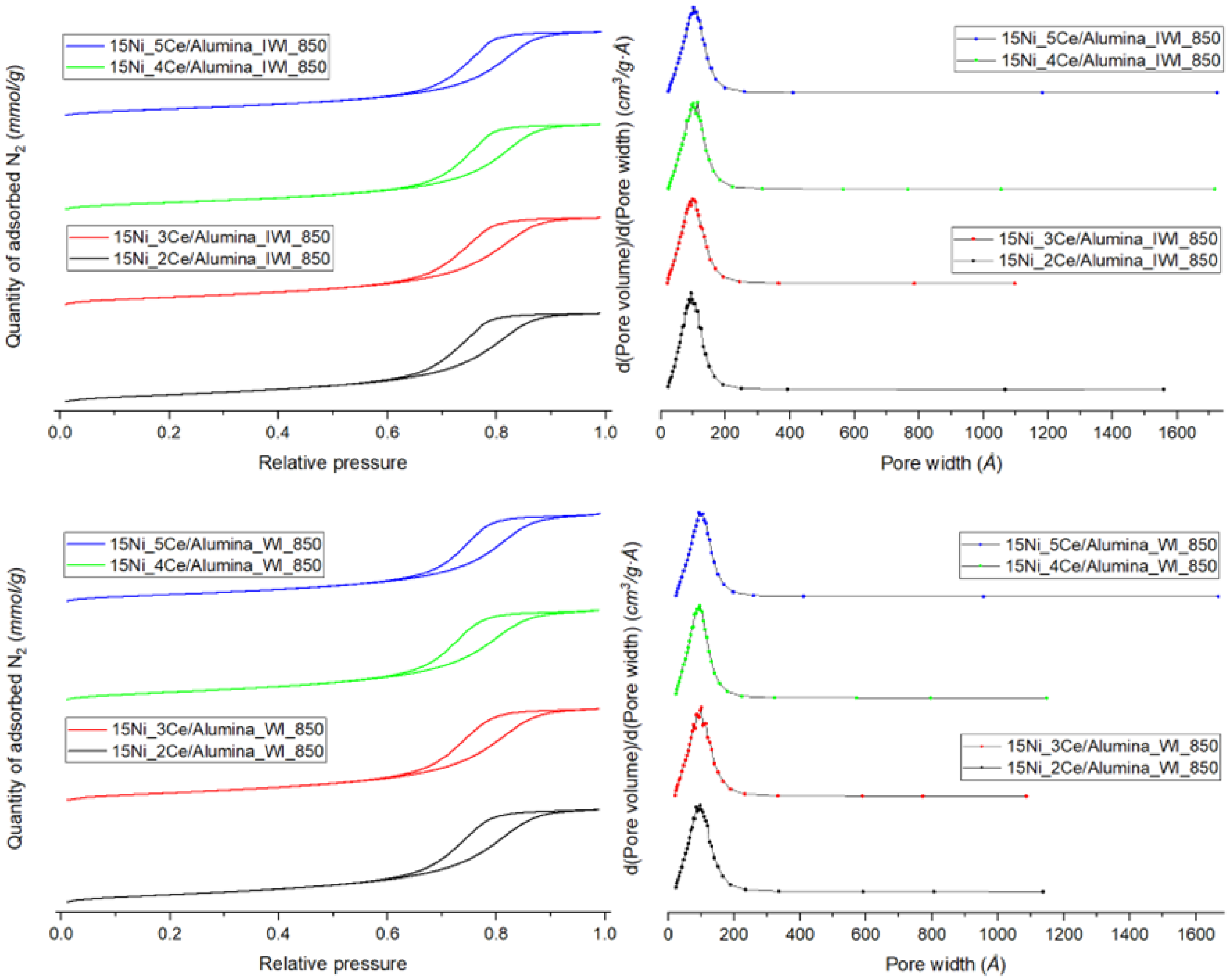

Fig. 4.20 Images of the isotherms, on the left, and the pore size distribution, on the right, of the 15% nickel promoted catalysts, calcined at 850°C.

Table 4.8 Textural properties and metal loading of the 15% nickel promoted catalysts.

Catalyst	**Surface area (m^2/g)**	**Pore volume (cm^3/g)**	**Average pore diameter (nm)**	**Metal loading (%)**
15Ni_2Ce/Alumina_IWI_550	157.5	0.36	9.1	14.4
15Ni_2Ce/Alumina_WI_550	159.3	0.35	8.8	13.4
15Ni_3Ce/Alumina_IWI_550	155.7	0.36	9.2	13.8
15Ni_3Ce/Alumina_WI_550	161.1	0.34	8.6	14.2
15Ni_4Ce/Alumina_IWI_550	152.4	0.34	9.0	13.4
15Ni_4Ce/Alumina_WI_550	176.1	0.34	7.8	14.2
15Ni_5Ce/Alumina_IWI_550	154.3	0.34	8.9	13.5
15Ni_5Ce/Alumina_WI_550	163.8	0.34	8.4	13.4
15Ni_2Ce/Alumina_IWI_850	139.0	0.36	10.2	14.3
15Ni_2Ce/Alumina_WI_850	140.8	0.35	10.0	13.3
15Ni_3Ce/Alumina_IWI_850	137.3	0.35	10.1	13.7
15Ni_3Ce/Alumina_WI_850	139.1	0.35	10.0	14.0
15Ni_4Ce/Alumina_IWI_850	127.0	0.34	10.7	13.2
15Ni_4Ce/Alumina_WI_850	139.7	0.34	9.7	14.2
15Ni_5Ce/Alumina_IWI_850	126.2	0.33	10.6	13.3
15Ni_5Ce/Alumina_WI_850	125.9	0.33	10.5	13.0

Figures 4.19 and 4.20 shows the adsorption isotherms and the pore size distribution curves for the promoted nickel catalysts, while Table 4.8 reports their textural properties. All the isotherms are of IV type, evidencing the occurrence of a mesoporous solid with high porosity, able to adsorb a lot of nitrogen.[3–6,33,50,62,67,69,78,80,87,98–100] The shapes of the isotherms are very similar for all catalysts, confirming that the differences must be minimal. The pore size distribution curves are all unimodal, resulting in a uniform impregnation in the pores of the support. The maximum is shifted to larger diameters for higher calcination temperatures, pointing out a greater sintering of the nickel oxide.[5,76]

There is a reduction in the pore volume as the quantity of cerium increases, due to the greater filling of the pore. Dividing the catalysts into the two calcination temperatures, the average pore diameters are almost identical among the different samples. A slightly smaller diameter is observed for calcined samples at 550°C by adopting the WI synthesis, due to the deposition of the metal on the outer surface of the support, causing less closure of the pores.

It is observed that the introduction of cerium allows to decrease the average pore size compared to the support and to the unpromoted counterparts, showing that the cerium permits a better dispersion of the nickel, forming smaller particles, which are able to shrink the pores but less to clog them.[31,60,61,68]

Higher surface areas are reported for lower calcination temperatures, limiting the agglomeration of the metal oxide particles, and for WI synthesis, since a greater area of the support is provided to disperse the metal, taking advantage of the external surface.[3,48,69]

A greater area is observed for the promoted catalysts calcined at 550°C compared to the support and the unpromoted counterparts. This is caused by the small oxide crystallites that are attached to the pore walls, making them more curvilinear and sinuous, allowing the creation of additional surface area.[31]

A decrease of the area is observed as the cerium loading increases, due to the formation of larger oxide particles which lead to greater obstruction of the pores. The only exception is the series of catalysts calcined at 550°C and synthesized by the WI method, for which an increase is noted up to 4% of cerium, followed by a subsequent decrease. This is caused by a greater initial narrowing of the pores due to the formation of oxide protrusions inside them, followed by their closure due to the increase in the quantity of precursor used.[31,33,60,62,68,87]

Table 4.8 reports the nickel loading of the promoted catalysts. The values are very close to the nominal one. Unfortunately, it is not possible to determine the cerium loading using the instrument adopted.

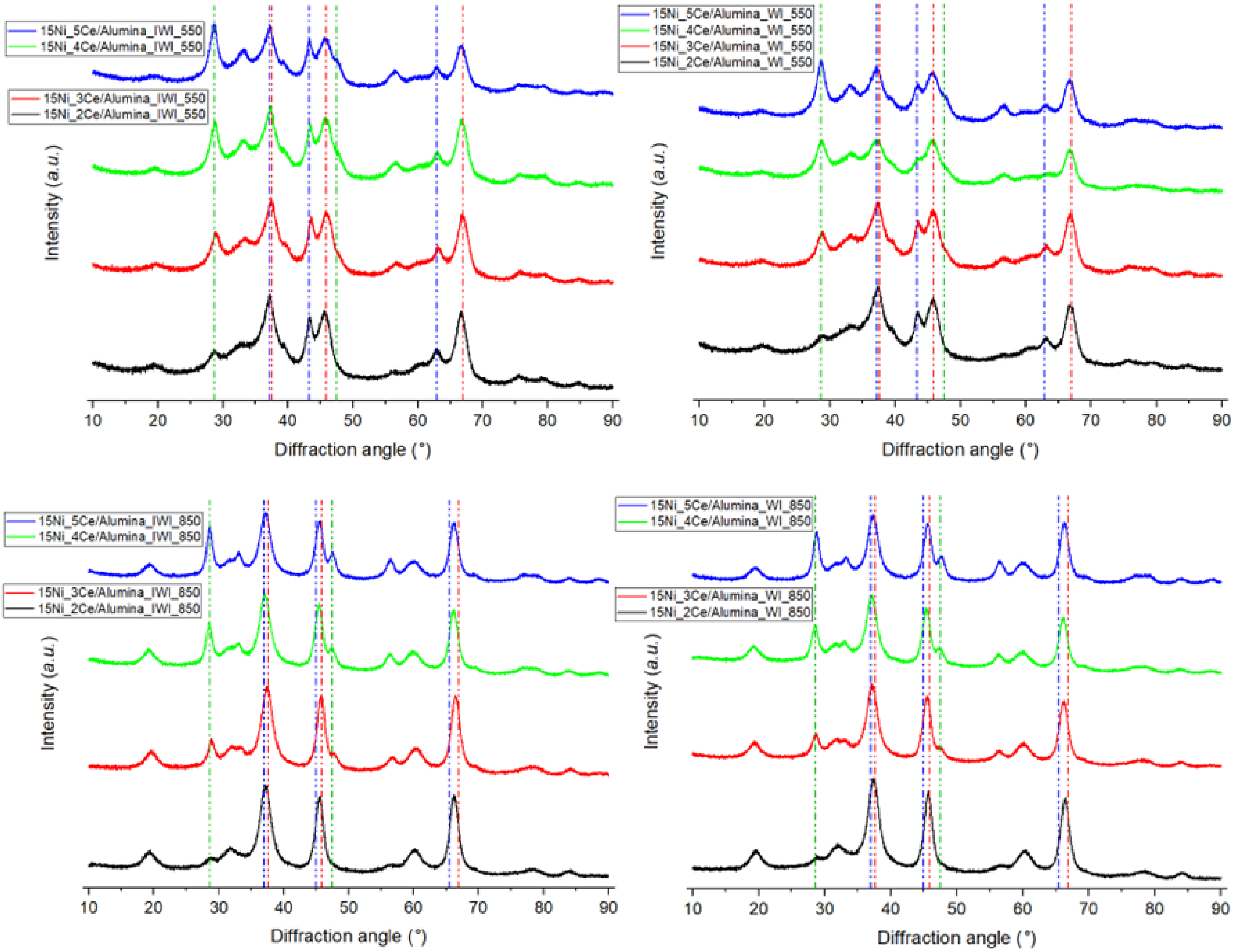

Fig. 4.21 Diffractograms of the calcined 15% nickel promoted catalysts. The vertical dotted lines show the position of the main peaks of γ-alumina (red), and cerianite (green). On the top, the blue ones show the main peaks of nickel oxide, while on the bottom, of nickel aluminate.

Figure 4.21 shows the diffractograms of the cerium promoted catalysts. The peaks related to γ-alumina are observed, confirming also the occurrence of the cerianite, at 28.6° and 47.5°. The peaks of ceria become gradually more intense as the cerium loading increases, being barely perceptible, for a 2% content, to clearly visible, for a 5%.[60,87]

The formation of nickel oxide, called also bunsenite, is observed for the catalysts calcined at 550°C, appearing the peaks at 37.2°, 43.3° and 62.9°. No differences are found in the patterns based on the synthesis method or the cerium addition, except for the occurrence of the peaks of the latter.[3,4,29,47,48,67,69,99]

Nickel aluminate is formed by complete conversion of the oxide for the catalysts calcined at 850°C, appearing the peaks at 37.0°, 45.0° and 65.5°. No effects are observed based on the synthesis method or the cerium introduction, other than the presence of peaks related to this.[2–4,26,37,60,67,69,99,108]

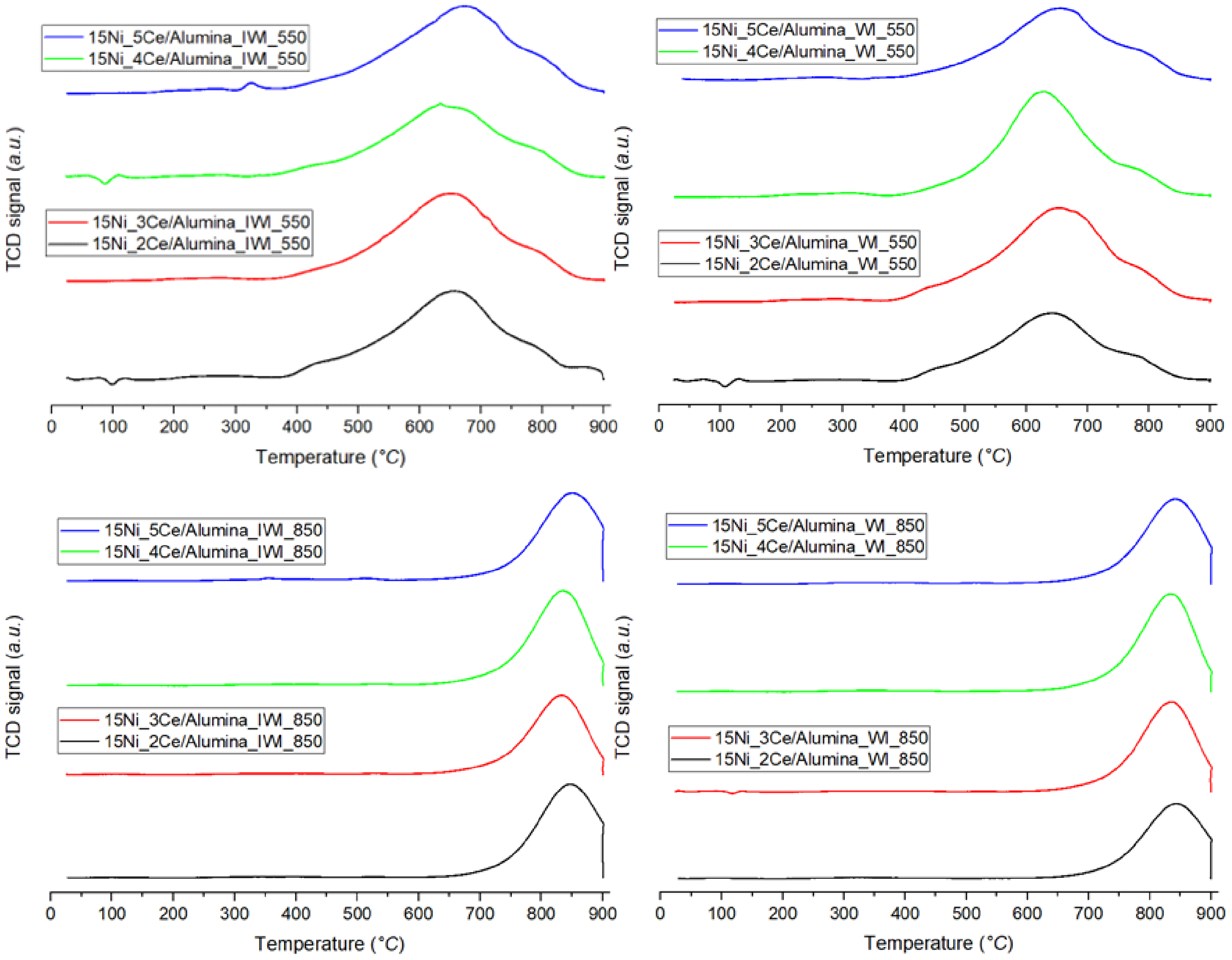

Fig. 4.22 Reduction profile of the 15% nickel promoted catalysts.

Figure 4.22 shows the reduction profile of the promoted catalysts. The three nickel phases appear for the samples calcined at 550°C, exactly as for the corresponding unpromoted samples, roughly in the same proportions. The maxima of the reduction profile are located between 650°C and 670°C for the series obtained through IWI synthesis, and between 630°C and 650°C for the one for the WI one. In particular, 15Ni_4Ce/Alumina_WI_550 stands out for its best reducibility, with a peak centered at 630°C. These values are slightly higher compared to the maxima of the unpromoted catalysts, even if the differences are negligible.[3,62,69]

A small reduction peak at 350°C is shown for 15Ni_5Ce/Alumina_IWI_550, caused by the occurrence of unsupported nickel oxide, not interacting with the support and easier to reduce.[30,62] Its cause is the higher loading of cerium, filling more the pores, and the deposition only on the inner surface, accumulating too much precursor to allow an optimal contact with the support.

A lower reducibility is observed for the catalysts calcined at 850°C, caused by the formation of the bulk aluminate, similarly to the unpromoted counterparts. There are some variations in the position of the maxima, between 830°C and 850°C for IWI synthesis, and between 835°C and 845°C for the

WI one. The values are slightly lower in absence of promoter, but even in this case the differences are negligible.[3,26,62,69]

The promoter should hinderance the formation of the aluminate, keeping a higher amount of nickel oxide, and modifying the electronic distribution of the oxide, incrementing the reducibility. However, it seems that cerium is not present in sufficient quantity to allow an increase in reducibility, preventing the formation of the mixed oxide.[10,11,31,56,60,62,68,87]

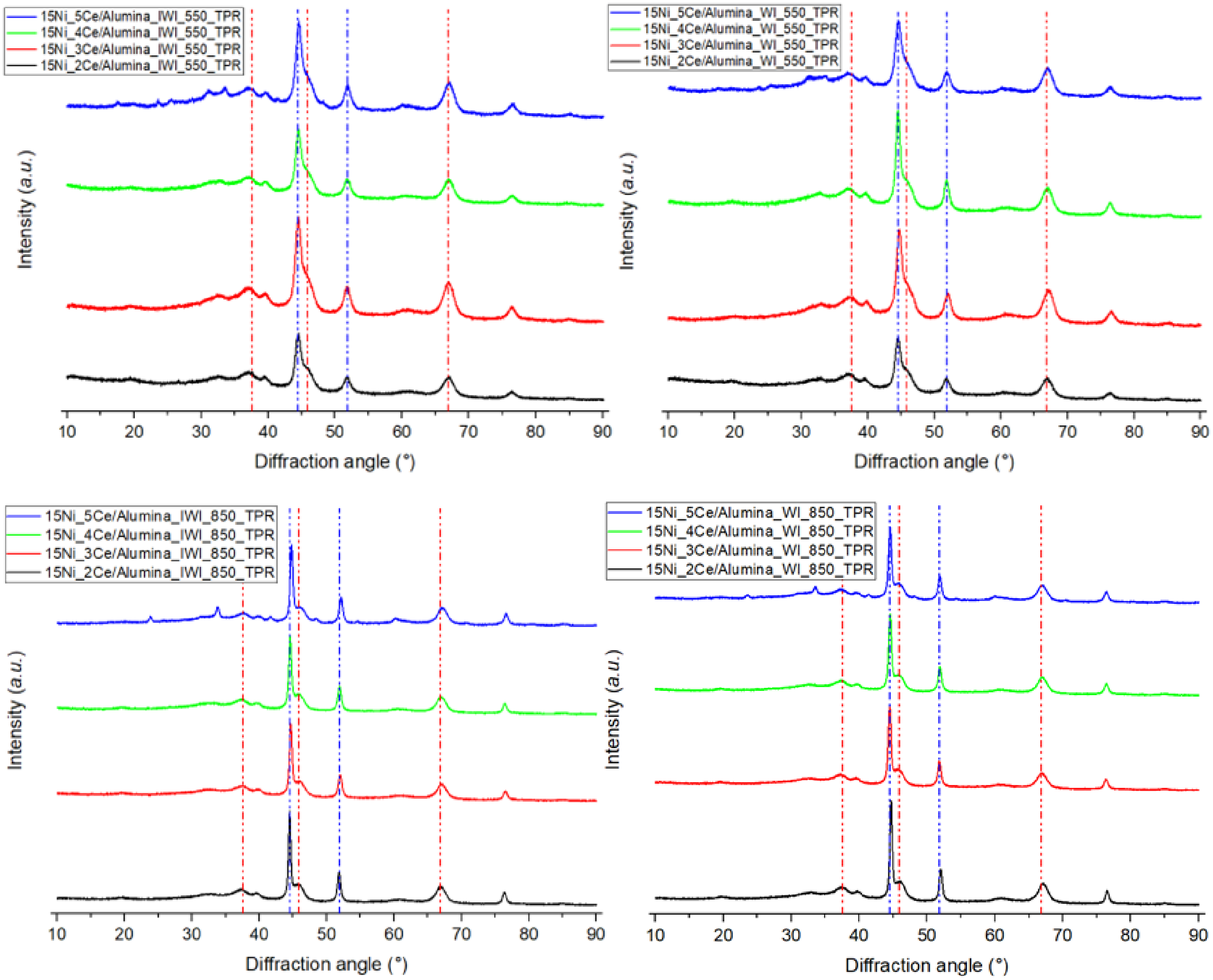

Fig. 4.23 Diffractograms of the reduced 15% nickel promoted catalysts. The vertical dotted lines show the position of the main peaks of γ-alumina (red), and metallic nickel (blue).

Figure 4.23 shows the diffractograms of the promoted catalyst after the temperature programmed-reduction, while Table 4.9 reports the crystallite size of the nickel particles. All catalysts have been completely reduced, forming metallic nickel, appearing the peaks at 44.5° and 51.9°, and maintaining the pattern of the γ-alumina unchanged, avoiding any phase transformation caused by the process.[3,4,27,29,35,48,50,64,67,68,84,94,106,109]

The lack of peaks related to ceria is evident, detecting no material containing cerium. This is caused by the limitation of the instrumentation, since most diffractometers do not allow the determination of particles less than about 5 nm. The reduction allows the partial dissolution of the cerium within the nickel metallic lattice, leading to a decrease of the size of ceria particles below the instrumental limit. In addition, the process also involves the change of the oxidation state of part of the cerium, from +4 to +3, resulting in a drastic alteration of the crystalline structure, creating an amorphous state, not detectable from the XRD analysis.[2–4,7,8,26,27,29,33,35,37,62,65,68,74,84,103,104,106,110,117]

The sizes of metal crystallites are substantially independent of the cerium loading, with the exception of the catalysts calcined at 850°C, observing a decrease in size for higher cerium contents, pointing out that the promoter increases the dispersion of nickel. No differences are seen for the catalysts calcined at 550°C compared to the unpromoted counterparts, while the promoted ones obtained at 850°C are slightly smaller in size due to the greater dispersion caused by cerium.[2,60,68]

15Ni_4Ce/Alumina_WI_550 stands out among all for larger particles, explaining the greater reducibility caused by the less interaction with the support.

A smaller average crystallite size than the average diameter of the support is observed for all the catalysts obtained by IWI method and calcined at 550°C, pointing out that the metal is mainly inside the pores. The opposite is found for the analogues calcined at 850° C, caused by a significant arrangement of the metal on the outer surface or in the connections between channels.[71–73,79]

Table 4.9 Parameters collected by static chemisorption and XRD of the reduced 15% nickel promoted catalysts.

Catalyst	Dispersion (%)	Metallic area (m^2/g)	Crystallite size (nm)	XRD Crystallite size (nm)
15Ni_2Ce/Alumina_IWI_550	5.68	5.67	17.8	9.1
15Ni_2Ce/Alumina_WI_550	5.20	5.19	19.5	8.7
15Ni_3Ce/Alumina_IWI_550	4.78	4.77	21.2	8.4
15Ni_3Ce/Alumina_WI_550	6.28	6.27	16.1	8.6
15Ni_4Ce/Alumina_IWI_550	5.15	5.14	19.6	8.5
15Ni_4Ce/Alumina_WI_550	3.50	3.50	28.9	10.7
15Ni_5Ce/Alumina_IWI_550	5.72	5.71	17.7	9.2
15Ni_5Ce/Alumina_WI_550	6.97	6.96	14.5	8.2
15Ni_2Ce/Alumina_IWI_850	2.39	2.39	42.3	19.3
15Ni_2Ce/Alumina_WI_850	2.19	2.18	46.3	19.5
15Ni_3Ce/Alumina_IWI_850	2.23	2.23	45.4	17.0
15Ni_3Ce/Alumina_WI_850	2.48	2.47	40.9	17.1
15Ni_4Ce/Alumina_IWI_850	2.28	2.27	44.4	16.8
15Ni_4Ce/Alumina_WI_850	2.83	2.82	35.8	16.8
15Ni_5Ce/Alumina_IWI_850	2.43	2.42	41.7	17.3
15Ni_5Ce/Alumina_WI_850	2.37	2.37	42.7	16.5

Table 4.9 reports the dispersion, the metal area and the crystallite size obtained by the static chemisorption of hydrogen for the promoted catalysts. Static hydrogen chemisorption confirms the conclusions from the diffractometry, pointing out the sporadic great size of the metallic crystallites on 15Ni_4Ce/Alumina_WI_550.

4.6 *Zeolites and Zeolite-based catalysts*

To conclude, the characterization of the zeolites and zeolite-based catalysts are reported below, in particular studying the adsorption properties.

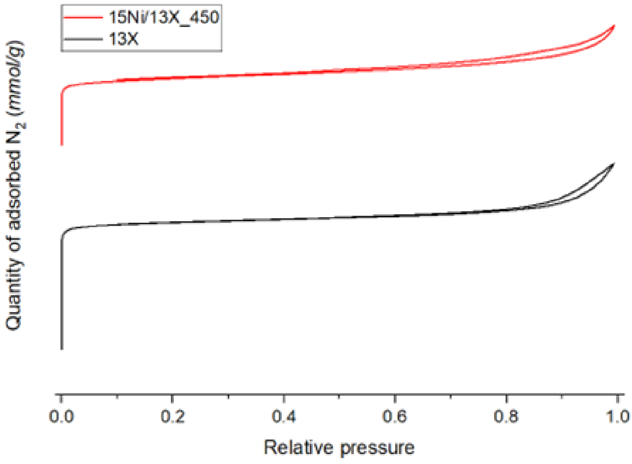

Fig. 4.24 Images of the isotherms of the zeolite 13X-based materials.

Table 4.10 Textural properties and metal loading of the zeolite-based materials.

Material	**Surface area (m^2/g)**	**Pore volume (cm^3/g)**	**Average pore diameter (nm)**	**Metal loading (%)**
13X	710.0	0.39	2.2	-
15Ni/13X_450	362.1	0.25	2.7	15.4
15Ni/4A_450	-	-	-	15.7

Figure 4.24 shows the adsorption isotherms of zeolite 13X and its derived catalyst, while Table 4.10 reports their textural properties. Unfortunately, the instrumentation does not allow the determination of the adsorption and desorption for zeolite 4A and the corresponding catalyst, as well as for the pore size distribution curves.

A rapid increase of the amount of adsorbate is observed at low relative pressures, just above zero, for both the samples. This identifies a type I isotherm, characteristic of a microporous material, forming a monolayer of adsorbate.[17,19,23,118] Hysteresis occurs at higher relative pressures, pointing out the presence of mesopores, caused by gaps between crystallites.[19,90,118]

Impregnation involves a decrease in the surface area and pore volume, while an increase in their average diameter, since the micropores are filling. [3,4,12,24,31–33,50,51,62,69,73,76,78–80,87,89,96,99–101,103,104,106,107] In particular, only a small increase in the average pore size is observed, while the surface area decreases at half of the initial value. This is clearly caused by the deposition of nickel on the outer surface of the zeolite grains, leading to the closure of the pore entrance, due to the excessive amount of precursor and the slow diffusion of it inside such small pores.[11,12,17,25,33,71,73,76,106,117,119]

Table 4.10 reports the nickel loading of the zeolite-based catalysts. The values are very close to the nominal target, pointing out a successful synthesis.

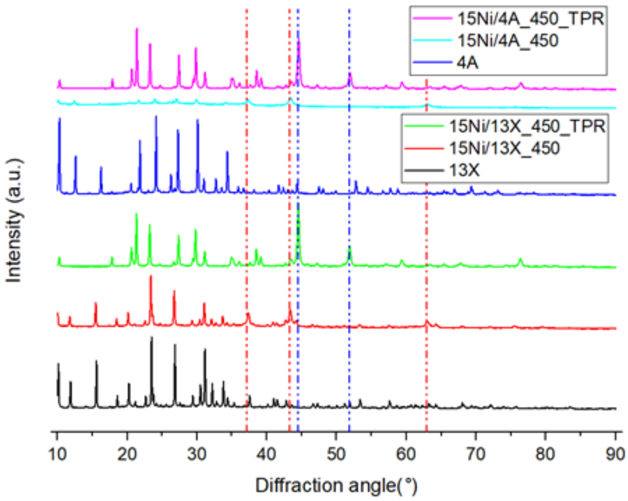

Fig. 4.25 Diffractograms of the zeolites and of calcined and reduced 15% nickel zeolite-based catalysts. The vertical dotted lines show the position of the main peaks of nickel oxide (red), and metallic nickel (blue).

Figure 4.25 shows the diffractograms of the zeolites and of the zeolite-based catalysts. The peaks of nickel oxide appear at 37.2°, 43.3° and 62.9°, while the identification of the zeolites is confirmed by the characteristic diffractometric footprint.[19,20,25,91,119]

The intensity of the peaks related to 13X zeolite is reduced for 15Ni/13X_450, showing that the high temperature in the calcination process causes a decrease in crystallinity. The phenomenon is even more evident for 15Ni/4A_450, whereby the disappearance of the peaks related to the 4A zeolite occurs. This means that, even by limiting the temperatures used to calcine, the thermal process leads to the amorphization of the material.[38,90]

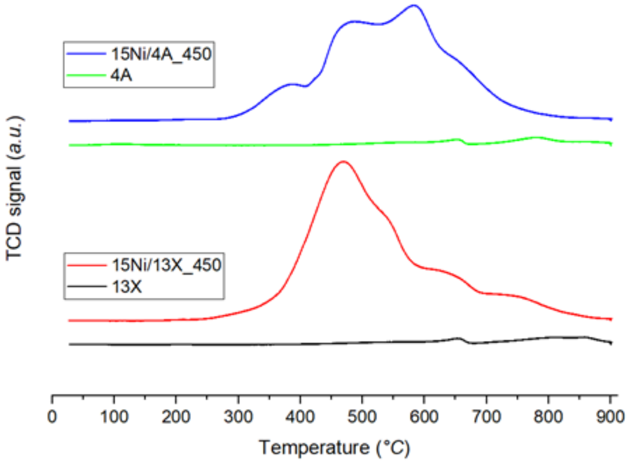

Fig. 4.26 Reduction profile of the zeolites and of the 15% nickel zeolite-based catalysts.

Figure 4.26 shows the reduction profile of the zeolites and zeolite-based catalysts. A small reduction of the material occurs above approximately 630°C for the two zeolites, concluding that a reduction of the catalysts above this temperature causes a physico-chemical change of the support, losing part of its intrinsic porosity.

The presence of multiple peaks is evident for 15Ni/13X_450, caused by the reduction nickel oxide particles with different interaction force with the zeolite, changing their size, and of aluminate and silicate, reducible only at higher temperatures. The maximum is located at 470°C, evidencing that most of the nickel is in the form of oxide particles with weak interaction with the support.

A quite intricate profile is observed for 15Ni/4A_450, caused by the variation of the size of the nickel oxide crystallites, the formation of silicate and aluminate and the occurrence of unsupported nickel oxide, the latter revealed by a reduction peak at 385°C. Although the peaks are overlapping, the maxima of the two major peaks can be isolated at 485°C and 585°C, respectively, provoked by the reduction of large and small nickel oxide particles, which interact differently with the zeolite.

Figure 4.25 shows the diffractograms of the zeolite-based catalysts after the temperature programmed-reduction, while Table 4.11 reports the crystallite size of the nickel particles. The complete reduction to metallic nickel was achieved on all of them, appearing the peaks at 44.5° and 51.9°.[3–5,27,29,35,43,48,50,64,66,67,84,94,96,106,109]

A total change in the crystalline structure of the supports is observed for 15Ni/13X_450 and 15Ni/4A_450, occurring the same diffractometric patterns. Application of high temperature during reduction leads to phase transformation into another aluminosilicate material.[38]

The sizes of the nickel crystallites are larger compared to the average pore diameter, confirming that a lot of metal is deposited on the outer surface of the support.[11,39,71–73,79] Other factors that have allowed this outcome are the less interaction between metal and support, leading to greater migration, and the phase transformation of the zeolite, intrinsically modifying the porosity of the material and rearranging the nickel distribution.[63,84,101,103]

A smaller average crystallite size is observed for 15Ni/4A_450 compared to 15Ni/13X_450, caused by the smaller pore diameter, allowing the creation of tinier particles that better resist sintering and agglomeration.[85]

Table 4.11 Parameters collected by static chemisorption and XRD of the reduced 15% nickel zeolite-based catalysts.

Catalyst	**Dispersion (%)**	**Metallic area (m^2/g)**	**Crystallite size (nm)**	**XRD crystallite size (nm)**
15Ni/13X_450	1.37	1.37	73.8	30.4
15Ni/4A_450	1.97	1.67	51.4	25.6

Table 4.11 reports the dispersion, the metal area and the crystallite size obtained by the static chemisorption of hydrogen for the zeolite-based catalysts. Static hydrogen chemisorption confirms

the assumptions from diffractometry, evidencing a larger crystallite size for 15Ni/13X_450 compared to 15Ni/4A_450.

Thermogravimetry is performed to evaluate the adsorption properties of zeolites, applying different parameters and gases. The zeolites are able to adsorb water due to the strong interaction between the ions in them and the dipole moment of the water molecules.[1]

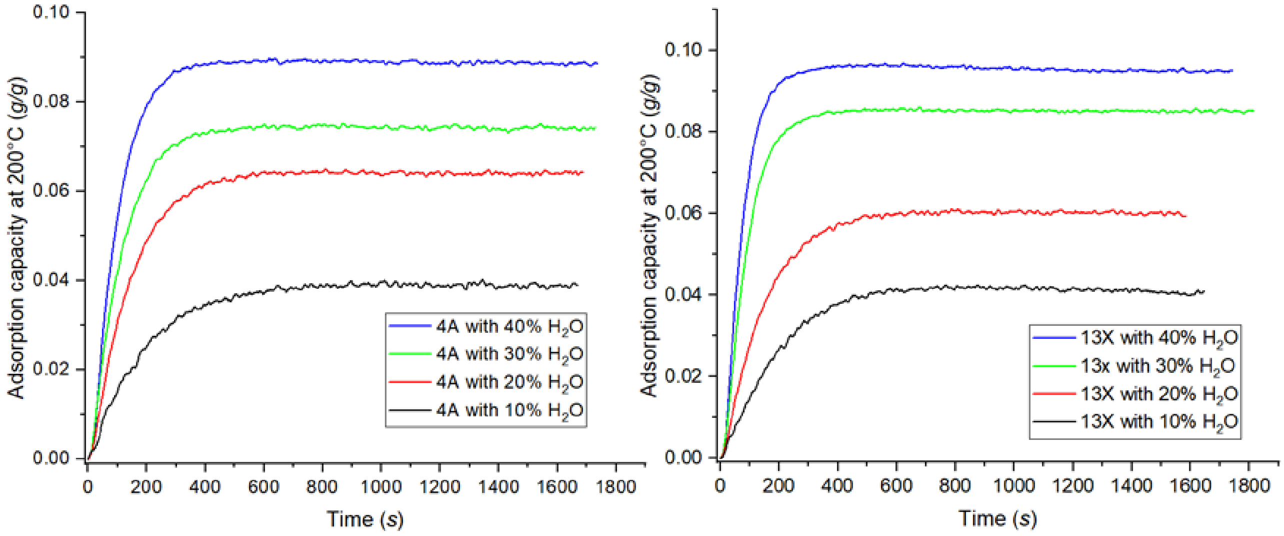

Fig. 4.27 Adsorption profile at different water content for zeolites.

Figure 4.27 shows the water adsorption profiles of the zeolites at different water contents. An increase of the water content in the gas corresponds to an increase in the adsorption capacity for both zeolites, since more reagent is being supplied, shifting the equilibrium towards the occupation of the adsorption sites. The adsorption kinetics are quite rapid, reaching the steady state after a short induction period. In particular, an increase in water content causes a decrease in induction time, accelerating the occupation of the adsorption sites.[14,23,90]

Zeolite 13X has a higher adsorption capacity compared to 4A, being evident for water contents higher than 30% by volume. Furthermore, the induction times are shorter for 13X compared to 4A, making it obvious that the two phenomena are related. This is caused by the higher surface area of the zeolite 13X compared to the 4A, offering a major number of sites for the adsorption of water.[17,19,25,85,118]

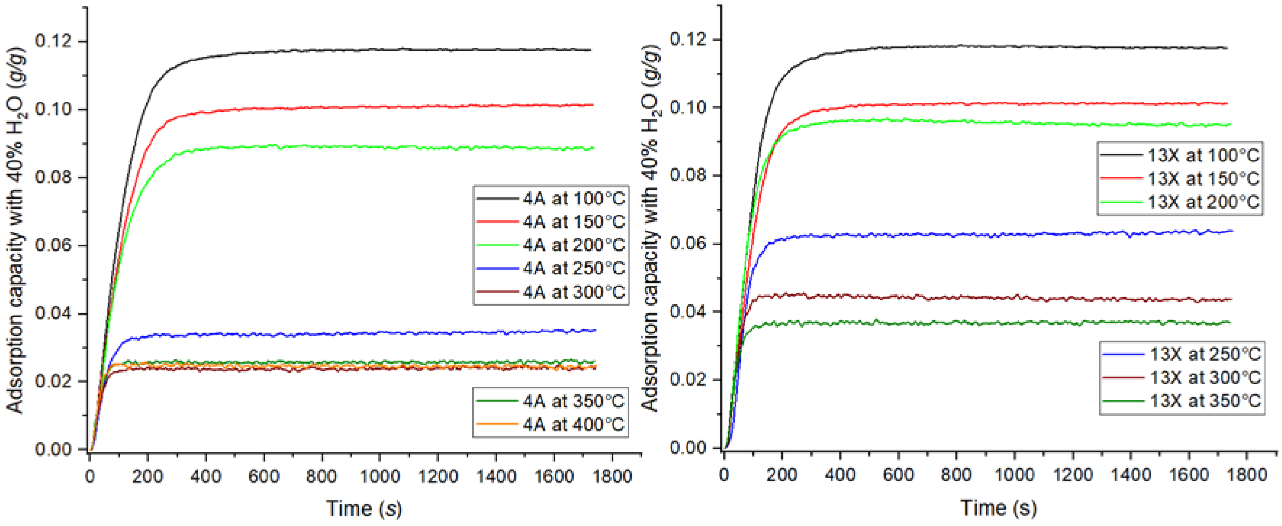

Fig. 4.28 Adsorption profile of water at diverse temperature for zeolites.

Figure 4.28 shows the water adsorption profiles of the zeolites at different temperatures. An increase in temperature corresponds to a decrease in the adsorption capacity of the zeolite due to the exothermic nature of the adsorption process. In particular, the ascending portion of the curve is very similar in all cases, regardless of the temperature. An increase of the temperature causes a decrease in the adsorption capacity, leading to a reduction in the induction time, showing an effect on the adsorption kinetics.[1,9,13,14,20,21,23,38,49,90,92,118]

It is observed that 13X has a greater water adsorption capacity compared to 4A over 200°C, while for lower temperatures there is no substantial difference. 4A zeolite shows no change in water adsorption capacity above 300°C.[17,19,25,85,118]

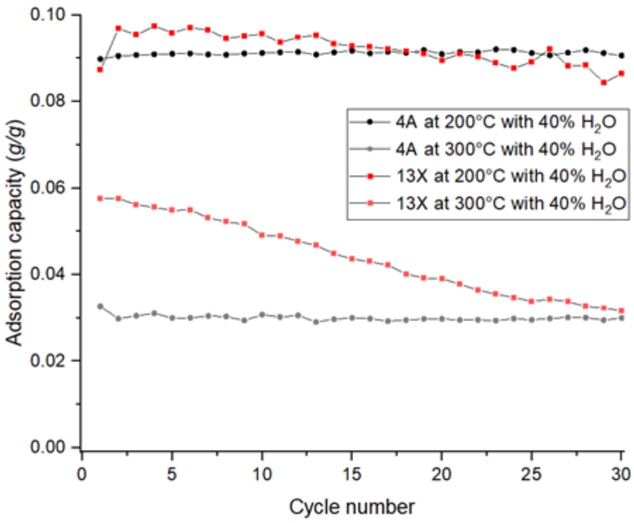

Fig. 4.29 Evolution of the adsorption water capacity of zeolites after 30 adsorption-desorption cycles.

Figure 4.29 shows the evolution of water adsorption capacity over various adsorption and desorption cycles. The zeolite stability test shows that 4A is very stable, not changing its adsorption capacity even at 300°C, while 13X shows a degradation process, mild at 200°C while quite severe at 300° C, decreasing of 0.0259 g after 30 cycles. However, 13X shows a higher adsorption capacity than 4A at 300°C even after 30 cycles, compensating its lower stability with a greater affinity to water.[9,13,14,90,120]

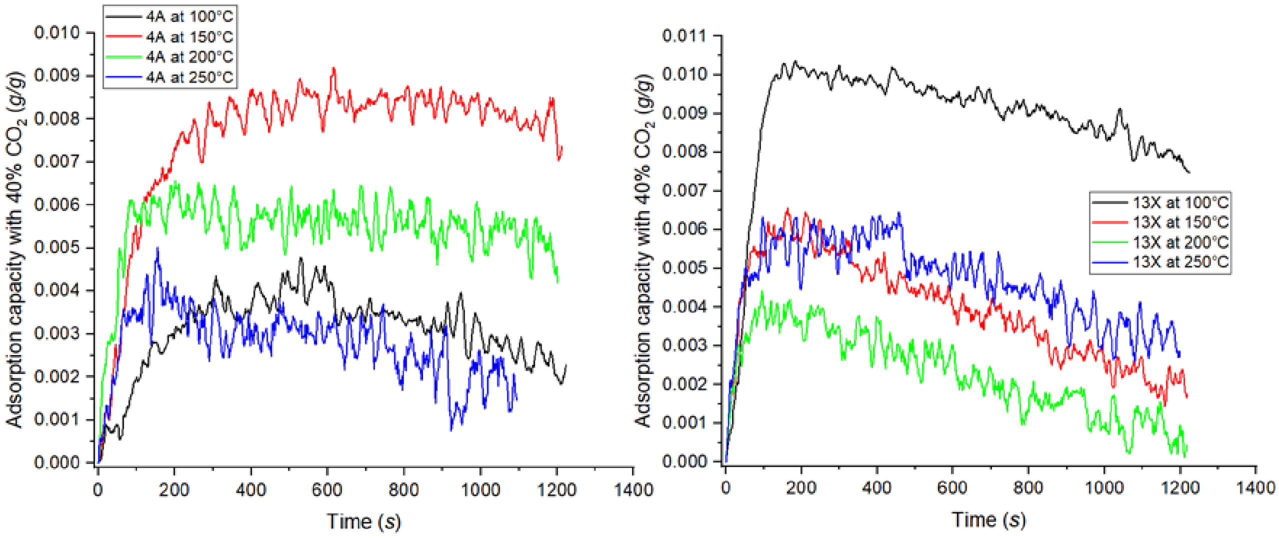

Fig. 4.30 Adsorption profile of carbon dioxide at diverse temperature for zeolites.

Figure 4.30 shows the carbon dioxide adsorption profile of the zeolites at different temperatures. The ions in the zeolites should be able to interact with the quadrupole of the carbon dioxide, leading to the adsorption of the reagent. However, the adsorbed carbon dioxide is so low that the signal is too weak to overcome the noise, resulting in unreliable measurements. The only certainty is that the carbon dioxide adsorption capacity of both zeolites is negligible at all temperatures, due to the exothermic nature of the process.[1,13,14,17,19–21,23,25,39]

Several studies have shown that in case of competitive adsorption between water and carbon dioxide, the greater affinity of the zeolite sites for the water leads to a notable decrease in the adsorption of the reagent. Therefore, it is plausible to assume that the dioxide is not adsorbed during the methanation.[21,23,92]

The descending trends of the plateaux are caused by the slow removal of the last traces of moisture, not eliminated after 30 minutes of desorption in a nitrogen atmosphere.

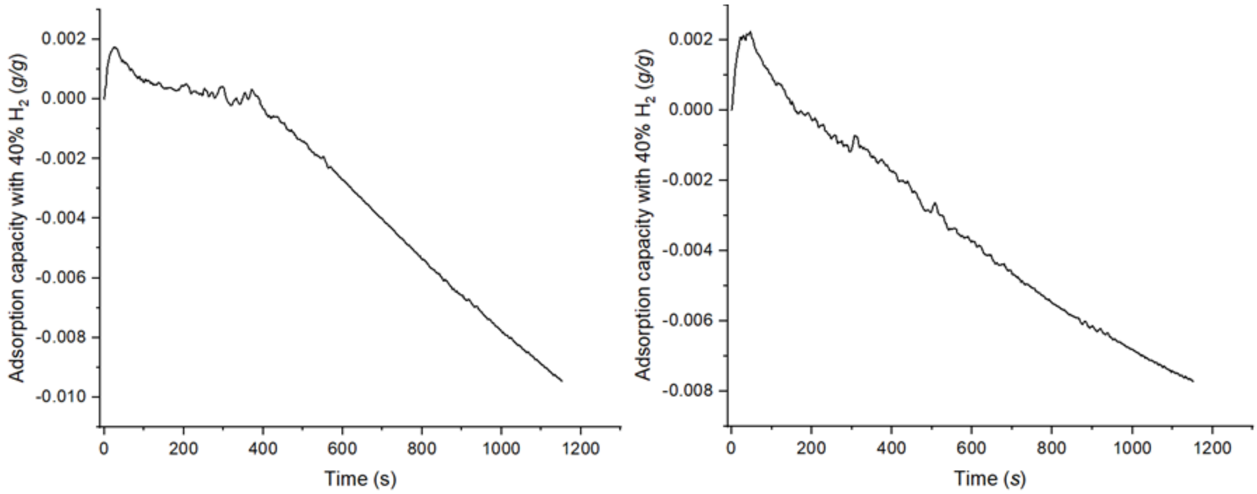

Fig. 4.31 Adsorption profile of hydrogen at diverse temperature for zeolite 4A, on the left, and 13X, on the right.

Figure 4.31 shows the carbon dioxide adsorption profile of the zeolites at different temperatures. In this case, it is clear that no adsorption occurs, not even at 100°C, due to the low polarizability of the molecule.[1] The slight increase in mass initially occurred is caused by the change of the gas flowed in the instrumentation, losing temporarily the calibration and collecting meaningless data.

5. METHANATION OF CARBON DIOXIDE

5.1 *Traditional methanation*

It was decided to carry out the catalytic tests only on catalysts obtained by WI synthesis, since similar properties were found for the Alumina-based catalysts with the two synthesis methods. This decision was taken considering the applicability of this method at an industrial scale. Such conclusion is not obvious, since many studies have shown that different synthesis techniques can significantly impact the physico-chemical properties of catalysts, altering their catalytic performances. An example is provided by sol-gel synthesis, which generally gives very high porosities, sometimes at the expense of less stability of the support.[35,49,84,103,104,106]

In the following, the different performances of the catalysts are reported, explaining their activities and selectivity with the characterization previously performed.

Table 5.1 Catalytic performance of the 15% nickel catalysts.

Catalyst	**Conversion of CO_2 (%)**	**Selectivity of CH_4 (%)**	**Selectivity of CO (%)**	**Yield of CH_4 (%)**
15Ni/Alumina_WI_550	49.2	97.03	2.97	47.8
15Ni/Alumina_WI_850	27.8	92.43	7.57	25.7
15Ni/TitaniaP25_550	20.0	96.73	3.27	19.4
15Ni/Anatase_550	0.8	0.00	100.00	0.0
15Ni/Anatase_850	2.9	28.57	71.43	0.8
15Ni/Zirconia_550	50.7	98.89	1.11	50.1
15Ni/Zirconia_850	32.1	98.58	1.42	31.6

Table 5.1 reports the conversion, selectivity and yield of the reaction, using nickel catalysts. A low conversion is observed for the titania-based catalysts. In particular, 15Ni/Anatase_550 shows the worst results, with almost no conversion, due to the covering of the nickel particles with a few atomic layers of reduced titania, isolating the active phase from the reagents and preventing the methanation. Furthermore, the interaction involves a modification of the electronic properties of the nickel, resulting in higher selectivity to carbon monoxide.[5,6,24,27,34,37,63,64,96,121]

15Ni/Anatase_850 shows slightly increased conversion, as well as increased selectivity for methane. This is caused by the formation of smaller metal particles, showing greater active area and sites to carry out methanation. The high temperature causes the collapse of the porosity, so the active metal is deposited on the outer surface of the support, obtained by the reduction of the nickel titanate. The unreduced mixed oxide acts as a barrier between titania and nickel, limiting the contact and reducing the change in electronic properties, leading to increased methane formation.[6]

The initial presence of rutile allows the attenuation of the strong metal-support interaction for 15Ni/TitaniaP25_550, exposing a greater metallic area to carry out methanation. Also, the initial interaction with rutile does not lead to a reduction in selectivity towards methane, contrary to anatase, therefore the catalyst is more selective. Such phenomenon is caused by the change of the interaction energy between the support and the carbon monoxide, detecting an easier release for anatase, without completing the reduction, while a difficult one for rutile, going on with the hydrogenation to methane.[5,6,24,27,37,53,63,64,74,94,96,122]

The most promising results are obtained for catalysts prepared from Alumina or Zirconia. 15Ni/Alumina_WI_550 shows good conversion caused by the high surface area, on which carbon dioxide is adsorbed and activated towards the reaction, and by the high dispersion of metal, exposing a greater number of active sites.[2–5,26,31,33,35,50,54,62,65,76,78,101,103] 15Ni/Zirconia_550 shows good activity due to the reducibility of the support, forming a multitude of oxygen vacancies which act as preferential adsorption and activation sites for carbon dioxide, simplifying and directing the reactivity towards the selective production of methane.[2,5,10,11,33,40,57,62,66,85,87,103]

DFT calculations and TEM images have shown that carbon dioxide and monoxide, two of the most important species in the catalytic system, are preferentially adsorbed on the interface between zirconia and nickel. This points out that the support does not just have a passive role, but rather interacts with the adsorbates and the active phase, altering their electronic properties and promoting the development of the hydrogenation.[36]

A decrease in conversion occurs for 15Ni/Alumina_WI_850 and 15Ni/Zirconia_850, caused by the sintering of the metal or support, reducing the number of available active sites. The change in the calcination temperature causes a decrease in selectivity towards methane for 15Ni/Alumina_WI_850, due to the formation of bigger nickel crystallites, outside the optimal range to carry out a selective methanation. On the other hand, 15Ni/Zirconia_850 is different, showing a slight decrease of the selectivity, since the oxygen vacancies favor the creation of methane.[3,10,26,33,50]

Table 5.2 Catalytic performance of the 15% cobalt catalysts.

Catalyst	**Conversion of CO_2 (%)**	**Selectivity of CH_4 (%)**	**Selectivity of CO (%)**	**Yield of CH_4 (%)**
15Co/Alumina_WI_550	40.4	79.12	20.88	31.9
15Co/Anatase_550	0.5	21.50	78.50	0.1
15Co/Zirconia_550	43.7	90.27	9.73	39.5

Table 5.2 reports the conversion, selectivity and yield of the reaction, using cobalt catalysts. 15Co/Anatase_550 shows a low conversion, caused by the partial coating of the cobalt particles with a layer of reduced titania. However, greater selectivity towards methane is evident, due to less alteration of the electronic properties of the metal caused by less interaction with the support compared to nickel, allowing an easier hydrogenation and a smaller metal particle size, approaching the optimal dimensions to carry out methanation. [5,6,15,24,27,34,37,57,63,64,96,121]

Better performances are observed for 15Co/Alumina_WI_550 and 15Co/Zirconia_550, in particular the conversion is quite high, although not as high as that obtained with the corresponding nickel catalysts. The observed trend is the same, concluding that the causes of the high activity are the high surface area and the reducibility of the support, forming surface oxygen vacancies.[2,10,11,15,50,85,103]

Various studies have shown an excellent interaction between cobalt and zirconia, resulting in the formation of a mixed species at the interface. It is believed that this phase has excellent catalytic performance, allowing a good conversion of reagents.[15,103]

Even if the metallic areas exposed by cobalt are significantly small, compared to the nickel ones, the conversions are not drastically different. Such damping of the conversion collapse is caused by the greater intrinsic activity of cobalt compared to nickel, for equal metallic area.[10,15]

A lower tendency towards hydrogenation is observed for cobalt compared to nickel, increasing the production of carbon monoxide. The difference is quite large for 15Co/Alumina_WI_550, while it is limited for 15Co/Zirconia_550, due to the guidance of the reactivity towards the production of methane caused by the oxygen vacancies, maintaining excellent yields.[3,10,26,33]

Table 5.3 Catalytic performance of the 10% metal catalysts.

Catalyst	**Conversion of CO_2 (%)**	**Selectivity of CH_4 (%)**	**Selectivity of CO (%)**	**Yield of CH_4 (%)**
10Ni/Alumina_WI_550	25.3	93.30	6.70	23.6
10Co/Alumina_WI_550	29.0	57.70	42.30	16.7

Table 5.3 reports the conversion, selectivity and yield of the reaction, using lower metal loading catalysts. The catalytic test was carried out only on the catalysts calcined at 550°C, identifying this temperature as the most suitable to create efficient catalysts. A reduction of the conversion is observed for 10Ni/Alumina_WI_550 and 10Co/Alumina_WI_550, caused by a decrease of the metallic area, connected to the lower amount of metal and the greater formation of aluminates, leading to less available active sites to carry out methanation.[3,6,10,15,29,35,47,50,61,67,73,80,87,111]

On the other hand, there is also a decrease of the selectivity to methane, increasing the percentage of carbon monoxide produced. This phenomenon is caused by the creation of smaller and defective metal particles, rich in edge and vertex sites on which carbon monoxide is adsorbed with lower interaction energy than on a crystalline face. The less interaction allows for easier desorption of the intermediate, without completing the hydrogenation.[10,41,81,83]

In addition to the formation of more uncoordinated sites, the production of smaller metal particles, especially for cobalt, changes the electronic properties, modifying the interaction with the adsorbates, resulting in a dramatic decrease of conversion and selectivity.[41,54,72,81,85,102,114,123]

A greater conversion is provided by 10Co/Alumina_WI_550 compared to 10Ni/Alumina_WI_550, evidencing the greater activity of the cobalt active sites.[10,15]

Before to expose the performances of the promoted catalysts, the contents of nickel and cerium are determined, in order to fully understand how the reactivity varies in relation to the promoter loading. For this purpose, an inductively coupled plasma optical emission spectroscopy, ICP-OES, is carried out.

Table 5.4 Metal content of the 15% nickel promoted catalysts, by ICP-OES.

Catalyst	**Nickel loading (%)**	**Cerium loading (%)**	**Ni/Ce mass ratio**
15Ni_2Ce/Alumina_WI_550	9.1	1.3	6.8
15Ni_3Ce/Alumina_WI_550	12.1	2.6	4.6
15Ni_4Ce/Alumina_WI_550	12.1	3.2	3.8
15Ni_5Ce/Alumina_WI_550	10.8	3.7	2.9
15Ni_3Ce/Alumina_WI_850	12.2	2.3	5.2

Table 5.4 shows the cerium and nickel loadings of the promoted catalysts. A difference from the values obtained by XRF is observed. This is caused by the different type of characterization technique and way of preparing the sample for analysis. In particular, an excessive dilution of the solutions

obtained by digestion of the catalysts is plausible. The Ni/Ce mass ratios are in agreement with the nominal ones.

Table. 5.5 Catalytic performance of the 15% nickel promoted catalysts.

Catalyst	**Conversion of CO_2 (%)**	**Selectivity of CH_4 (%)**	**Selectivity of CO (%)**	**Yield of CH_4 (%)**
15Ni_2Ce/Alumina_WI_550	55.7	98.33	1.67	54.7
15Ni_3Ce/Alumina_WI_550	52.7	98.68	1.32	52.0
15Ni_4Ce/Alumina_WI_550	65.3 ± 0.8	99.19 ± 0.02	0.81 ±0.02	64.7 ± 0.8
15Ni_5Ce/Alumina_WI_550	60.5	98.69	1.31	59.7
15Ni_3Ce/Alumina_WI_850	45.1	97.52	2.48	43.9

Table 5.5 reports the conversion, selectivity and yield of the reaction, using promoted catalysts. An increased conversion and selectivity are evident for all catalysts compared to the unpromoted counterparts, pointing out a positive effect of cerium on the performance of nickel. The increase in selectivity is quite limited since nickel is already intrinsically very selective, while the increase in conversion is substantial, significantly improving the performance. Such effect is caused by the greater dispersion of nickel, the increase of the basicity, provided by different sites, like oxygen vacancies, and allowing an easier and higher adsorption of carbon dioxide, and the alteration of the electronic properties of nickel, incrementing the electron density responsible for the dissociation of reagents and intermediates.[2,9–11,31–33,36,52,57,60–62,68,75,87]

The reaction was also carried out on 15Ni_3Ce/Alumina_WI_850 to validate the previous results, confirming that an increase in the calcination temperature is harmful to the efficiency of the catalyst.[26,50]

An increase of conversion for catalysts calcined at 550°C is observed up to a 4% cerium loading, for 15Ni_4Ce/Alumina_WI_550, followed by a decrease for the next sample. This may be caused by various phenomena, therefore a comparison between the trends of the conversions and various parameters is carried out to understand the causes.

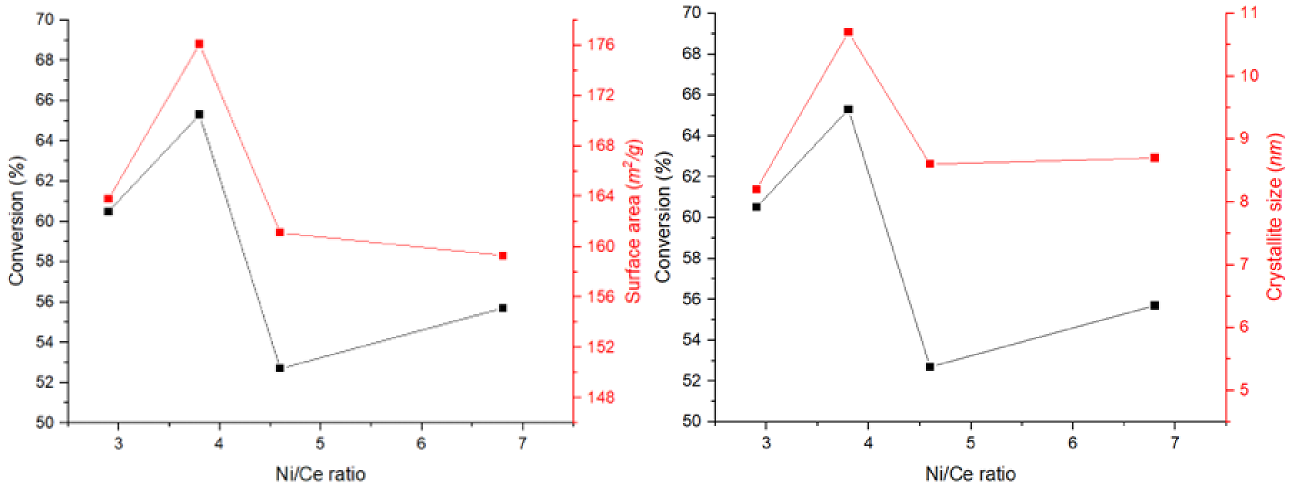

Fig. 5.1 Correlation of the conversions with the surface areas, on the left, and with the XRD crystallite sizes, on the right, for the 15% nickel promoted catalysts.

Figure 5.1 shows the correlations between the trends of the conversions and the surface areas and between conversions and the crystallite sizes for the promoted catalysts. An excellent correspondence is evident for both the parameters.

A large surface area allows the formation of more adsorption sites, transforming of a greater amount of carbon dioxide molecules, while bigger crystallites result in improved nickel reducibility, confirmed by the temperature- programmed reduction, reducing more oxide to metal and providing more metallic active sites for hydrogenation.[15,24,28,50,64,70,73,74,78,80,81,85,103,106,107,114] The two parameters have the same trend, so a connection cannot be ruled out.

5.2 *Stability tests*

The methanation of carbon dioxide is carried out for 70 consecutive hours to understand the effect of cerium on the stability of the catalyst.

Table. 5.6 Catalytic performance after 70 hours of methanation of the 15% nickel catalysts, with and without cerium.

Catalyst	**Conversion of CO_2 (%)**	**Selectivity of CH_4 (%)**	**Selectivity of CO (%)**	**Yield of CH_4 (%)**
15Ni/Alumina_WI_550	48.3	96.48	3.52	46.6
15Ni_3Ce/Alumina_WI_550	55.3	98.56	1.44	54.5

Table 5.6 reports the conversion, selectivity and yield of the reaction for the selected catalysts after 70 hours of reaction. The conversion and selectivity slightly decrease for 15Ni/Alumina_WI_550, while the conversion increases for 15Ni_3Ce/Alumina_WI_550 and its selectivity remained essentially unchanged. These differences are minimal, too small to be significant.[29]

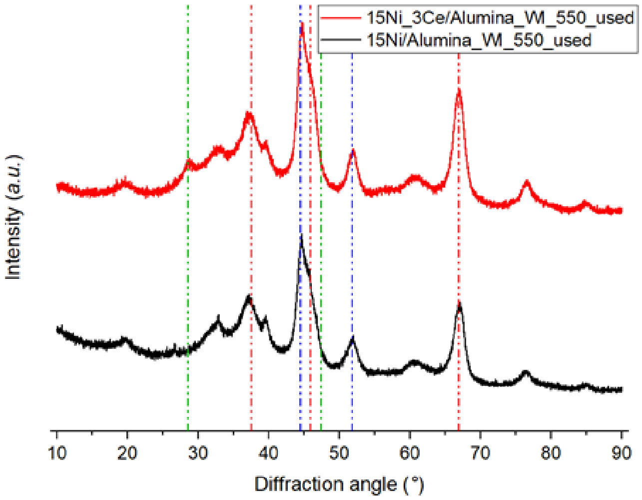

Fig. 5.2 Diffractograms of the used 15% nickel catalysts, after 70 hours of methanation. The vertical dotted lines show the position of the main peaks of γ-alumina (red), metallic nickel (blue), and cerianite (green).

Figure 5.2 shows the diffractograms of the used catalysts after 70 hours of reaction. No signal related to carbon coke appear in the diffractometric pattern of the two catalysts, showing that its deposition is negligible after 70 hours. On the other hand, the peaks of metallic nickel and γ-alumina are clearly distinguishable, followed by the weak signal of cerianite, distinctly visible only at 28.6°, for 15Ni_3Ce/Alumina_WI_550.[2,29,30,47,50,69,84]

Table 5.7 Crystallite size of the used 15% nickel catalysts by the XRD.

Catalyst	XRD crystallite size (nm)
15Ni/Alumina_WI_550	6.0
15Ni_3Ce/Alumina_WI_550	6.3

Table 5.7 reports the crystallite size of the nickel particles on the used catalysts. Similar crystallite sizes are recorded for the two used catalysts. Smaller values are obtained compared to the same samples after temperature-programmed reduction due to the different activation process.

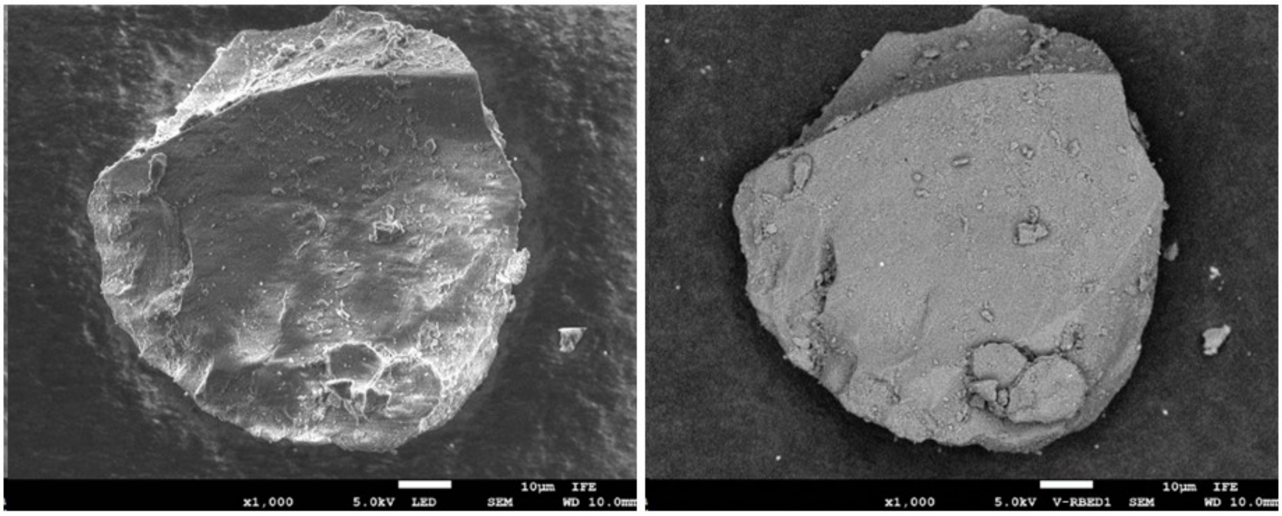

Fig. 5.3 SEM images of calcined 15Ni/Alumina_WI_550 obtained by secondary electrons, on the left, and backscattered electrons, on the right.

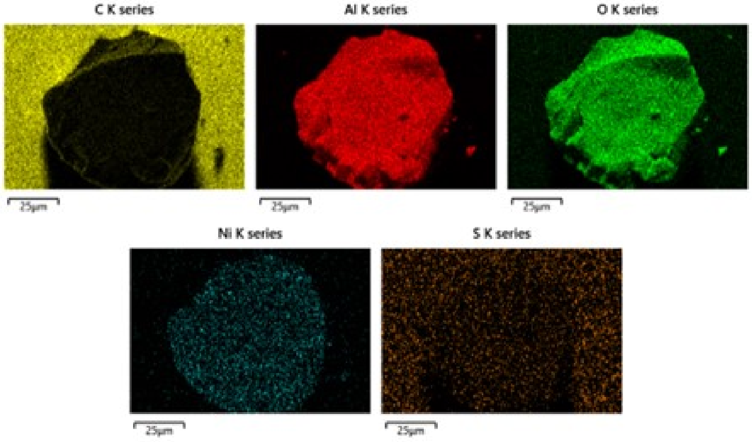

Fig. 5.4 SEM images of calcined 15Ni/Alumina_WI_550, obtained by energy-dispersive spectroscopy, visualizing the distribution of the elements.

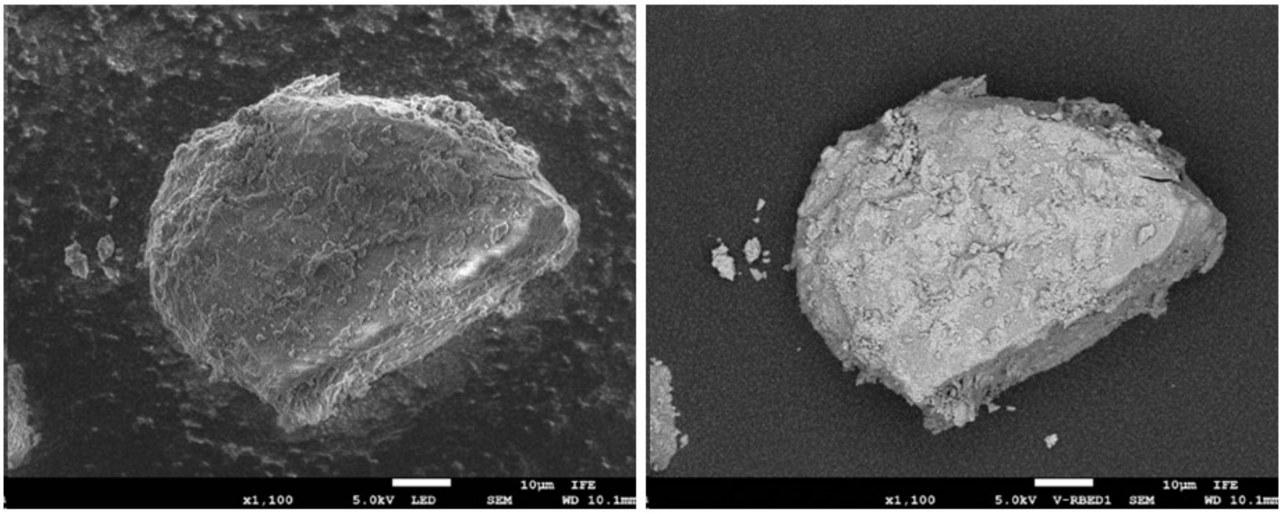

Fig. 5.5 SEM images of calcined 15Ni_3Ce/Alumina_WI_550 obtained by secondary electrons, on the left, and backscattered electrons, on the right.

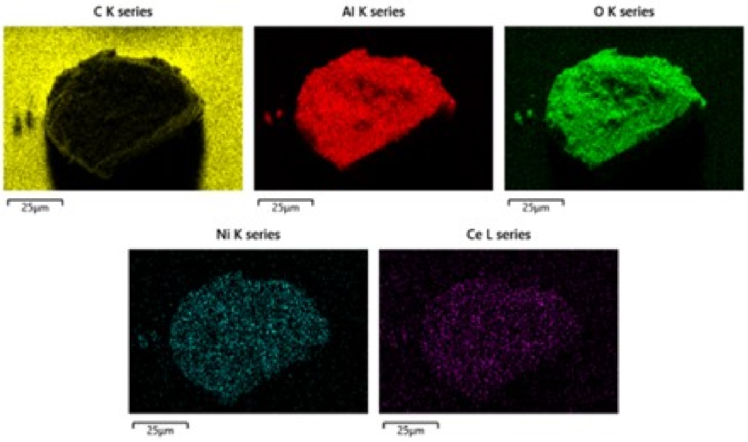

Fig. 5.6 SEM images of calcined 15Ni_3Ce/Alumina_WI_550, obtained by energy-dispersive spectroscopy, visualizing the distribution of the elements.

Figures 5.3, 5.4, 5.5 and 5.6 show the SEM images of the calcined catalysts, before the methanation. Sometimes, images of secondary electrons show very light areas, caused by the accumulation of electric charge on the sample due to its insulating nature. EDX spectroscopy identifies some elements not introduced by the synthesis, brought by the graphite support used to immobilize the powder.

The particles of 15Ni_3Ce/Alumina_WI_550 shows a rougher surface compared to the ones of 15Ni/Alumina_WI_550, caused by the formation of protrusions on the support grain. This is particularly evident in the backscattered electrons images. Such appearance is caused by the formation of smaller oxide particles, which create a less smooth surface.[60]

EDX spectroscopy evidences a homogeneous distribution of nickel and cerium on the catalysts. This is confirmed by the absence of clear spots in the backscattered electrons images, which would have identified agglomerations of metals.[4,51]

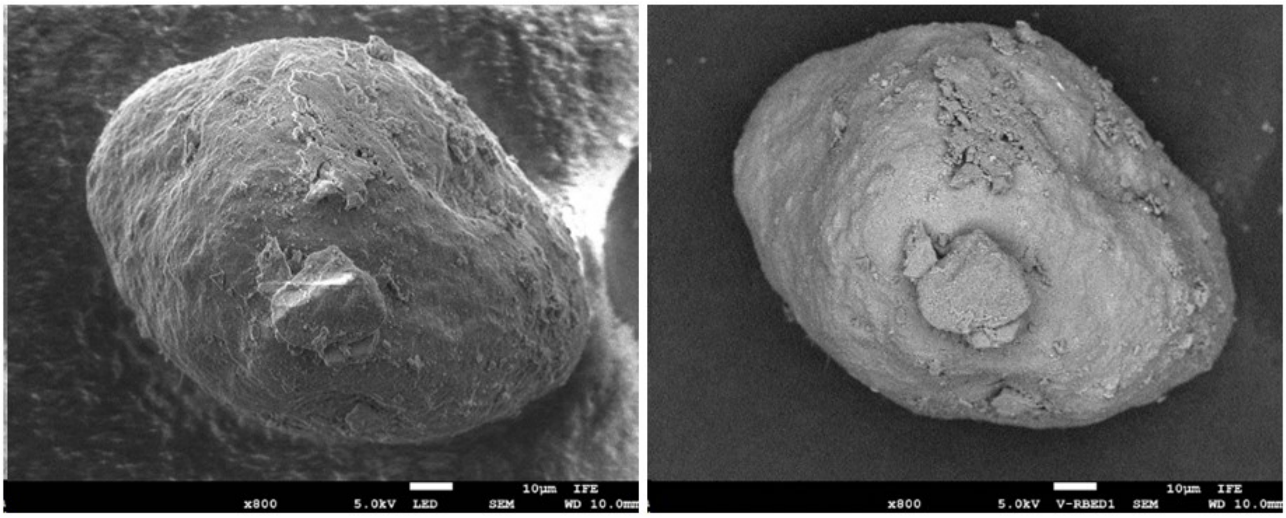

Fig. 5.7 SEM images of used 15Ni/Alumina_WI_550 obtained by secondary electrons, on the left, and backscattered electrons, on the right.

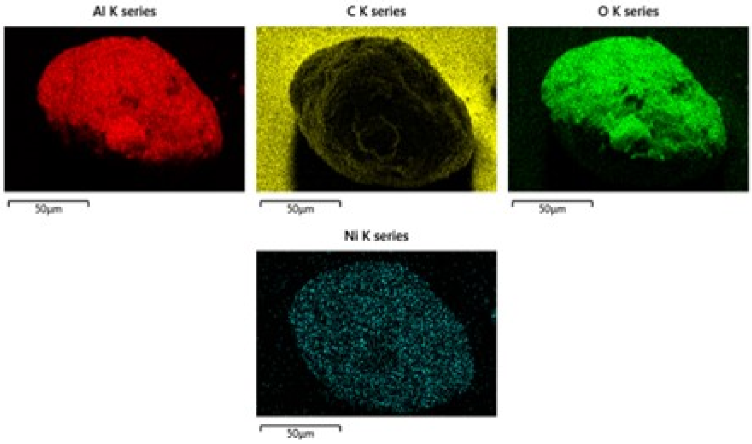

Fig. 5.8 SEM images of used 15Ni/Alumina_WI_550, obtained by energy-dispersive spectroscopy, visualizing the distribution of the elements.

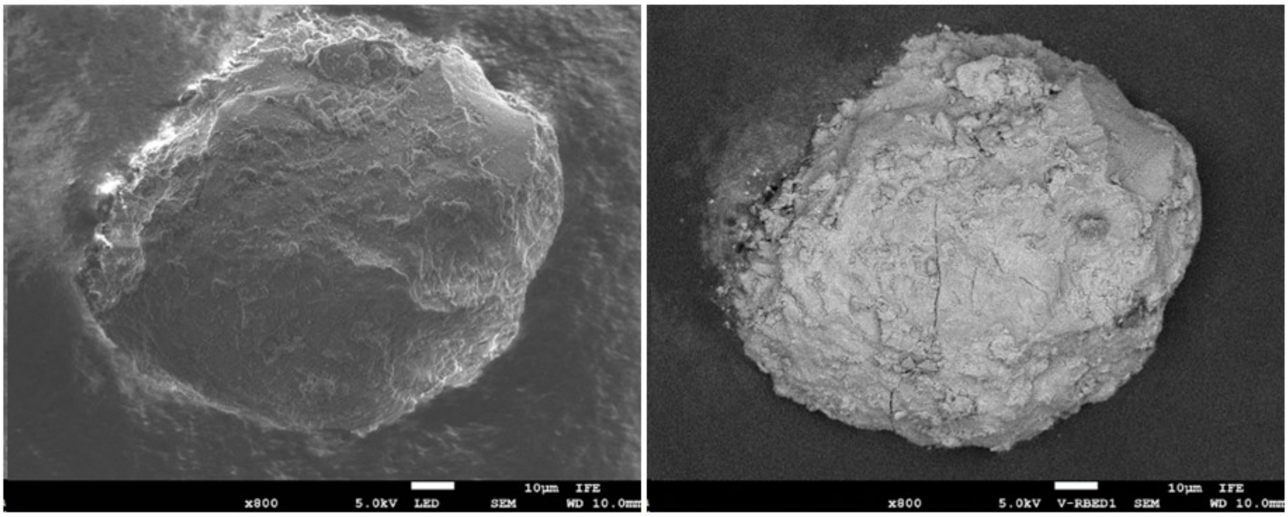

Fig. 5.9 SEM images of used 15Ni_3Ce/Alumina_WI_550 obtained by secondary electrons, on the left, and backscattered electrons, on the right.

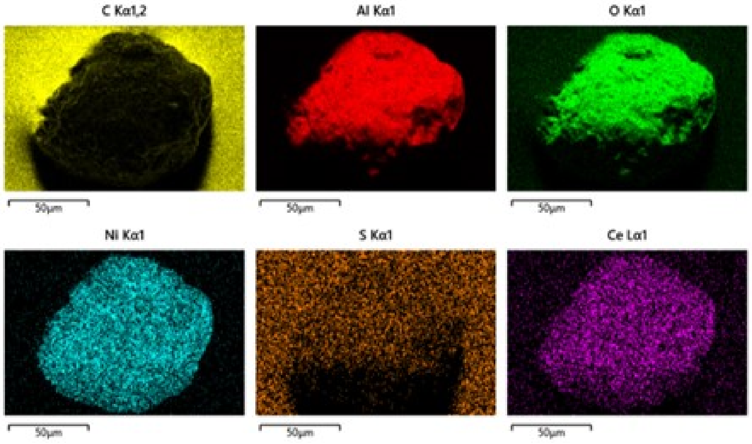

Fig. 5.10 SEM images of used 15Ni_3Ce/Alumina_WI_550, obtained by energy-dispersive spectroscopy, visualizing the distribution of the elements.

Figures 5.7, 5.8, 5.9 and 5.10 show the SEM images of the used catalysts, after 70 hours of methanation. The high roughness of 15Ni_3Ce/Alumina_WI_550 is observed once again, suggesting that sintering did not occur significantly to affect the morphology of the catalyst. The backscattered electrons image of 15Ni_3Ce/Alumina_WI_550 evidences some fractures along the grain, probably caused by the permanence of the sample in the reactor, exposed to high temperatures.

No agglomeration of nickel or cerium is observed, based on the absence of clear spots in the backscattered electrons images and the good distribution of the elements shown by EDX spectroscopy.[4,51]

The introduction of cerium should allow the oxidation of carbon coke deposits to carbon dioxide and monoxide by metal centers with a high oxidation state and the limitation of sintering due to an increase of the nickel dispersion and interaction with the support.[31,60–62,65,66,68] The results of the stability tests point out that both 15Ni/Alumina_WI_550 and 15Ni_3Ce/Alumina_WI_550 show no signs of deactivation for 70 hours of continued reactivity.[29]

5.3 *Sorption-enhanced methanation*

In the following, the different performances of the zeolite-based catalysts are reported.

Table 5.8 Catalytic performance of the 15% nickel zeolite-based catalysts.

Catalyst	**Conversion of CO_2 (%)**	**Selectivity of CH_4 (%)**	**Selectivity of CO (%)**	**Yield of CH_4 (%)**
15Ni/13X_450	19.6	53.88	46.12	10.6
15Ni/4A_450	21.4	38.82	61.18	8.3

Table 5.8 reports the conversion, selectivity and yield of the reaction, using zeolite-based catalysts. Low conversions and selectivity for methane are observed, preferring the formation of carbon monoxide, in particular for 15Ni/4A_450.

The low conversion of carbon dioxide is caused by the closure of the pores and collapse of the porosity of the zeolites due to the thermal treatments, leading to the sequestration of nickel and the decrease of adsorption sites for the capture of water. The transformation of zeolite into aluminosilicate also leads to the loss of its water adsorption capacity, therefore it is not possible to find any sorption-enhancement, since the water produced by methanation is not removed away from the active site.[9,117]

15Ni/4A_450 shows a better conversion than that of 15Ni/13X_450, since the nickel dispersion is higher, allowing the creation of a greater surface metallic area, therefore more active sites. Poor selectivity is observed, since the weak interaction with the support allows the agglomeration of the metal into quite large particles, outside the optimal range of methane production.

To deal with the degradation of the zeolite, it was added to the catalytic bed to replace the quartz, not using it as a support. Below, the results are reported, using the most active and selective catalyst, 15Ni_4Ce/Alumina_WI_550, and the zeolite with the greatest water adsorption capacity, 13X.

Table 5.9 Catalytic performance of the 15Ni_4Ce/Alumina_WI_550 under different working conditions, with and without zeolite 13X.

Catalyst	**Conversion of CO_2 (%)**	**Selectivity of CH_4 (%)**	**Selectivity of CO (%)**	**Yield of CH_4 (%)**
350°C, 200 mL/min	65.3 ± 0.8	99.19 ± 0.02	0.81 ±0.02	64.7 ± 0.8
with 13X	70.5	99.28	0.72	70.0
	70.6	99.32	0.68	70.1
	70.6	99.32	0.68	70.1
300°C, 200 mL/min	25.6	98.28	1.72	25.1
with 13X	28.7	98.60	1.40	28.3
	28.2	98.58	1.42	27.8
	28.3	98.62	1.38	27.9
300°C, 100 mL/min	41.7	99.13	0.87	41.3
with 13X	59.4	99.49	0.51	59.1
	59.9	99.52	0.48	59.6
	60.0	99.53	0.47	59.7
300°C, 100 mL/min, ratio 11:1	28.3	98.12	1.88	27.8
with 13X	29.4	97.99	2.01	28.8
	30.9	98.11	1.89	30.3
	30.4	98.15	1.85	29.8
300°C, 100 mL/min, $8H_2$:$1CO_2$	79.2	99.60	0.40	78.9
with 13X	92.8	99.77	0.23	92.5
	93.6	99.78	0.22	93.4
	94.2	99.78	0.22	94.0

Table 5.9 reports the conversion, selectivity and yield of the reaction, using zeolite or quartz to dilute the catalyst. An increase of the conversion is observed comparing the reference methanation carried out at 350°C and flow rate of 200mL/min with the three reaction cycles performed under the same conditions but in the presence of 13X zeolite, noting the occurrence of sorption-enhancement. In addition, a slight increase in selectivity is also observed, since the sequestration of water leads to an improvement of the reactions that produce more water, so the hydrogenation to methane, instead of

just the reduction to monoxide. The effect is very limited since nickel is already very selective towards the formation of methane.[1,9,12,13,46,93]

No variation of conversion and selectivity is observed between the various methanations with zeolite interspersed by water desorption, therefore the degradation of the zeolite is absent or so slow that it cannot be clearly noticed in such a low number of cycles.[9,13,90,120]

Different conditions were applied to carry out the reaction, to understand which one provides the greatest improvement.

A reduction of conversion and selectivity is observed decreasing the temperature to 300°C, both for the reference and for the cycles with zeolite, due to the slowing down of the reaction kinetics, decreasing the hydrogenation rate of the intermediates.[4,10,13,42,43,80,83] The sorption-enhancement is observed but it is low compared to that previously achieved, due to lower water production. In fact, a shift in the reaction equilibrium can occur only if the product to be captured is generated, otherwise the reaction is unchanged. This clearly shows that the sorption-enhancement is more intense for higher conversions of the reaction, pointing out an exponential improvement rather than linear.[12]

An increase in conversion and selectivity is revealed reducing the flow rate to 100mL/min at 300°C, since the reagents remain longer in contact with the catalyst, allowing more carbon dioxide, hydrogen and intermediates to react.[1,3,7,13,31,42,46,50,61,63,79,80] This is also reflected for the application of zeolite, observing a particularly high sorption-enhancement which increases the conversion by about 20%. This is due to the greater production of water and to a longer contact time of water with 13X, leaving more time for the occupation of the adsorption sites, leading to a higher adsorption and an increase of the water adsorption capacity.[9,46] However, it should be clear that a decrease in the flow rate also involves a reduction in the productivity of the reactor.

A reduction in conversion and selectivity is observed halving the quantity of catalyst, but keeping the same catalytic bed mass and working conditions, resulting in less catalytic sites to carry out the reaction. In these conditions, there is a very slight sorption-enhancement on the conversion, while nothing change for the selectivity.[1,14,111]

To conclude, an increase of the hydrogen content in the feed is tested, adopting a ratio of 8:1, showing that an excess of reagent allows to shift the methanation equilibrium towards the products, according to Le Châtelier's principle, increasing significantly the conversion.[1,3,29,32,42] In excess of reductant, hydrogenation to methane is particularly favored compared to the production of carbon monoxide, caused by the greater consumption of hydrogen for the former reaction, allowing an increase in selectivity. The application of zeolite involves the appearance of a strong sorption-enhancement, increasing selectivity and conversion, the latter of about 14%. Although the conversion is higher, the increase caused by the sorption-enhancement is smaller compared to the use of a mixture with a volumetric ratio of 4:1, therefore there must be a negative effect that restrains the increase. This phenomenon is caused by the dilution of water with the excess hydrogen, resulting in a decrease of its partial pressure, with a consequent reduction of the water adsorption capacity of the zeolite.[9]

No significant variation of conversion and selectivity occurs for the three cycles of methanation interspersed by water desorption, for all the operating conditions. This means that the zeolite is sufficiently stable not to permit performance degradation for such a small number of catalytic cycles.[9,13,90,120]

6. CONCLUSIONS AND FUTURE PERSPECTIVES

The results of this study have shown that the use of γ-alumina, in particular promoted by cerium, or monoclinic zirconia as supports favor the conversion and selectivity. On the contrary, the use of zeolite as support does not provide good performance, due to the collapse of the crystalline structure, losing any affinity with water. Titania-based supports, whether anatase or a mixture of anatase and rutile, do not show good activity, due to the coating of the metal sites with a layer of reduced oxide, caused by the strong metal-support interaction. It has been proven that the use of nickel is more desirable than cobalt, due to the greater selectivity, preferring higher loadings to ensure the abundance of active metallic sites.

The study points out that the fundamental parameters that allow good conversion and selectivity are the following:

- high surface area, providing a greater number of sites for the adsorption and activation of carbon dioxide;
- good reducibility, obtaining a greater number of metallic sites for the dissociation and activation of hydrogen, as well as the transformation of important intermediates, such as carbon monoxide;
- redox properties provided by a reducible oxide, support or promoter, allowing an easier activation of carbon dioxide through reaction with the oxygen vacancies, directing the conversion of the reagent towards the production of methane.

The use of zeolite as additive in the catalytic bed has shown clear advantages and improvements compared to traditional methanation, shifting the reaction equilibrium towards the products, according to Le Châtelier's principle.

Many perspectives are open to the future, making research essential to improve the efficiency of catalysts and to increase the available knowledge regarding the reaction path of methanation.

First of all, a deeper understanding of the role of zeolite in the reactor will be essential, both as an additive, but in particular as a support. Regarding the latter, careful research will be necessary to determine the conditions to maintain the crystalline structure and water adsorption properties. A valid strategy may be the decomposition of the metal precursor with plasma, carrying out calcination at low temperatures, which allows less damage to the crystalline lattice.[37,48]

Regarding the active phase, extensive studies will be useful in order to achieve a higher efficiency than that achievable through the use of nickel alone. A combination of nickel and cobalt could be thoroughly investigated, having previously shown better performance than the individual metals.[66] Another useful metal in combination with nickel could be iron, obtaining good performance and an improvement in stability.[10,30,43] To conclude, small percentages of noble metals, such as ruthenium, platinum, rhodium or rhenium, could be used as promoters to increase the reducibility of the catalyst, increasing the metal area and the number of active sites.[2,10,56,71,72,89,107]

To conclude, it is possible to engineer the supports and their synthesis to achieve greater dispersion of the active phase and better activation of the reagents. The synthesis of ordered mesoporous supports allows the formation of pores with tunable diameter, changing the size of the surfactant responsible for their creation, obtaining a very high dispersion and a greater resistance to carbon coke deposition.[10,11,26,27,33,37,50,61,62,80,103,106] Figure 6.1 shows the synthesis of a catalyst from an ordered mesoporous support, by using surfactant. Another possibility is the use of supports composed of a multitude of oxides, including reducible ones, combining the redox properties of one with the stability of the other, or decreasing the crystalline order to favor the formation of highly reactive crystalline defects and oxygen vacancies.[2,7,10,11,31,40]

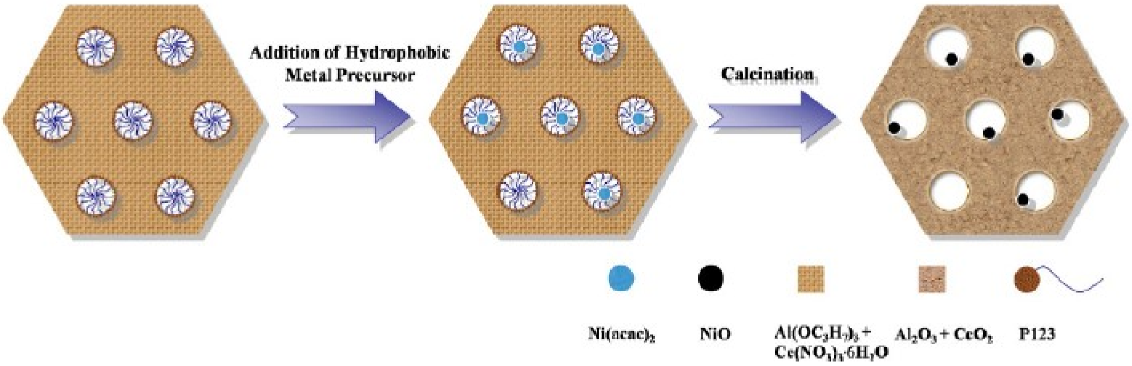

Fig. 6.1 Schematic diagram of the synthesis of a catalyst from an ordered mesoporous support.[62]

7. BIBLIOGRAPHY

(1) Cañada-Barcala, A.; Larriba, M.; Maté, V. I. Á.; Dobladez, J. A. D. CO2 Methanation Enhanced with a Cyclic SERP Process Using a Commercial Ni-Based Catalyst Mixed with 3A Zeolite as Adsorbent. *Chemical Engineering Journal* **2023**, *461*, 141897.

(2) Ocampo, F.; Louis, B.; Kiwi-Minsker, L.; Roger, A.-C. Effect of Ce/Zr Composition and Noble Metal Promotion on Nickel Based CexZr1- xO2 Catalysts for Carbon Dioxide Methanation. *Applied Catalysis A: General* **2011**, *392* (1–2), 36–44.

(3) Hu, D.; Gao, J.; Ping, Y.; Jia, L.; Gunawan, P.; Zhong, Z.; Xu, G.; Gu, F.; Su, F. Enhanced Investigation of CO Methanation over Ni/Al $_2$ O $_3$ Catalysts for Synthetic Natural Gas Production. *Ind. Eng. Chem. Res.* **2012**, *51* (13), 4875–4886. https://doi.org/10.1021/ie300049f.

(4) Charisiou, N. D.; Papageridis, K. N.; Siakavelas, G.; Tzounis, L.; Kousi, K.; Baker, M. A.; Hinder, S. J.; Sebastian, V.; Polychronopoulou, K.; Goula, M. A. Glycerol Steam Reforming for Hydrogen Production over Nickel Supported on Alumina, Zirconia and Silica Catalysts. *Top Catal* **2017**, *60* (15–16), 1226–1250. https://doi.org/10.1007/s11244-017-0796-y.

(5) Nichele, V.; Signoretto, M.; Menegazzo, F.; Gallo, A.; Dal Santo, V.; Cruciani, G.; Cerrato, G. Glycerol Steam Reforming for Hydrogen Production: Design of Ni Supported Catalysts. *Applied Catalysis B: Environmental* **2012**, *111*, 225–232.

(6) Nichele, V.; Signoretto, M.; Menegazzo, F.; Rossetti, I.; Cruciani, G. Hydrogen Production by Ethanol Steam Reforming: Effect of the Synthesis Parameters on the Activity of Ni/TiO2 Catalysts. *International Journal of Hydrogen Energy* **2014**, *39* (9), 4252–4258.

(7) Ocampo, F.; Louis, B.; Roger, A.-C. Methanation of Carbon Dioxide over Nickel-Based Ce0. 72Zr0. 28O2 Mixed Oxide Catalysts Prepared by Sol–Gel Method. *Applied Catalysis A: General* **2009**, *369* (1–2), 90–96.

(8) Solis-Garcia, A.; Louvier-Hernandez, J. F.; Almendarez-Camarillo, A.; Fierro-Gonzalez, J. C. Participation of Surface Bicarbonate, Formate and Methoxy Species in the Carbon Dioxide Methanation Catalyzed by ZrO2-Supported Ni. *Applied Catalysis B: Environmental* **2017**, *218*, 611–620.

(9) Wei, L.; Azad, H.; Haije, W.; Grenman, H.; de Jong, W. Pure Methane from CO2 Hydrogenation Using a Sorption Enhanced Process with Catalyst/Zeolite Bifunctional Materials. *Applied Catalysis B: Environmental* **2021**, *297*, 120399.

(10) Lv, C.; Xu, L.; Chen, M.; Cui, Y.; Wen, X.; Li, Y.; Wu, C.; Yang, B.; Miao, Z.; Hu, X. Recent Progresses in Constructing the Highly Efficient Ni Based Catalysts with Advanced Low-Temperature Activity toward CO2 Methanation. *Frontiers in Chemistry* **2020**, *8*, 269.

(11) Lee, W. J.; Li, C.; Prajitno, H.; Yoo, J.; Patel, J.; Yang, Y.; Lim, S. Recent Trend in Thermal Catalytic Low Temperature CO2 Methanation: A Critical Review. *Catalysis today* **2021**, *368*, 2–19.

(12) Borgschulte, A.; Gallandat, N.; Probst, B.; Suter, R.; Callini, E.; Ferri, D.; Arroyo, Y.; Erni, R.; Geerlings, H.; Züttel, A. Sorption Enhanced CO 2 Methanation. *Physical Chemistry Chemical Physics* **2013**, *15* (24), 9620–9625.

(13) Gomez, L.; Martínez, I.; Navarro, M. V.; Garcia, T.; Murillo, R. Sorption-Enhanced CO and CO2 Methanation (SEM) for the Production of High Purity Methane. *Chemical Engineering Journal* **2022**, *440*, 135842.

(14) Agirre, I.; Acha, E.; Cambra, J. F.; Barrio, V. L. Water Sorption Enhanced CO_2 Methanation Process: Optimization of Reaction Conditions and Study of Various Sorbents. *Chem. Eng. Sci.* **2021**, *237*, 116546. https://doi.org/10.1016/j.ces.2021.116546.

(15) Li, W.; Nie, X.; Jiang, X.; Zhang, A.; Ding, F.; Liu, M.; Liu, Z.; Guo, X.; Song, C. ZrO_2 Support Imparts Superior Activity and Stability of Co Catalysts for CO_2 Methanation. *Appl. Catal. B-Environ.* **2018**, *220*, 397–408. https://doi.org/10.1016/j.apcatb.2017.08.048.

(16) Massa, F.; Coppola, A.; Scala, F. A Thermodynamic Study of Sorption-Enhanced CO2 Methanation at Low Pressure. *Journal of CO2 Utilization* **2020**, *35*, 176–184.

(17) Bezerra, D. P.; Oliveira, R. S.; Vieira, R. S.; Cavalcante, C. L.; Azevedo, D. C. S. Adsorption of CO2 on Nitrogen-Enriched Activated Carbon and Zeolite 13X. *Adsorption* **2011**, *17* (1), 235–246. https://doi.org/10.1007/s10450-011-9320-z.

(18) Chatti, R.; Bansiwal, A. K.; Thote, J. A.; Kumar, V.; Jadhav, P.; Lokhande, S. K.; Biniwale, R. B.; Labhsetwar, N. K.; Rayalu, S. S. Amine Loaded Zeolites for Carbon Dioxide Capture: Amine Loading and Adsorption Studies. *Microporous and Mesoporous Materials* **2009**, *121* (1–3), 84–89.

(19) Chen, C.; Park, D.-W.; Ahn, W.-S. CO2 Capture Using Zeolite 13X Prepared from Bentonite. *Applied Surface Science* **2014**, *292*, 63–67.

(20) Garshasbi, V.; Jahangiri, M.; Anbia, M. Equilibrium CO2 Adsorption on Zeolite 13X Prepared from Natural Clays. *Applied Surface Science* **2017**, *393*, 225–233.

(21) Zabielska, K.; Aleksandrzak, T.; Gabruś, E. Influence of Humidity on Carbon Dioxide Adsorptionon Zeolite 13X. *Chemical and Process Engineering* **2020**, *41* (3), 197–208.

(22) Ren, J.; Guo, H.; Yang, J.; Qin, Z.; Lin, J.; Li, Z. Insights into the Mechanisms of CO_2 Methanation on Ni(111) Surfaces by Density Functional Theory. *Appl. Surf. Sci.* **2015**, *351*, 504–516. https://doi.org/10.1016/j.apsusc.2015.05.173.

(23) Wilkins, N. S.; Sawada, J. A.; Rajendran, A. Measurement of Competitive $$\text {CO}_{2}$$ and $$\text {H}_{2}\text {O}$$ Adsorption on Zeolite 13X for Post-Combustion $$\text {CO}_{2}$$ Capture. *Adsorption* **2020**, *26* (5), 765–779. https://doi.org/10.1007/s10450-020-00199-3.

(24) Messou, D.; Bernardin, V.; Meunier, F.; Ordoño, M. B.; Urakawa, A.; Machado, B. F.; Collière, V.; Philippe, R.; Serp, P.; Le Berre, C. Origin of the Synergistic Effect between TiO2 Crystalline Phases in the Ni/TiO2-Catalyzed CO2 Methanation Reaction. *Journal of Catalysis* **2021**, *398*, 14–28.

(25) Wang, P.; Sun, Q.; Zhang, Y.; Cao, J. Synthesis of Zeolite 4A from Kaolin and Its Adsorption Equilibrium of Carbon Dioxide. *Materials* **2019**, *12* (9), 1536. https://doi.org/10.3390/ma12091536.

(26) Seo, J. G.; Youn, M. H.; Chung, J. S.; Song, I. K. Effect of Calcination Temperature of Mesoporous Nickel–Alumina Catalysts on Their Catalytic Performance in Hydrogen Production by Steam Reforming of Liquefied Natural Gas (LNG). *Journal of Industrial and Engineering Chemistry* **2010**, *16* (5), 795–799.

(27) Kho, E. T.; Scott, J.; Amal, R. Ni/TiO2 for Low Temperature Steam Reforming of Methane. *Chemical Engineering Science* **2016**, *140*, 161–170.

(28) Dahdah, E.; Estephane, J.; Gennequin, C.; Aboukais, A.; Abi-Aad, E.; Aouad, S. Zirconia Supported Nickel Catalysts for Glycerol Steam Reforming: Effect of Zirconia Structure on the Catalytic Performance. *Int. J. Hydrog. Energy* **2020**, *45* (7), 4457–4467. https://doi.org/10.1016/j.ijhydene.2019.12.019.

(29) Abelló, S.; Berrueco, C.; Montané, D. High-Loaded Nickel–Alumina Catalyst for Direct CO2 Hydrogenation into Synthetic Natural Gas (SNG). *Fuel* **2013**, *113*, 598–609.

(30) Garbarino, G.; Riani, P.; Magistri, L.; Busca, G. A Study of the Methanation of Carbon Dioxide on Ni/Al2O3 Catalysts at Atmospheric Pressure. *International journal of hydrogen energy* **2014**, *39* (22), 11557–11565.

(31) Mebrahtu, C.; Abate, S.; Perathoner, S.; Chen, S.; Centi, G. CO2 Methanation over Ni Catalysts Based on Ternary and Quaternary Mixed Oxide: A Comparison and Analysis of the Structure-Activity Relationships. *Catalysis Today* **2018**, *304*, 181–189.

(32) Kristiani, A.; Takeishi, K. CO2 Methanation over Nickel-Based Catalyst Supported on Yttria-Stabilized Zirconia. *Catalysis Communications* **2022**, *165*, 106435.

(33) Sun, C.; Beaunier, P.; Da Costa, P. Effect of Ceria Promotion on the Catalytic Performance of Ni/SBA-16 Catalysts for CO2 Methanation. *Catalysis Science & Technology* **2020**, *10* (18), 6330–6341.

(34) Li, J.; Lin, Y.; Pan, X.; Miao, D.; Ding, D.; Cui, Y.; Dong, J.; Bao, X. Enhanced CO $_2$ Methanation Activity of Ni/Anatase Catalyst by Tuning Strong Metal–Support Interactions. *ACS Catal.* **2019**, *9* (7), 6342–6348. https://doi.org/10.1021/acscatal.9b00401.

(35) Liu, J.; Li, C.; Wang, F.; He, S.; Chen, H.; Zhao, Y.; Wei, M.; Evans, D. G.; Duan, X. Enhanced Low-Temperature Activity of CO 2 Methanation over Highly-Dispersed Ni/TiO 2 Catalyst. *Catalysis Science & Technology* **2013**, *3* (10), 2627–2633.

(36) Ma, L.; Ye, R.; Huang, Y.; Reina, T. R.; Wang, X.; Li, C.; Zhang, X. L.; Fan, M.; Zhang, R.; Liu, J. Enhanced Low-Temperature CO2 Methanation Performance of Ni/ZrO2 Catalysts via a Phase Engineering Strategy. *Chemical Engineering Journal* **2022**, *446*, 137031.

(37) Shen, L.; Xu, J.; Zhu, M.; Han, Y.-F. Essential Role of the Support for Nickel-Based CO $_2$ Methanation Catalysts. *ACS Catal.* **2020**, *10* (24), 14581–14591. https://doi.org/10.1021/acscatal.0c03471.

(38) Coppola, A.; Massa, F.; Salatino, P.; Scala, F. Evaluation of Two Sorbents for the Sorption-Enhanced Methanation in a Dual Fluidized Bed System. *Biomass Conv. Bioref.* **2021**, *11* (1), 111–119. https://doi.org/10.1007/s13399-020-00829-4.

(39) Delmelle, R.; Terreni, J.; Remhof, A.; Heel, A.; Proost, J.; Borgschulte, A. Evolution of Water Diffusion in a Sorption-Enhanced Methanation Catalyst. *Catalysts* **2018**, *8* (9), 341.

(40) Pan, Q.; Peng, J.; Sun, T.; Wang, S.; Wang, S. Insight into the Reaction Route of CO2 Methanation: Promotion Effect of Medium Basic Sites. *Catalysis Communications* **2014**, *45*, 74–78.

(41) Wang, X.; Shi, H.; Kwak, J. H.; Szanyi, J. Mechanism of CO_2 Hydrogenation on Pd/Al_2O_3 Catalysts: Kinetics and Transient DRIFTS-MS Studies. *ACS Catal.* **2015**, *5* (11), 6337–6349. https://doi.org/10.1021/acscatal.5b01464.

(42) Gómez, L.; Grasa, G.; Martínez, I.; Murillo, R. Performance Study of a Methanation Process for a Syngas Obtained from a Sorption Enhanced Gasification Process. *Chemical Engineering Science* **2023**, *267*, 118291.

(43) Mutz, B.; Belimov, M.; Wang, W.; Sprenger, P.; Serrer, M.-A.; Wang, D.; Pfeifer, P.; Kleist, W.; Grunwaldt, J.-D. Potential of an Alumina-Supported Ni_3Fe Catalyst in the Methanation of CO_2: Impact of Alloy Formation on Activity and Stability. *ACS Catal.* **2017**, *7* (10), 6802–6814. https://doi.org/10.1021/acscatal.7b01896.

(44) Götz, M.; Lefebvre, J.; Mörs, F.; Koch, A. M.; Graf, F.; Bajohr, S.; Reimert, R.; Kolb, T. Renewable Power-to-Gas: A Technological and Economic Review. *Renewable energy* **2016**, *85*, 1371–1390.

(45) Coppola, A.; Massa, F.; Scala, F. Simulation of a Sorption-Enhanced Methanation Process with CaO in a Dual Interconnected Fluidized Bed System. *Fuel* **2023**, *339*, 127374.

(46) Kiefer, F.; Nikolic, M.; Borgschulte, A.; Eggenschwiler, P. D. Sorption-Enhanced Methane Synthesis in Fixed-Bed Reactors. *Chemical Engineering Journal* **2022**, *449*, 137872.

(47) Garbarino, G.; Campodonico, S.; Perez, A. R.; Carnasciali, M. M.; Riani, P.; Finocchio, E.; Busca, G. Spectroscopic Characterization of Ni/Al2O3 Catalytic Materials for the Steam Reforming of Renewables. *Applied Catalysis A: General* **2013**, *452*, 163–173.

(48) Jia, X.; Zhang, X.; Rui, N.; Hu, X.; Liu, C. Structural Effect of Ni/ZrO2 Catalyst on CO2 Methanation with Enhanced Activity. *Applied Catalysis B: Environmental* **2019**, *244*, 159–169.

(49) Aksoylu, A. E.; Akin, A. N.; Sunol, S. G.; Onsan, Z. I. The Effect of Metal Loading on the Adsorption Parameters of Carbon Dioxide on Coprecipitated Nickel-Alumina Catalysts. *Turk. J. Chem.* **1996**, *20* (1), 88–94.

(50) Aljishi, A.; Veilleux, G.; Lalinde, J. A. H.; Kopyscinski, J. The Effect of Synthesis Parameters on Ordered Mesoporous Nickel Alumina Catalyst for CO_2 Methanation. *Appl. Catal. A-Gen.* **2018**, *549*, 263–272. https://doi.org/10.1016/j.apcata.2017.10.012.

(51) Janlamool, J.; Praserthdam, P.; Jongsomjit, B. Ti-Si Composite Oxide-Supported Cobalt Catalysts for CO_2 Hydrogenation. *J. Nat. Gas Chem.* **2011**, *20* (5), 558–564. https://doi.org/10.1016/S1003-9953(10)60213-7.

(52) Aldana, P. U.; Ocampo, F.; Kobl, K.; Louis, B.; Thibault-Starzyk, F.; Daturi, M.; Bazin, P.; Thomas, S.; Roger, A. C. Catalytic CO2 Valorization into CH4 on Ni-Based Ceria-Zirconia. Reaction Mechanism by Operando IR Spectroscopy. *Catalysis Today* **2013**, *215*, 201–207.

(53) Lin, Y.; Zhu, Y.; Pan, X.; Bao, X. Modulating the Methanation Activity of Ni by the Crystal Phase of TiO 2. *Catalysis Science & Technology* **2017**, *7* (13), 2813–2818.

(54) Takenaka, S.; Shimizu, T.; Otsuka, K. Complete Removal of Carbon Monoxide in Hydrogen-Rich Gas Stream through Methanation over Supported Metal Catalysts. *International Journal of Hydrogen Energy* **2004**, *29* (10), 1065–1073.

(55) Takenaka, S.; Kobayashi, S.; Ogihara, H.; Otsuka, K. Ni/SiO2 Catalyst Effective for Methane Decomposition into Hydrogen and Carbon Nanofiber. *Journal of Catalysis* **2003**, *217* (1), 79–87.

(56) Tada, S.; Kikuchi, R.; Takagaki, A.; Sugawara, T.; Oyama, S. T.; Urasaki, K.; Satokawa, S. Study of RuNi/TiO2 Catalysts for Selective CO Methanation. *Applied catalysis B: environmental* **2013**, *140*, 258–264.

(57) da Silva, D. C. D.; Letichevsky, S.; Borges, L. E. P.; Appel, L. G. The Ni/ZrO_2 Catalyst and the Methanation of CO and CO_2. *Int. J. Hydrog. Energy* **2012**, *37* (11), 8923–8928. https://doi.org/10.1016/j.ijhydene.2012.03.020.

(58) Gao, J.; Wang, Y.; Ping, Y.; Hu, D.; Xu, G.; Gu, F.; Su, F. A Thermodynamic Analysis of Methanation Reactions of Carbon Oxides for the Production of Synthetic Natural Gas. *RSC advances* **2012**, *2* (6), 2358–2368.

(59) Rönsch, S.; Schneider, J.; Matthischke, S.; Schlüter, M.; Götz, M.; Lefebvre, J.; Prabhakaran, P.; Bajohr, S. Review on Methanation–From Fundamentals to Current Projects. *Fuel* **2016**, *166*, 276–296.

(60) Bereketidou, O. A.; Goula, M. A. Biogas Reforming for Syngas Production over Nickel Supported on Ceria–Alumina Catalysts. *Catalysis Today* **2012**, *195* (1), 93–100.

(61) Rezaei, M.; Alavi, S. M.; Sahebdelfar, S.; Xinmei, L.; Qian, L.; Yan, Z.-F. CO_2-CH_4 Reforming over Nickel Catalysts Supported on Mesoporous Nanocrystalline Zirconia with High Surface Area. *Energy Fuels* **2007**, *21* (2), 581–589. https://doi.org/10.1021/ef0606005.

(62) Wang, N.; Shen, K.; Huang, L.; Yu, X.; Qian, W.; Chu, W. Facile Route for Synthesizing Ordered Mesoporous Ni–Ce–Al Oxide Materials and Their Catalytic Performance for Methane Dry Reforming to Hydrogen and Syngas. *ACS Catal.* **2013**, *3* (7), 1638–1651. https://doi.org/10.1021/cs4003113.

(63) Takanabe, K.; Nagaoka, K.; Nariai, K.; Aika, K. Influence of Reduction Temperature on the Catalytic Behavior of Co/TiO2 Catalysts for CH4/CO2 Reforming and Its Relation with Titania Bulk Crystal Structure. *Journal of Catalysis* **2005**, *230* (1), 75–85.

(64) Yao, N.; Chen, J.; Zhang, J.; Zhang, J. Influence of Support Calcination Temperature on Properties of Ni/TiO2 for Catalytic Hydrogenation of o-Chloronitrobenzene to o-Chloroaniline. *Catalysis Communications* **2008**, *9* (6), 1510–1516.

(65) AlSabban, B.; Falivene, L.; Kozlov, S. M.; Aguilar-Tapia, A.; Ould-Chikh, S.; Hazemann, J.-L.; Cavallo, L.; Basset, J.-M.; Takanabe, K. In-Operando Elucidation of Bimetallic CoNi Nanoparticles during High-Temperature CH4/CO2 Reaction. *Applied Catalysis B: Environmental* **2017**, *213*, 177–189.

(66) Zhang, M.; Zhang, J.; Wu, Y.; Pan, J.; Zhang, Q.; Tan, Y.; Han, Y. Insight into the Effects of the Oxygen Species over Ni/ZrO2 Catalyst Surface on Methane Reforming with Carbon Dioxide. *Applied Catalysis B: Environmental* **2019**, *244*, 427–437.

(67) Hwang, S.; Lee, J.; Hong, U. G.; Seo, J. G.; Jung, J. C.; Koh, D. J.; Lim, H.; Byun, C.; Song, I. K. Methane Production from Carbon Monoxide and Hydrogen over Nickel–Alumina Xerogel Catalyst: Effect of Nickel Content. *Journal of Industrial and Engineering Chemistry* **2011**, *17* (1), 154–157.

(68) Wang, S.; Lu, G. M. Role of CeO2 in Ni/CeO2–Al2O3 Catalysts for Carbon Dioxide Reforming of Methane. *Applied Catalysis B: Environmental* **1998**, *19* (3–4), 267–277.

(69) He, L.; Ren, Y.; Yue, B.; Tsang, S. C. E.; He, H. Tuning Metal-Support Interactions on Ni/Al_2O_3 Catalysts to Improve Catalytic Activity and Stability for Dry Reforming of Methane. *Processes* **2021**, *9* (4), 706. https://doi.org/10.3390/pr9040706.

(70) Liu, Y.; Chen, J.; Fang, K.; Wang, Y.; Sun, Y. A Large Pore-Size Mesoporous Zirconia Supported Cobalt Catalyst with Good Performance in Fischer–Tropsch Synthesis. *Catalysis Communications* **2007**, *8* (6), 945–949.

(71) Storsæter, S.; Tøtdal, B.; Walmsley, J. C.; Tanem, B. S.; Holmen, A. Characterization of Alumina-, Silica-, and Titania-Supported Cobalt Fischer–Tropsch Catalysts. *Journal of catalysis* **2005**, *236* (1), 139–152.

(72) Chu, W.; Chernavskii, P. A.; Gengembre, L.; Pankina, G. A.; Fongarland, P.; Khodakov, A. Y. Cobalt Species in Promoted Cobalt Alumina-Supported Fischer–Tropsch Catalysts. *Journal of Catalysis* **2007**, *252* (2), 215–230.

(73) Jean-Marie, A.; Griboval-Constant, A.; Khodakov, A. Y.; Diehl, F. Cobalt Supported on Alumina and Silica-Doped Alumina: Catalyst Structure and Catalytic Performance in Fischer–Tropsch Synthesis. *Comptes Rendus Chimie* **2009**, *12* (6–7), 660–667.

(74) Jongsomjit, B.; Sakdamnuson, C.; Praserthdam, P. Dependence of Crystalline Phases in Titania on Catalytic Properties during CO Hydrogenation of Co/TiO2 Catalysts. *Materials chemistry and physics* **2005**, *89* (2–3), 395–401.

(75) Enache, D. I.; Roy-Auberger, M.; Revel, R. Differences in the Characteristics and Catalytic Properties of Cobalt-Based Fischer–Tropsch Catalysts Supported on Zirconia and Alumina. *Applied Catalysis A: General* **2004**, *268* (1–2), 51–60.

(76) Rahmati, M.; Huang, B.; Mortensen Jr, M. K.; Keyvanloo, K.; Fletcher, T. H.; Woodfield, B. F.; Hecker, W. C.; Argyle, M. D. Effect of Different Alumina Supports on Performance of Cobalt Fischer-Tropsch Catalysts. *Journal of Catalysis* **2018**, *359*, 92–100.

(77) Eschemann, T. O.; Bitter, J. H.; De Jong, K. P. Effects of Loading and Synthesis Method of Titania-Supported Cobalt Catalysts for Fischer–Tropsch Synthesis. *Catalysis today* **2014**, *228*, 89–95.

(78) Liu, C.; Li, J.; Zhang, Y.; Chen, S.; Zhu, J.; Liew, K. Fischer–Tropsch Synthesis over Cobalt Catalysts Supported on Nanostructured Alumina with Various Morphologies. *Journal of Molecular Catalysis A: Chemical* **2012**, *363*, 335–342.

(79) Borg, Ø.; Eri, S.; Blekkan, E. A.; Storsæter, S.; Wigum, H.; Rytter, E.; Holmen, A. Fischer–Tropsch Synthesis over γ-Alumina-Supported Cobalt Catalysts: Effect of Support Variables. *Journal of Catalysis* **2007**, *248* (1), 89–100.

(80) Vosoughi, V.; Badoga, S.; Dalai, A. K.; Abatzoglou, N. Modification of Mesoporous Alumina as a Support for Cobalt-Based Catalyst in Fischer-Tropsch Synthesis. *Fuel Processing Technology* **2017**, *162*, 55–65.

(81) Rane, S.; Borg, Ø.; Rytter, E.; Holmen, A. Relation between Hydrocarbon Selectivity and Cobalt Particle Size for Alumina Supported Cobalt Fischer–Tropsch Catalysts. *Applied Catalysis A: General* **2012**, *437*, 10–17.

(82) Jongsomjit, B.; Wongsalee, T.; Praserthdam, P. Study of Cobalt Dispersion on Titania Consisting Various Rutile: Anatase Ratios. *Materials chemistry and physics* **2005**, *92* (2–3), 572–577.

(83) Agnelli, M.; Swaan, H. M.; Marquez-Alvarez, C.; Martin, G. A.; Mirodatos, C. CO Hydrogenation on a Nickel Catalyst: II. A Mechanistic Study by Transient Kinetics and Infrared Spectroscopy. *Journal of Catalysis* **1998**, *175* (1), 117–128.

(84) Shah, M.; Al Mesfer, M. K.; Danish, M. Effect of Titania Synthesis Conditions on the Catalytic Performance of Mesoporous Ni/TiO2 Catalysts for Carbon Dioxide Reforming of Methane. *International Journal of Hydrogen Energy* **2022**, *47* (14), 8867–8874.

(85) Delmelle, R.; Duarte, R. B.; Franken, T.; Burnat, D.; Holzer, L.; Borgschulte, A.; Heel, A. Development of Improved Nickel Catalysts for Sorption Enhanced CO2 Methanation. *international journal of hydrogen energy* **2016**, *41* (44), 20185–20191.

(86) Terreni, J.; Trottmann, M.; Delmelle, R.; Heel, A.; Trtik, P.; Lehmann, E. H.; Borgschulte, A. Observing Chemical Reactions by Time-Resolved High-Resolution Neutron Imaging. *J. Phys. Chem. C* **2018**, *122* (41), 23574–23581. https://doi.org/10.1021/acs.jpcc.8b07321.

(87) Choya, A.; de Rivas, B.; González-Velasco, J. R.; Gutiérrez-Ortiz, J. I.; López-Fonseca, R. Oxidation of Lean Methane over Cobalt Catalysts Supported on Ceria/Alumina. *Applied Catalysis A: General* **2020**, *591*, 117381.

(88) Boon, J. Sorption-Enhanced Reactions as Enablers for CO2 Capture and Utilisation. *Current Opinion in Chemical Engineering* **2023**, *40*, 100919.

(89) Hilmen, A. M.; Schanke, D.; Hanssen, K. F.; Holmen, A. Study of the Effect of Water on Alumina Supported Cobalt Fischer–Tropsch Catalysts. *Applied Catalysis A: General* **1999**, *186* (1–2), 169–188.

(90) Fischer, F.; Lutz, W.; Buhl, J.-C.; Laevemann, E. Insights into the Hydrothermal Stability of Zeolite 13X. *Microporous and Mesoporous Materials* **2018**, *262*, 258–268.

(91) Du, C.; Yang, H. Synthesis and Characterization of Zeolite 4A-Type Desiccant from Kaolin. *American Mineralogist* **2010**, *95* (5–6), 741–746.

(92) Zhu, W.; Gora, L.; van den Berg, A. W. C.; Kapteijn, F.; Jansen, J. C.; Moulijn, J. A. Water Vapour Separation from Permanent Gases by a Zeolite-4A Membrane. *J. Membr. Sci.* **2005**, *253* (1–2), 57–66. https://doi.org/10.1016/j.memsci.2004.12.039.

(93) Walspurger, S.; Elzinga, G. D.; Dijkstra, J. W.; Sarić, M.; Haije, W. G. Sorption Enhanced Methanation for Substitute Natural Gas Production: Experimental Results and Thermodynamic Considerations. *Chemical Engineering Journal* **2014**, *242*, 379–386.

(94) Przydacz, M.; Jędrzejczyk, M.; Brzezińska, M.; Rogowski, J.; Keller, N.; Ruppert, A. M. Solvothermal Hydrodeoxygenation of Hydroxymethylfurfural Derived from Biomass towards Added Value Chemicals on Ni/TiO2 Catalysts. *The Journal of Supercritical Fluids* **2020**, *163*, 104827.

(95) Weatherbee, G. D.; Bartholomew, C. H. Hydrogenation of CO2 on Group VIII Metals: II. Kinetics and Mechanism of CO2 Hydrogenation on Nickel. *Journal of Catalysis* **1982**, *77* (2), 460–472.

(96) Raj, K. J. A.; Prakash, M. G.; Mahalakshmy, R.; Elangovan, T.; Viswanathan, B. Liquid Phase Hydrogenation of Crotanaldehyde over Nickel Supported on Titania. *Journal of Molecular Catalysis A: Chemical* **2013**, *366*, 92–98.

(97) Petersen, A. P.; Forbes, R. P.; Govender, S.; Kooyman, P. J.; Van Steen, E. Effect of Alumina Modification on the Reducibility of Co3O4 Crystallites Studied on Inverse-Model Catalysts. *Catal Lett* **2018**, *148* (4), 1215–1227. https://doi.org/10.1007/s10562-018-2332-5.

(98) Peters, A.; Nouroozi, F.; Richter, D.; Lutecki, M.; Gläser, R. Nickel-Loaded Zirconia Catalysts with Large Specific Surface Area for High-Temperature Catalytic Applications. *ChemCatChem* **2011**, *3* (3), 598–606. https://doi.org/10.1002/cctc.201000277.

(99) Yue, M. B.; Xue, T.; Jiao, W. Q.; Wang, Y. M. Performance of Mesoporous Silica-Doped Aluminas on Nickel Passivation. *Materials Letters* **2013**, *91*, 115–117.

(100) Lima, T. M.; Pereira, C. A.; Castelblanco, W. N.; Santos, C. M. B.; da Silva, S. W.; Santana, R. C.; Urquieta-Gonzalez, E. A.; Sartoratto, P. P. C. Zirconia-Supported Cobalt Catalysts: Activity and Selectivity in NO Reduction by CO. *ChemistrySelect* **2017**, *2* (35), 11565–11573. https://doi.org/10.1002/slct.201702475.

(101) Chary, K. V.; Rao, P. V. R.; Rao, V. V. Catalytic Functionalities of Nickel Supported on Different Polymorphs of Alumina. *Catalysis Communications* **2008**, *9* (5), 886–893.

(102) Borg, Ø.; Dietzel, P. D.; Spjelkavik, A. I.; Tveten, E. Z.; Walmsley, J. C.; Diplas, S.; Eri, S.; Holmen, A.; Rytter, E. Fischer–Tropsch Synthesis: Cobalt Particle Size and Support Effects on Intrinsic Activity and Product Distribution. *Journal of Catalysis* **2008**, *259* (2), 161–164.

(103) Tsoncheva, T.; Ivanova, L.; Paneva, D.; Mitov, I.; Minchev, C.; Fröba, M. Cobalt and Iron Oxide Modified Mesoporous Zirconia: Preparation, Characterization and Catalytic Behaviour in Methanol Conversion. *Microporous and mesoporous materials* **2009**, *120* (3), 389–396.

(104) Panpranot, J.; Taochaiyaphum, N.; Praserthdam, P. Glycothermal Synthesis of Nanocrystalline Zirconia and Their Applications as Cobalt Catalyst Supports. *Materials Chemistry and Physics* **2005**, *94* (2–3), 207–212.

(105) Gonçalves, G.; Lenzi, M. K.; Santos, O. A. A.; Jorge, L. M. M. Preparation and Characterization of Nickel Based Catalysts on Silica, Alumina and Titania Obtained by Sol–Gel Method. *Journal of Non-Crystalline Solids* **2006**, *352* (32–35), 3697–3704.

(106) Li, G.; Hu, L.; Hill, J. M. Comparison of Reducibility and Stability of Alumina-Supported Ni Catalysts Prepared by Impregnation and Co-Precipitation. *Applied Catalysis A: General* **2006**, *301* (1), 16–24.

(107) Jacobs, G.; Das, T. K.; Zhang, Y.; Li, J.; Racoillet, G.; Davis, B. H. Fischer–Tropsch Synthesis: Support, Loading, and Promoter Effects on the Reducibility of Cobalt Catalysts. *Applied Catalysis A: General* **2002**, *233* (1–2), 263–281.

(108) Bolt, P. H.; Habraken, F. H.; Geus, J. W. Formation of Nickel, Cobalt, Copper, and Iron Aluminates Fromα-Andγ-Alumina-Supported Oxides: A Comparative Study. *Journal of Solid State Chemistry* **1998**, *135* (1), 59–69.

(109) Kumar, V. V.; Naresh, G.; Sudhakar, M.; Tardio, J.; Bhargava, S. K.; Venugopal, A. Role of Brønsted and Lewis Acid Sites on Ni/TiO2 Catalyst for Vapour Phase Hydrogenation of Levulinic Acid: Kinetic and Mechanistic Study. *Applied Catalysis A: General* **2015**, *505*, 217–223.

(110) Xu, B.; Dong, L.; Fan, Y.; Chen, Y. A Study on the Dispersion of NiO and/or WO3 on Anatase. *Journal of Catalysis* **2000**, *193* (1), 88–95.

(111) Joseph Antony Raj, K.; Prakash, M. G.; Elangovan, T.; Viswanathan, B. Selective Hydrogenation of Cinnamaldehyde over Cobalt Supported on Alumina, Silica and Titania. *Catal Lett* **2012**, *142* (1), 87–94. https://doi.org/10.1007/s10562-011-0693-0.

(112) Voß, M.; Borgmann, D.; Wedler, G. Characterization of Alumina, Silica, and Titania Supported Cobalt Catalysts. *Journal of Catalysis* **2002**, *212* (1), 10–21.

(113) Li, Y.; Xu, B.; Fan, Y.; Feng, N.; Qiu, A.; He, J. M. J.; Yang, H.; Chen, Y. The Effect of Titania Polymorph on the Strong Metal-Support Interaction of Pd/TiO2 Catalysts and Their Application in the Liquid Phase Selective Hydrogenation of Long Chain Alkadienes. *Journal of Molecular Catalysis A: Chemical* **2004**, *216* (1), 107–114.

(114) Gavrilovic, L.; Save, J.; Blekkan, E. A. The Effect of Potassium on Cobalt-Based Fischer-Tropsch Catalysts with Different Cobalt Particle Sizes. *Catalysts* **2019**, *9* (4), 351. https://doi.org/10.3390/catal9040351.

(115) Dandekar, A.; Vannice, M. A. Crotonaldehyde Hydrogenation on Pt/TiO2and Ni/TiO2SMSI Catalysts. *Journal of Catalysis* **1999**, *183* (2), 344–354.

(116) Melaet, G.; Ralston, W. T.; Li, C.-S.; Alayoglu, S.; An, K.; Musselwhite, N.; Kalkan, B.; Somorjai, G. A. Evidence of Highly Active Cobalt Oxide Catalyst for the Fischer–Tropsch Synthesis and CO_2 Hydrogenation. *J. Am. Chem. Soc.* **2014**, *136* (6), 2260–2263. https://doi.org/10.1021/ja412447q.

(117) Ye, Q.; Li, D.; Zhao, J.; Zhao, J.; Kang, T.; Cheng, S. Low-Temperature CO Oxidation over Au-Doped 13X-Type Zeolite Catalysts: Preparation and Catalytic Activity. *Front. Environ. Sci. Eng. China* **2011**, *5* (4), 497–504. https://doi.org/10.1007/s11783-011-0256-z.

(118) Wang, P.; Sun, Q.; Zhang, Y.; Cao, J. Effective Removal of Methane Using Nano-Sized Zeolite 4A Synthesized from Kaolin. *Inorganic Chemistry Communications* **2020**, *111*, 107639.

(119) Ma, Y.; Yan, C.; Alshameri, A.; Qiu, X.; Zhou, C. Synthesis and Characterization of 13X Zeolite from Low-Grade Natural Kaolin. *Advanced Powder Technology* **2014**, *25* (2), 495–499.

(120) Buhl, J.-C.; Gerstmann, M.; Lutz, W.; Ritzmann, A. Hydrothermal Stability of the Novel Zeolite Type LSX in Comparison to the Traditional 13X Modification. *Zeitschrift für anorganische und allgemeine Chemie* **2004**, *630* (4), 604–608.

(121) Zhou, R.; Rui, N.; Fan, Z.; Liu, C. Effect of the Structure of Ni/TiO2 Catalyst on CO2 Methanation. *International Journal of Hydrogen Energy* **2016**, *41* (47), 22017–22025.

(122) Jongsomjit, B.; Wongsalee, T.; Praserthdam, P. Characteristics and Catalytic Properties of Co/TiO2 for Various Rutile: Anatase Ratios. *Catalysis Communications* **2005**, *6* (11), 705–710.

(123) Van Meerten, R. Z. C.; Beaumont, A.; Van Nisselrooij, P.; Coenen, J. W. E. Structure Sensitivity and Crystallite Size Change of Nickel during Methanation of CO/H2 on Nickel-Silica Catalysts. *Surface science* **1983**, *135* (1–3), 565–579.